Department of Physics and Astronomy

University of Heidelberg

Master thesis

in Physics

submitted by

Arthur Bolz

born in Filderstadt

2015

Charge Asymmetries in $\pi^+\pi^-$ Photoproduction in a Model for Soft High Energy Scattering and Detector Asymmetry Measurements at the H1 Experiment

This Master thesis has been carried out by Arthur Bolz

at the

Physikalisches Institut

under the supervision of

Herrn Prof. Dr. André Schöning

Abstract

Charge asymmetries in $\pi^+\pi^-$ photoproduction are studied in a model for soft high energy scattering processes. $\pi^+\pi^-$ photoproduction at high center of mass energies is dominated by the exchange of the pomeron with even charge conjugation quantum number C. It is investigated that already small contributions from exchange particles with odd C-parity result in asymmetries in the angular distributions of the pions. C-odd contributions come from photon, and possibly also from odderon exchange. The odderon is the leading exchange particle in soft high energy scattering with odd C-parity but has not been observed yet. Thus measuring charge asymmetries in $\pi^+\pi^-$ photoproduction can help establish its existence experimentally.
As a part of efforts to measure charge asymmetries in $\pi^+\pi^-$ photoproduction at the H1-experiment at the HERA collider, an evaluation of detector effects that may cause charge asymmetries is performed. A focus is put on studying the performance the Fast Track Trigger, which is used to trigger photoproduction events at H1. Several detector effects, most importantly geometric detector asymmetries that are not considered on the trigger level, are shown to give rise to charge asymmetries in the trigger efficiency. It is verified that all effects are correctly described in the detector simulation and can thus be accounted for in an asymmetry measurement.

Zusammenfassung

Ladungsasymmetrien in $\pi^+\pi^-$ Photoproduktion werden in einem Modell für weiche Hochenergie-Streuprozesse studiert. $\pi^+\pi^-$ Photoproduktion bei hohen Schwerpunktsenergien wird vom Austausch des Pomerons mit gerader Ladungskonjugationsquantenzahl C dominiert. Es wird untersucht, dass bereits kleine Beiträge von Austauschteilchen mit ungerader C-Parität zu Asymmetrien in den Winkelverteilungen der Pionen führen. Beiträge mit ungeradem C kommen vom Austausch des Photons und möglicherweise des Odderons. Das Odderon ist das führende Austauschteilchen in weicher Hochenergie-Streuung mit ungerader C-Parität, wurde aber bisher noch nicht beobachtet. Das Messen von Ladungsasymmetrien in $\pi^+\pi^-$ Photoproduktion kann damit helfen, seine Existenz experimentell zu etablieren.
Als Teil der Bemühungen Ladungsasymmetrien in $\pi^+\pi^-$ Photoproduktion am H1-Experiment am HERA-Collider zu messen, werden Detektor Effekte, die Ladungsasymmetrien verursachen könnten, untersucht. Der Schwerpunkt liegt auf der Untersuchung der Leistungsfähigkeit des Fast Track Trigger, mit dem Photoproduktionsereignisse bei H1 getriggert werden. Es wird gezeigt, dass verschiedene Detektoreffekte, vor allem geometrische Detektorasymmetrien die nicht im Trigger berücksichtigt werden, Ladungsasymmetrien in der Triggereffizienz verursachen. Es wird überprüft, dass alle Effekte korrekt in der Detektorsimulation beschrieben sind, und damit bei einer Asymmetriemessung berücksichtigt werden können.

Contents

1 Introduction

Within the *Standard Model of Particle Physics* [1–3], which describes fundamental particles and their interactions, *Quantum Chromodynamics* (QCD) [4] has asserted itself to be the correct theory of the strong force acting between quarks. The non-abelian structure of QCD gives rise to the self-coupling of the strong force carriers, the gluons, with far-reaching consequences; most notably the energy scale dependence of the strong coupling strength α_s. At high energy scales, i.e., small interaction distances, α_s becomes small leading to asymptotically free quarks and gluons [5, 6]. At small scales, on the other hand, α_s increases with increasing interaction distance resulting in the confinement of quarks and gluons into colorless bound states, the hadrons.

The scale dependence of α_s has severe consequences for theoretical QCD predictions and results in the classification of strong interactions into three categories. First, there are *hard* processes that happen at one definite, large energy scale and are computable with perturbative methods, where the interaction is expanded in orders of the (small) coupling constant. Secondly, there are pure small scale phenomena where this approach fails but which can partially be treated by lattice QCD methods [7]. Finally, there are *soft* processes for which no energy scale can be defined at all and which to this point can only be described by phenomenological models.

Hadron-hadron scattering at high energies with a simultaneously small momentum transfer is dominated by soft processes and thus falls into the last category. The most successful model describing the underlying interactions is *Regge Theory* [8, 9], which was first introduced in the late 1950s even before the dawn of QCD, but is still of interest today. In Regge theory, the interaction of colliding particles is described in terms of exchange objects corresponding to so-called *Regge trajectories*. At large scattering energies, the dominant exchange object is the *pomeron*. The key characteristics of the pomeron are, first, that it has a Regge intercept close to 1 and is thus responsible for the observed rise of soft scattering cross sections with increasing center of mass energy (compare for example Figure 2.1.2) and, secondly, that it carries the quantum numbers of the vacuum, i.e., in particular it is a charge conjugation (C) and parity (P) eigenstate with eigenvalues $C = P = +1$.

Understanding the high energy behavior of soft scattering processes is necessary to acquire a full understanding of the strong force. In this context one of the unsolved questions is whether the pomeron is the only exchange particle with an

intercept close to 1. Indeed, from a theoretical point of view the existence of a second pomeron-like object but with odd C-parity is favorable [10]. Having an odd charge parity, this object was coined with the name *odderon* [11].

An odderon contribution to soft scattering processes can lead, among other things, to asymmetries in the final state. In this thesis, charge asymmetries among the pions in $\pi^+\pi^-$ photoproduction, as proposed by Ginzburg et al. [12] and Ivanov et al. [13], are studied in a recently presented model for soft high energy scattering processes by Ewerz et al. [14]. In Chapter 2 an introduction to theoretical concepts relevant for this thesis is given. Results of the asymmetry studies in the scattering model are presented in Chapter 3.

Photoproduction of pion pairs can be studied experimentally at the HERA electron-proton collider at DESY, Hamburg. At the H1 experiment at HERA efforts are being made to measure charge asymmetries among the pions to find evidence for the presence of the odderon. The second part of this master's thesis contributes to these efforts. One cornerstone of measuring charge asymmetries is to understand detector effects that result in charge dependencies in the detection of particles and might introduce artificial asymmetries into a data sample. At H1, the Fast Track Trigger (FTT) used to trigger photoproduction events is particularly prone to such effects.

In Chapter 4 HERA and the H1 experiment are introduced. In Chapter 5 Monte Carlo techniques and simulated event samples used in this thesis are described. In Chapter 6 a reference data sample of $\pi^+\pi^-$ events in deep inelastic scattering (DIS) processes measured at H1 is presented. This sample is used in Chapter 7 to study the performance of the FTT with a focus put on measuring charge asymmetries in the trigger efficiencies. In Chapter 8 the FTT performance is studied in simulated photoproduction events using the insights obtained in Chapter 7. The results of this thesis are summarized in Chapter 9.

Chapter 3, Chapter 6, Chapter 7, and Chapter 8 and are at the core of this thesis and a direct result of my work.

Part I

CHARGE ASYMMETRIES IN $\pi^+\pi^-$ PHOTOPRODUCTION IN A MODEL FOR SOFT HIGH ENERGY SCATTERING

2 Theoretical Background of $\pi^+\pi^-$ Photoproduction

To put this thesis into a theoretical context, a short introduction to the theory of diffractive scattering processes is given. In particular, some basic concepts of Regge theory are explained, the hadronic properties of the photon are introduced, and diffractive photoproduction of pion pairs is studied in a recently presented model for soft high energy scattering processes [14]. A focus is put on how charge asymmetries between the pions arise in this model and how they express themselves in asymmetries of the angular distributions. In addition, the event generator that was used in this thesis to evaluate the model is briefly described and a connection between diffractive scattering processes and electron-proton scattering at the HERA collider is established.

2.1 Diffractive Scattering and Regge Theory

A detailed introduction to soft high energy hadronic scattering and Regge Theory is given for example by Donnachie et al. [15] or Collins [16]. Here, only a brief overview over the phenomenology and terminology relevant for this thesis is given.

2.1.1 $2 \to 2$ Reactions

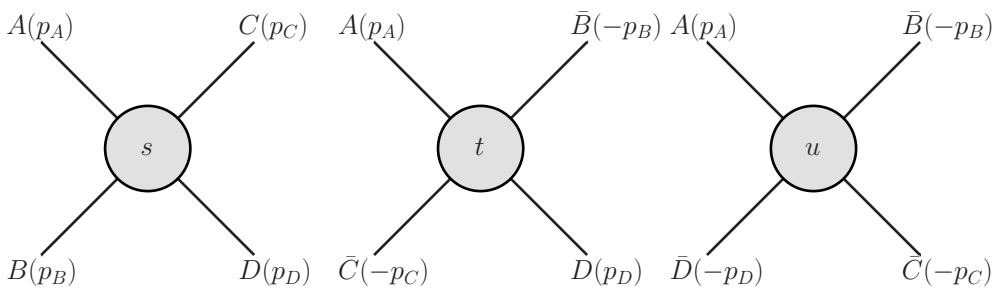

Figure 2.1.1: s-, t-, and u-channel $2 \to 2$ reactions.

In the following, hadron-hadron reactions of the form

$$A(p_A) + B(p_B) \quad \rightarrow \quad C(p_C) + D(p_D) \tag{2.1.1}$$

are considered, where p_X denotes the four momentum of the respective particle X. From the four momenta three Lorentz invariant quantities, the *Mandelstamm* variables

$$s = (p_A + p_B)^2 = (p_C + p_D)^2, \tag{2.1.2}$$
$$t = (p_A - p_C)^2 = (p_B - p_D)^2, \text{ and} \tag{2.1.3}$$
$$u = (p_A - p_D)^2 = (p_B - p_C)^2, \tag{2.1.4}$$

can be formed. Of those only two are independent, as all three are constrained by the relation

$$s + t + u = \sum_{X=A}^{D} m_X^2, \tag{2.1.5}$$

where $m_X^2 = p_X^2$ denotes the squared invariant mass of particle X. In *s-channel* annihilation, s is the center of mass energy squared, and t and u are the squared four momentum transfer between particle A and C, and B and D, respectively.

A fundamental property of quantum field theory is that an incoming particle with momentum p can be interpreted as an outgoing anti-particle with momentum $-p$. This relates reaction 2.1.1 to the *t-channel* scattering $A(p_A) + \bar{C}(-p_C) \rightarrow \bar{B}(-p_B) + D(p_D)$, where now the Mandelstamm variable t determines the center of mass energy and s corresponds to the momentum transfer, and equivalently for the *u-channel*; compare Figure 2.1.1. In particular, *crossing symmetry* holds, which states that the scattering amplitude for all crossings is given by the same function of s, t, and u evaluated in different domains of s, t, and u. As a consequence, the scattering amplitude of reaction 2.1.1 can be obtained equivalently from either the s-, t-, or u-channel reaction.

2.1.2 Cross Sections

In the limit of large center of mass energy $\sqrt{s}$ and simultaneously small momentum transfer $\sqrt{|t|}$ hadronic scattering is characterized by the following features:

1. The scattering cross section rises slowly with energy.
2. Scattering happens predominantly in forward direction, i.e., the cross-section falls steeply with increasing momentum transfer.
3. This forward peak gets smaller with increasing energy (“shrinkage”).

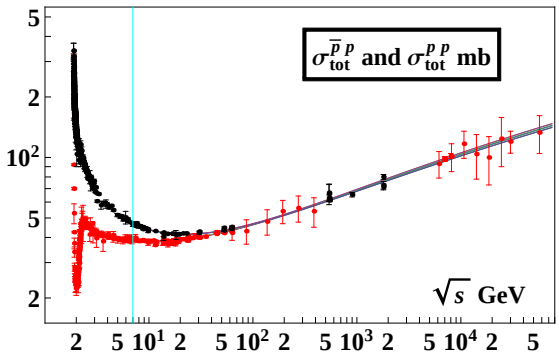

Figure 2.1.2: Total cross section for proton-proton (red) and antiproton-proton scattering (black). Figure from the PDG [17].

The similarities to the diffraction of light at an obstacle, where on a distant screen an intensity maximum is produced directly at the position of the obstacle, resulted in coining such scattering processes with the term *diffractive*. As typical example, the cross sections for proton-proton and antiproton-proton scattering are shown in Figure 2.1.2.

To explain diffractive scattering processes, Regge Theory exploits fundamental properties of the $\mathcal{S}$-matrix [15], such as Lorentz invariance, analyticity, or crossing symmetry, to derive the form of the scattering amplitude $\mathcal{A}$ for a given initial (A, B) and final state (C, D). The scattering amplitude can only depend on Lorentz invariant quantities, that is for reaction 2.1.1 on the three Mandelstamm variables. As only two of them are independent, $\mathcal{A} \equiv \mathcal{A}(s,t)$ can be written as a function of s and t alone.

The scattering amplitude is related to the cross section in two important ways. First, the *optical theorem* states that the total cross section is related to the imaginary part of the elastic forward amplitude

$$\sigma_{tot} = \frac{1}{s}\mathrm{Im}\,\mathcal{A}_{el}(s, t=0). \tag{2.1.6}$$

Elastic scattering here describes the case $A = C$ and $B = D$, in contrast to singly dissociative ($A! = C$ or $B! = D$) or doubly dissociative scattering ($A! = C$ and $B! = D$). Furthermore, the scattering amplitude also defines the differential cross section $\mathrm{d}\sigma/\mathrm{d}t$:

$$\frac{\mathrm{d}\sigma}{\mathrm{d}t} = \frac{1}{16\pi s^2}|\mathcal{A}(s,t)|^2. \tag{2.1.7}$$

$\mathcal{A}(s,t)$ can be written in a t-channel *partial wave expansion* in terms of Legendre polynomials P_l

$$\mathcal{A}(s,t) = 16\pi \sum_{l=0}^{\infty}(2l+1)A_l(t)P_l(\cos\theta_t), \tag{2.1.8}$$

with the scattering angle

$$\cos\theta_z = 1 + \frac{2s}{t - 4m^2}, \tag{2.1.9}$$

where in the high energy limit the masses m of all particles are assumed equal. The coefficients A_l are called the partial waves and have a propagator-like shape

$$A_l(t) \propto \frac{1}{t - M_l^2}, \tag{2.1.10}$$

which can be interpreted as a particle of mass M and spin l being exchanged in the scattering. Using equation Equation (2.1.6) and $P_l(z) \underset{z\to\infty}{=} z^J$, the cross section for such an exchange in the high energy limit $s \to \infty$ has the form

$$\sigma_{tot} \underset{z\to\infty}{\sim} s^{l-1}. \tag{2.1.11}$$

2.1.3 Regge Trajectories

Regge's idea [8, 9] was to continue $\mathcal{A}(t, s)$ to complex values of l, so that the partial waves $A_l(t)$ become a continuous function $A(l, t)$, which reduces to $A_l(t)$ for integer l. The poles of $A(l, t)$ then also become continuous and are located at given values of l and t, characterized by a relation

$$l = \alpha(t). \tag{2.1.12}$$

In analogy to the interpretation of the discrete poles as corresponding to the exchange of a particle, the continuous poles can be interpreted as the exchange of a more complex object, called a *reggeon*. The function $\alpha(t)$ characterizing such a reggeon is called a *Regge trajectory*. Reggeon exchange in the t-channel ($t < 0$) has a peculiar relation to s-channel ($t > 0$) resonances or bound states. A positive value t_L giving integer values $L = \mathrm{Re}\,\alpha(t_L)$ should correspond to such a bound state with mass $m^2 = t_L$ and spin L. This relates Regge trajectories to hadron families, such that hadrons with different spins and masses but otherwise identical quantum numbers should all lie on the same Regge trajectory.

In Figure 2.1.3 a selection of hadron families and the corresponding Regge trajectories are shown in a Chew-Frautschi plot [19, 20], where the spin of the particles is plotted against their mass. Surprisingly, the Regge trajectories for all hadron families can be parametrized by a simple line:

$$\alpha(t) = \alpha_0 + \alpha' \cdot t \tag{2.1.13}$$

with intercept α_0 and slope α'.

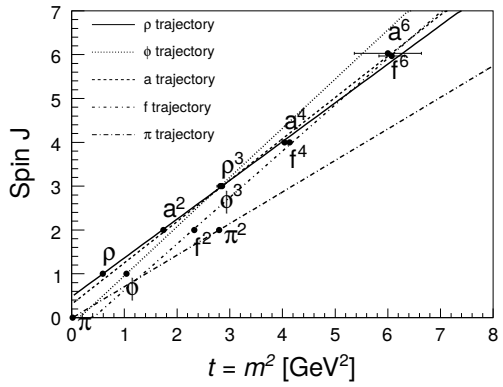

Figure 2.1.3: Various vector mesons and straight regge trajectories plotted in the Chew-Frautschi plane. Figure from Weber [18].

According to Equation (2.1.11) in the high energy limit the cross section for reggeon exchange is given by

$$\sigma_{tot} \underset{s\to\infty}{\sim} s^{\alpha_0 - 1}. \tag{2.1.14}$$

Additionally, the differential cross section $\mathrm{d}\sigma/\mathrm{d}t$ introduced in Equation (2.1.7) can be brought to the form

$$\frac{\mathrm{d}\sigma}{\mathrm{d}t} \sim s^{2(\alpha_0 - 1)} e^{-b|t|} \tag{2.1.15}$$

with the additional parameter

$$b = b_0 + 2\alpha' \ln(s). \tag{2.1.16}$$

So in particular, α_0 defines the high energy dependence of the cross section while α' is responsible for the aforementioned shrinkage of the forward peak.

2.1.4 Pomeron and Odderon

As it turns out, all of the hadronic Regge trajectories have an intercept $\alpha_0 \sim 0.5$. According to Equation (2.1.14) this results in a cross section falling with energy. Thus, to describe the observed rise of diffractive scattering cross sections at high energies, an additional Regge trajectory with an intercept larger than 1 has to be introduced. It is typically called the *pomeron* (after the Russian physicist Isaak Pomeranchuk) and its "canonical" Donnachie-Landshoff trajectory is given by

$$\alpha_{\mathbb{P}}(t) = 1.0808 + 0.25\,\mathrm{GeV}^{-2} \cdot t, \tag{2.1.17}$$

where the parameters have been obtained from fits to total cross sections of various scattering processes. The pomeron has the quantum numbers of the vacuum, i.e.,

in particular it is a P- and C- parity eigenstate with eigenvalue +1. Today, the pomeron is well established both theoretically and experimentally. In particular, within QCD it can be described as a colorless object containing no valence quarks. At lowest order, such an object is given by a two-gluon system [21, 22], but also more complex candidates, like the BFKL-pomeron having the form of a gluon ladder [23, 24], have been proposed.

The question that has not been answered as of yet, is whether the pomeron is the only object having an intercept close to 1 and thus solely characterizes hadronic scattering at very high energies. Indeed, already in the 1970s the observation that there are reggeons with both even and odd C-parity led to the proposition of an odd C-parity partner for the pomeron, which was hence called *odderon* [11]. A partner for the pomeron can also be anticipated from a QCD point of view, where in addition to pomeron like colorless objects formed by two valence gluons, also colorless objects formed by three gluons should be possible. However, while there are good theoretical arguments for the odderon, there is only little to no experimental evidence for its existence, as of yet. A comprehensive discussion of the status of the odderon in soft high energy processes is given for example by Ewerz [10].

The existence of an odderon would have important consequences for the phenomenology of diffractive scattering in the high energy limit. One key signature of the odderon is that, unlike the pomeron, it couples differently to particles and antiparticles, thus leading to different particle-particle and antiparticle-particle cross sections in the high energy limit. In case of pomeron exchange only, those would be the same. In addition, as it carries different quantum numbers than the pomeron, odderon exchange opens the door for new final states. An explicit example is considered in Section 2.2.1, where in the high energy limit diffractive photoproduction of an f_2 meson is only possible via odderon exchange.

As was shown first by Brodsky et al. [25] a contribution from the $C = -1$ odderon in scattering processes can also interfere with the $C = +1$ pomeron contribution and by that give rise to asymmetries among the final state particles. In this thesis a concrete example for this, namely charge asymmetries in the diffractive photoproduction of oppositely charged pion pairs, which have been proposed by Ginzburg et al. [12] and Ivanov et al. [13], are studied. However, before these asymmetries are further discussed in Section 2.2, it is necessary to establish a connection between the photon and the soft hadronic scattering processes discussed so far.

2.1.5 Hadronic Structure of the Photon

In quantum field theory an undisturbed photon is allowed to fluctuate into fermion-antifermion pairs. In particular, it can fluctuate into strongly interacting

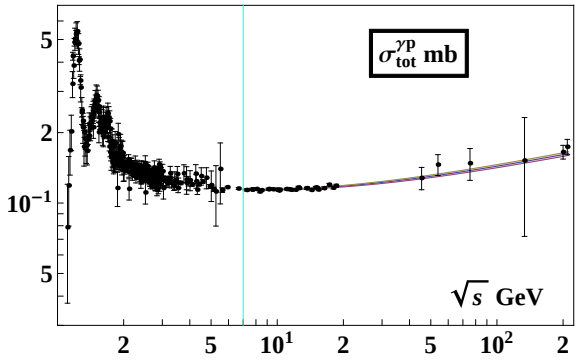

Figure 2.1.4: Total cross section for photon-proton scattering. Figure from the PDG [17].

quarks and antiquarks that then give it hadronic properties. The timescale over which such fluctuations exist [26] can be longer than the timescale of the strong interaction, thus allowing the pairs of virtual quarks to interact and form bound states. These states ought to have the quantum numbers of the photon

$$J^{PC} = 1^{--}, \tag{2.1.18}$$

where J is the spin of the photon, and P and C are the parity and charge eigenvalues, respectively. Thus only (virtual) vector meson states are allowed to be formed. In *Vector Dominance Models* (VDM) [27–31] the hadronic part of the photon is modeled by a superposition of light vector mesons, such as the ρ^0, ϕ, ω, J/ψ, $\psi(2S)$, and Υ.

This hadronic part of the photon gives rise to strong contributions in photon-hadron scattering processes, which can even dominate the cross sections [31]. As a consequence photon-hadron cross sections exhibit all the features of hadron-hadron cross sections. Compare for example the photon-proton cross section shown in Figure 2.1.4 with the proton-proton cross section in Figure 2.1.2. However, photon-hadron cross sections are suppressed by a factor α_{em}, the electromagnetic coupling constant, because of the necessity of the photon to oscillate into a vector meson before it can interact strongly.

2.2 $\pi^+\pi^-$ Photoproduction

In this thesis, charge asymmetries in the photoproduction of oppositely charged pion pairs, i.e., in the reaction

$$\gamma^{(*)}(q, \epsilon) + p(p, \mathfrak{s}) \to \pi^+(k_1) + \pi^-(k_2) + p'(p', \mathfrak{s}'), \tag{2.2.1}$$

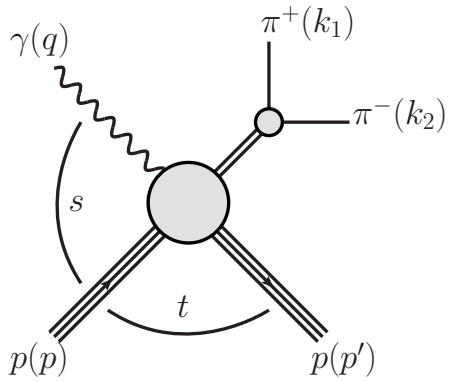

Figure 2.2.1: Generic diagram of (resonant) $\pi^+\pi^-$ photoproduction.

are studied. In the expression (2.2.1) q, and p denote the four momenta of the ingoing photon and proton, and k_1, k_2, and p' the four momenta of the outgoing pions and proton, respectively. ϵ denotes the polarization of the photon, which in the case of virtual photons γ^* can also be longitudinal. The respective spin states of the incoming and outgoing proton are denoted by $\mathfrak{s}$ and $\mathfrak{s}'$. In the following, unpolarized photons and protons are assumed and ϵ, $\mathfrak{s}$, and $\mathfrak{s}'$ are dropped. Furthermore, only proton elastic scattering, i.e., the case $p'^2 = m_p^2$ with m_p denoting the proton mass, is considered.

From the five involved four momentum vectors $q,\ p,\ k_1,\ k_2$, and p' in total 15 Lorentz invariants, i.e., scalar products, can be formed, which the process can depend on. Considering energy momentum conservation

$$q + p = k_1 + k_2 + p' \tag{2.2.2}$$

and the mass-shell constraints

$$p^2 = p'^2 = m_p^2, \quad \text{and} \quad k_1^2 = k_2^2 = m_\pi^2 \tag{2.2.3}$$

only six of them are independent and can be used to express all others. One can choose for example

$$q^2,\ s,\ t,\ m^2_{\pi^+\pi^-},\ \theta_{k_1},\ \text{and}\ \varphi_{k_1} \tag{2.2.4}$$

where $s = (p+q)^2$ is the photon-proton center of mass energy squared, $t = (p-p')^2$ the squared proton momentum transfer and $m^2_{\pi^+\pi^-} = (k_1 + k_2)^2$ the invariant mass square of the $\pi^+\pi^-$ system, and θ_{k_1} and φ_{k_1} are the polar and azimuthal angle of the π^+. Suitable reference frames for the pion angles are discussed in Section 2.2.3. In the context of this thesis, the photon-proton center of mass energy is equivalently denoted with $W_{\gamma p}$.

In a recently published paper [32], which also contains results obtained within this thesis, a previously presented soft scattering model by Ewerz et al. [14] was

applied one the photoproduction of pion pairs, i.e., reaction (2.2.1). This model is the theoretical basis for the study of asymmetries to be performed in this thesis and a brief introduction to it's basic concepts and ingredients is thus given in this section. All the details can be found in the publications by Bolz et al. [32] and Ewerz et al. [14].

Reaction 2.2.1 has contributions from both electromagnetic and strong processes which, in principle, should be fully calculable by QED and QCD, respectively. However, the nature of the strong interaction - namely the aforementioned running of the coupling constant α_s with energy - limits the phenomena that can actually be calculated from the QCD-Lagrangian. In particular, for soft scattering processes such as reaction 2.2.1, which happen preferably at high energy $\sqrt{s}$ and low momentum transfer t, the absence of a definite energy scale results in their incalculability within the framework of perturbative QCD.

To be able to describe soft scattering processes quantitatively, anyhow, Ewerz et al. developed an effective model in the spirit of Regge Theory. While Regge Theory itself is very limited in its predictions, giving little more than the $\sqrt{s}$ and t dependence of the cross section in the high energy limit, this model provides an effective Lagrangian. In particular, the soft interactions are described in terms of the exchange of reggeons, the pomeron and the odderon, for which propagators and couplings to various hadrons are given. This allows to explicitly calculate Feynman diagrams and thus to access soft scattering processes in full detail.

2.2.1 Matrix Elements

In Figure 2.2.2 the Feynman diagrams for all processes contributing to $\pi^+\pi^-$ photoproduction that are considered here are shown. The necessary ingredients to calculate the matrix elements, most importantly coupling constants and propagators are provided by Ewerz et al. [14], details on the calculation are given in the publication by Bolz et al. [32].

The most important contribution comes from resonant $\pi^+\pi^-$ production via vector mesons, as shown in 2.2.2 a) where the photon oscillates into either the $\rho \equiv \rho(770)$, $\omega \equiv \omega(782)$, or $\rho' \equiv \rho'(1415)$ meson. The vector mesons then interact strongly with the proton by exchange of a pomeron $\mathbb{P}$ or one of the reggeons f_{2R} and a_{2R}. In order to preserve C-parity, from the reggeons included in the model only those with even C-parity ($C = +1$) can be exchanged. The pomeron and the $C = +1$ reggeons are treated as effective tensor particles. After the scattering the vector meson decays into the considered $\pi^+\pi^-$ final state. It can be shown that $\pi^+\pi^-$ photoproduction in the model has a high energy dependence of the cross section in agreement with Regge theory, see also Chapter 3.

In addition to 2.2.2 a), various other contributions are included in the calculations. Among those, the matrix elements 2.2.2 b), c), and d) describe $\pi^+\pi^-$ production

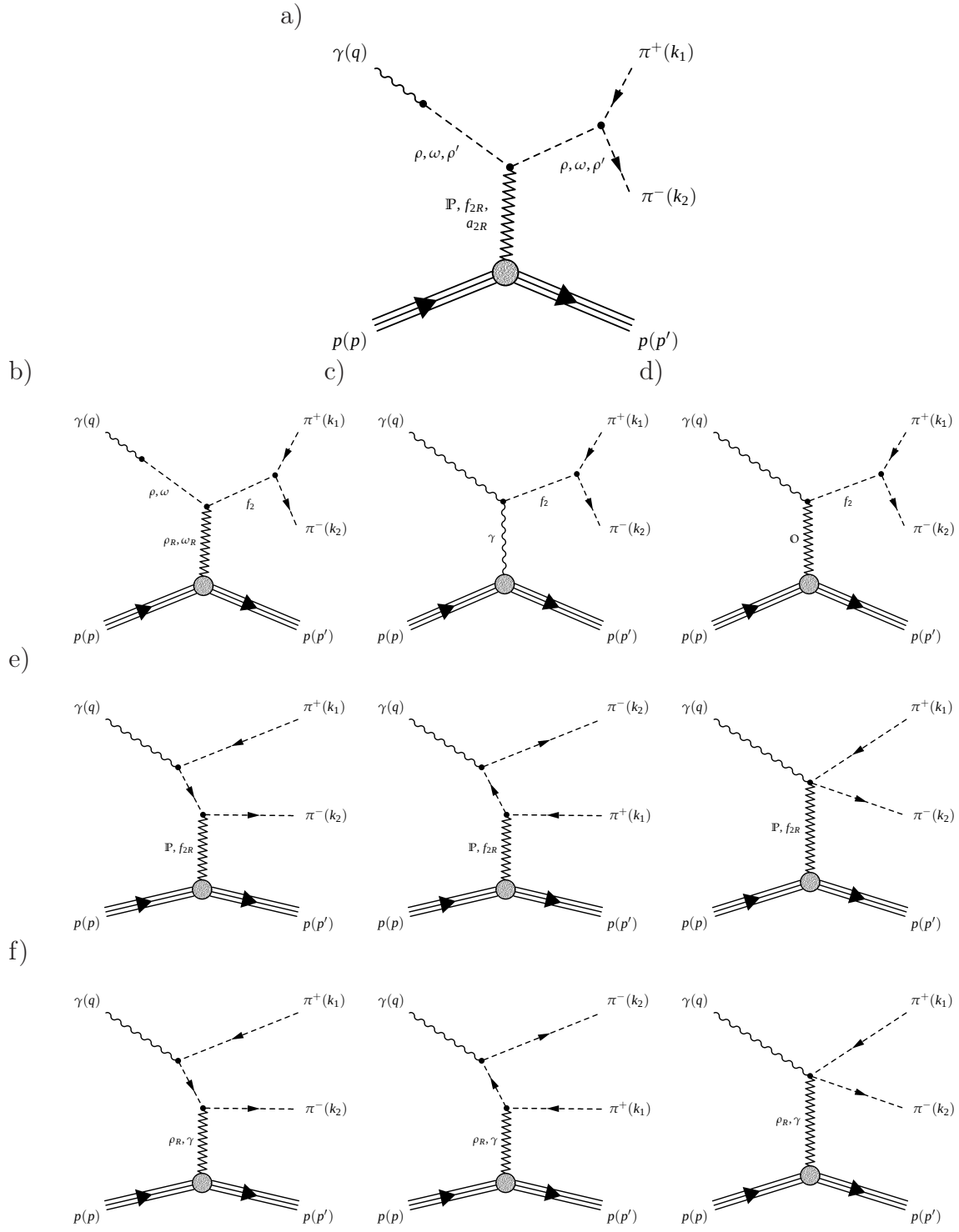

Figure 2.2.2: Amplitudes contributing to $\pi^+\pi^-$ photoproduction in the model by Ewerz et al. [14]. In a) the Feynman diagram for the resonant states $\rho(770)$, $\omega(782)$ and $\rho'(1450)$ is shown, in b), c), and d) diagrams describing $f_2(1270)$ production, and in c) and d) non-resonant $\pi^+\pi^-$ production mechanisms are shown (sorted by $C = +1$ and $C = -1$ exchange particles). Figure from Bolz et al. [32].

via an $f_2(1270)$ resonance. The $f_2(1270)$ has the quantum numbers $J^{PC} = 2^{++}$ and consequently quantum fluctuations of a photon ($J^{PC} = 1^{--}$) into an f_2 meson are not possible. Furthermore, to ensure conservation of the multiplicative C-parity the exchange particle with the proton must have $C = -1$, so in particular pomeron exchange is not allowed in this case. Instead, an f_2 can be produced if the photon oscillates into a vector meson and a $C = -1$ reggeon such as a ρ_R or ω_R is exchanged with the proton, as shown in 2.2.2 b). Alternatively, there is the purely electromagnetic Primakoff process [33] as drawn in 2.2.2 c) where two photons form an f_2. A third possibility for f_2 resonance production is shown in 2.2.2 d), where the photon couples to a possible odderon ($\mathbb{O}$), which has not been observed yet but is included in the model as an effective vector particle, nonetheless. As the cross section for reggeon exchange drops with energy, photoproduction of an f_2 resonance at high energies is only possible via odderon exchange or the well constrained QED Primakoff process. Observing an f_2 resonance in excess of what can be expected from QED alone would thus be direct evidence for the odderon.

Finally, a third class of processes for non-resonant $\pi^+\pi^-$ production are considered, corresponding to the diagrams shown in 2.2.2 e) and f). They include exchange of the pomeron, various reggeons and the photon. In particular, exchange of both $C = +1$ (2.2.2 e)) and $C = -1$ particles (2.2.2 f)) is possible.

Ewerz et al. [14] provide all means to calculate all of the discussed Feynman diagrams and thus the full scattering amplitude for the process 2.2.1. The full matrix element can formally be written as:

$$\mathcal{M}^{\mu}_{\mathfrak{s},\,\mathfrak{s}'}(k_1, k_2, p', q, p)\epsilon_\mu = \langle \pi^+(k_1),\ \pi^-(k_2),\ p(p',\,\mathfrak{s}')|\mathcal{T}|\gamma(q,\epsilon),\ p(p,\,\mathfrak{s})\rangle. \quad (2.2.5)$$

Here $q,\ p,\ k_1,\ k_2$ and p' are the four-momenta of the particles, $\mathfrak{s}$ and $\mathfrak{s}'$ are the respective spin states of the incoming and outgoing proton, and ϵ is the photon polarization vector. $\mathcal{T}$ is the scattering matrix. In particular, $\mathcal{M}^{\mu}_{\mathfrak{s},\,\mathfrak{s}'}$ is the sum of the matrix elements for all the sub-processes, i.e.,

$$\mathcal{M}^{\mu}_{\mathfrak{s},\,\mathfrak{s}'} = \mathcal{M}^{\mu,(a)}_{\mathfrak{s},\,\mathfrak{s}'} + \mathcal{M}^{\mu,(b)}_{\mathfrak{s},\,\mathfrak{s}'} + \mathcal{M}^{\mu,(c)}_{\mathfrak{s},\,\mathfrak{s}'} + \mathcal{M}^{\mu,(d)}_{\mathfrak{s},\,\mathfrak{s}'} + \mathcal{M}^{\mu,(e)}_{\mathfrak{s},\,\mathfrak{s}'} + \mathcal{M}^{\mu,(f)}_{\mathfrak{s},\,\mathfrak{s}'}. \quad (2.2.6)$$

The total cross section for elastic $\pi^+\pi^-$ photoproduction can then be calculated using the common formula [17]

$$\mathrm{d}\sigma = \frac{(2\pi)^4}{2(s - m_p^2)} \left(-\frac{1}{4} \sum_{\mathfrak{s},\,\mathfrak{s}'} \mathcal{M}^{*}_{\mu,\,\mathfrak{s}',\,\mathfrak{s}} \mathcal{M}^{\mu}_{\mathfrak{s}',\,\mathfrak{s}} \right) \mathrm{d}\Pi_3, \quad (2.2.7)$$

where the squared matrix element is averaged over the initial and summed over the final state proton spin states, normalized and integrated over the three particle phase space

$$d\Pi_3 = \frac{1}{(2\pi)^9} \frac{d^3k_1}{2k_1^0} \frac{d^3k_2}{2k_2^0} \frac{d^3p'}{2p'^0} \delta^{(4)}(k_1 + k_2 + p' - q - p). \quad (2.2.8)$$

2.2.2 Asymmetries

At high scattering energies, $W_{\gamma p} \equiv \sqrt{s} \gtrsim 10\,\mathrm{GeV}$, $\pi^+\pi^-$ photoproduction is completely dominated by ρ^0 production via pomeron exchange. Details are discussed in Chapter 3. All other processes shown in Figure 2.2.2 have cross sections that are smaller by at least one order of magnitude. f_2 production, where the odderon appears in the model, is even suppressed by three orders of magnitude and gives the smallest contribution. Consequently, there is little hope to observe the f_2 resonance and it is practically impossible to establish the presence of the odderon by a precise measurement of the total $\gamma\, p \to \pi^+\pi^-\, p$ cross section. However, as it turns out the odderon can have a significant influence on the differential cross sections. Interference of the $C = -1$ contributions, where a $C = -1$ particle is exchanged and the odderon could contribute, with the $C = +1$ processes leads to charge asymmetries. These asymmetries can be rather large and thus might allow to establish the odderon, after all.

To understand how those charge asymmetries arise it is necessary to consider the matrix elements for the various sub processes as denoted in Equation (2.2.6). When looking at the full mathematical expressions given by Bolz et al. [32] it turns out that the matrix elements depend on k_1 and k_2, i.e., the four-momenta of the two pions, only in terms of

$$(k_1 + k_2) \text{ and } (k_1 - k_2). \tag{2.2.9}$$

Furthermore it can be shown that under the exchanged $k_1 \leftrightarrow k_2$, i.e., the exchange $\pi^+ \leftrightarrow \pi^-$, matrix elements for processes where a $C = +1$ particle is exchange transform like

$$\mathcal{M}_{C=+1}(k_1, k_2, p', q, p) = -\mathcal{M}_{C=+1}(k_2, k_1, p', q, p), \tag{2.2.10}$$

while those where a $C = -1$ particle is exchanged transform like

$$\mathcal{M}_{C=-1}(k_1, k_2, p', q, p) = +\mathcal{M}_{C=-1}(k_2, k_1, p', q, p). \tag{2.2.11}$$

As a consequence the squared sum of all matrix elements can be split into two parts: One that pics up a minus sign under the exchange $k_1 \leftrightarrow k_2$ and one that is not affected by this exchange, at all. That is, one can write

$$\mathcal{R} \coloneqq -\frac{1}{4} \sum_{\mathfrak{s},\, \mathfrak{s}'} \mathcal{M}^*_{\mu,\, \mathfrak{s}',\, \mathfrak{s}} \mathcal{M}^{\mu}_{\mathfrak{s}',\, \mathfrak{s}} \equiv \mathcal{R}_+ + \mathcal{R}_-, \tag{2.2.12}$$

where

$$\mathcal{R}_+(k_1, k_2, p', q, p) = +\mathcal{R}_+(k_2, k_1, p', q, p) \tag{2.2.13}$$

and

$$\mathcal{R}_-(k_1, k_2, p', q, p) = -\mathcal{R}_-(k_2, k_1, p', q, p). \tag{2.2.14}$$

From the way the matrix elements transform it is clear that $\mathcal{R}_-$ contains all interference terms of $C = +1$-exchange processes with $C = -1$-exchange processes while $\mathcal{R}_+$ contains the remains, i.e., explicitly:

$$\mathcal{R}_+ = -\frac{1}{4}\sum_{\mathfrak{s},\,\mathfrak{s}'}\left[\mathcal{M}^{(a+e)*}_{\mu,\,\mathfrak{s}',\,\mathfrak{s}}\mathcal{M}^{(a+e)\mu}_{\mathfrak{s}',\,\mathfrak{s}} + \mathcal{M}^{(b+c+d+f)*}_{\mu,\,\mathfrak{s}',\,\mathfrak{s}}\mathcal{M}^{(b+c+d+f)\mu}_{\mathfrak{s}',\,\mathfrak{s}}\right], \text{ and} \tag{2.2.15}$$

$$\mathcal{R}_- = -\frac{1}{4}\sum_{\mathfrak{s},\,\mathfrak{s}'}\left[\mathcal{M}^{(a+e)*}_{\mu,\,\mathfrak{s}',\,\mathfrak{s}}\mathcal{M}^{(b+c+d+f)\mu}_{\mathfrak{s}',\,\mathfrak{s}} + \mathcal{M}^{(b+c+d+f)*}_{\mu,\,\mathfrak{s}',\,\mathfrak{s}}\mathcal{M}^{(a+e)\mu}_{\mathfrak{s}',\,\mathfrak{s}}\right]. \tag{2.2.16}$$

For the total cross section, the minus sign picked up by $\mathcal{R}_-$ under $k_1 \leftrightarrow k_2$ does not play a rôle, because of the phase space integration over k_1 and k_2 in Equation (2.2.7). However, when looking at differential cross sections where the integral over the phase space is not (fully) performed, $\mathcal{R}_-$ gives rise to an asymmetry under the exchange of the pions, i.e., a charge asymmetry. This can be easily seen by taking the differential cross section

$$\frac{\mathrm{d}\sigma}{\mathrm{d}\Pi_3}(k_1, k_2, p', q, p), \tag{2.2.17}$$

where $\mathrm{d}\Pi_3$ is the full 3 particle phase space, and use it to define the charge asymmetry

$$\begin{aligned}\mathcal{A}(k_1, k_2, p', q, p) &\coloneqq \frac{\dfrac{\mathrm{d}\sigma}{\mathrm{d}\Pi_3}(k_1, k_2, p', q, p) - \dfrac{\mathrm{d}\sigma}{\mathrm{d}\Pi_3}(k_2, k_1, p', q, p)}{\dfrac{\mathrm{d}\sigma}{\mathrm{d}\Pi_3}(k_1, k_2, p', q, p) + \dfrac{\mathrm{d}\sigma}{\mathrm{d}\Pi_3}(k_2, k_1, p', q, p)} \\ &= \frac{\mathcal{R}(k_1, k_2, p', q, p) - \mathcal{R}(k_2, k_1, p', q, p)}{\mathcal{R}(k_1, k_2, p', q, p) + \mathcal{R}(k_2, k_1, p', q, p)} \\ &= \frac{\mathcal{R}_-(k_1, k_2, p', q, p)}{\mathcal{R}_+(k_1, k_2, p', q, p)}.\end{aligned} \tag{2.2.18}$$

While Equation (2.2.18) illustrates how the asymmetry under the exchange $\pi^+ \leftrightarrow \pi^-$ is a direct consequence of the interference of the C-even and C-odd contributions, it is not very practical. In particular, many variables that appear there are completely unrelated to the charge asymmetry. To find a more suitable definition of a charge asymmetry, it is best to consider the consequences of exchanging the pions with each other in the $\pi^+\pi^-$ rest frame. There, the relation

$$\vec{k} \equiv \vec{k}_1 + \vec{k}_2 = 0 \tag{2.2.19}$$

holds, so that exchanging $\pi^+ \leftrightarrow \pi^-$, i.e., $k_1 \leftrightarrow k_2$, corresponds to

$$\vec{k}_1 \to -\vec{k}_1, \quad \text{and} \quad \vec{k}_2 \to -\vec{k}_2. \tag{2.2.20}$$

If $\vec{k}_1$ is expressed in polar coordinates with a polar angle $\theta_{k_1} \in [0, \pi]$ and an azimuthal angle $\varphi_{k_1} \in [-\pi, \pi]$ this transformation writes as

$$\vec{k}_1 \to -\vec{k}_1 \quad \Leftrightarrow \quad \begin{cases} \varphi_{k_1} \to \varphi_{k_1} + \pi \\ \theta_{k_1} \to \pi - \theta_{k_1} \end{cases} . \tag{2.2.21}$$

A charge asymmetry thus manifests itself in an asymmetry of the angular distributions, i.e., the differential cross section in θ and φ, in the $\pi^+\pi^-$ center of mass system. In Section 3.2 in particular the asymmetry in $\frac{\mathrm{d}\sigma}{\mathrm{d}\cos\theta_{k_1}}$ is studied, where $\cos\theta_{k_1}$ instead of θ_{k_1} is used for simplicity. It is defined according to Equation (2.2.18) as:

$$\mathcal{A}(\cos\theta_{k_1}) \coloneqq \frac{\dfrac{\mathrm{d}\sigma}{\mathrm{d}(\cos\theta_{k_1})}(+\cos\theta_{k_1}) - \dfrac{\mathrm{d}\sigma}{\mathrm{d}(\cos\theta_{k_1})}(-\cos\theta_{k_1})}{\dfrac{\mathrm{d}\sigma}{\mathrm{d}(\cos\theta_{k_1})}(+\cos\theta_{k_1}) + \dfrac{\mathrm{d}\sigma}{\mathrm{d}(\cos\theta_{k_1})}(-\cos\theta_{k_1})}, . \tag{2.2.22}$$

An asymmetry in φ can be defined equivalently. Some important remarks concerning the choice of a suitable reference frame are made in Section 2.2.3.

From the asymmetry in the differential cross sections a *total charge asymmetry* $\hat{\mathcal{A}}$ can be defined which can depend on various variables, such as $m_{\pi^+\pi^-}$ or t.

$$\hat{\mathcal{A}}(m_{\pi^+\pi^-},\ t, \dots) \coloneqq \frac{\sigma_+(m_{\pi^+\pi^-},\ t, \dots) - \sigma_-(m_{\pi^+\pi^-},\ t, \dots)}{\sigma_+(m_{\pi^+\pi^-},\ t, \dots) + \sigma_-(m_{\pi^+\pi^-},\ t, \dots)} \tag{2.2.23}$$

with

$$\sigma_\pm \coloneqq \int_0^1 \frac{\mathrm{d}\sigma(\gamma p \to \pi^+\pi^- p)}{\mathrm{d}(\cos\theta_{k_1})} (\pm\cos\theta_{k_1})\, \mathrm{d}(\cos\theta_{k_1}), \tag{2.2.24}$$

and equivalently for any other asymmetry variable.

2.2.3 Reference Frames

What remains to be specified, is the references frame in which the π^+ angles θ_{k_1} and φ_{k_1} are evaluated. This turns out to be a crucial point for studying charge asymmetries. Several possible reference frames exist, of which the so-called proton-Jackson [34] and photon-Jackson [35] frame are used in this thesis. They are both defined in the $\pi^+\pi^-$ center of mass system, where $\vec{k_1} = -\vec{k_2}$. The polar

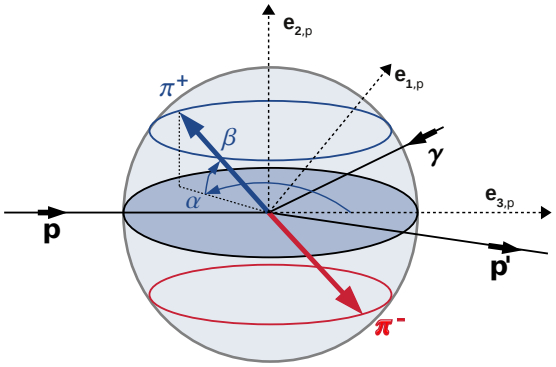

Figure 2.2.3: Illustration of the angles α and β introduced in the text. Figure from Bolz et al. [32] and adapted.

axis in the proton-Jackson frame is given by the proton momentum $\vec{p}$ so that in particular

$$\cos\theta_{k_1,p} = \hat{p} \cdot \hat{k_1} \tag{2.2.25}$$

where $\hat{p} = \vec{p}/|\vec{p}|$ and $\hat{k_1} = \vec{k_1}/|\vec{k_1}|$. Correspondingly, the photon momentum defines the polar axis in the photon-Jackson frame. The remaining two axes are given by

$$\hat{e}_{1,p} = \frac{-\vec{p'} + \hat{p}\,(\hat{p} \cdot \vec{p'})}{|\hat{p} \times \vec{p'}|} \quad \text{and} \quad \hat{e}_{2,p} = -\frac{\hat{p} \times \vec{p'}}{|\hat{p} \times \vec{p'}|} \tag{2.2.26}$$

in the proton-Jackson and

$$\hat{e}_{1,\gamma} = \frac{-\vec{p'} + \hat{q}\,(\hat{q} \cdot \vec{p'})}{|\hat{q} \times \vec{p'}|} \quad \text{and} \quad \hat{e}_{2,\gamma} = -\frac{\hat{q} \times \vec{p'}}{|\hat{q} \times \vec{p'}|} \tag{2.2.27}$$

in the photon-Jackson frame, with $\hat{q} = \vec{q}/|\vec{q}|$. In particular, it is noteworthy that $\hat{e}_{2,p} = -\hat{e}_{2,q}$.

To access the full asymmetry information, the differential cross section needs to be studied in both angles simultaneously. For a two dimensional asymmetry however, a smarter choice of angular coordinates than θ_{k_1} and φ_{k_1} is possible. The scattering $\gamma\, p \rightarrow \pi^+\pi^-\, p$ is governed by the strong and electromagnetic force and thus conserves parity. With $\vec{p}$, $\vec{q}$, and $\vec{p'}$ all being in the same plane because of momentum conservation, parity invariance corresponds to an invariance under mirroring the process at this reaction plane. This motivates the introduction of a new set of angles α and β. As illustrated in Figure 2.2.3, β is the elevation angle with respect to the reaction plane and α is the azimuth in the plane with respect to the proton momentum. They can be calculated using the relations

$$\sin\beta = \hat{k_1} \cdot \hat{e}_{2,p}, \tag{2.2.28}$$

$$\cos\beta\cos\alpha = \hat{k_1} \cdot \hat{e}_{3,p}, \text{ and} \tag{2.2.29}$$

$$\cos\beta\sin\alpha = \hat{k_1} \cdot \hat{e}_{1,p}. \tag{2.2.30}$$

The parity transformation, i.e., mirroring the process at the reaction plane, then simply corresponds to $\beta \to -\beta$. It is in particular noteworthy, that the relation

$$\cos\theta_{k_1,p} = \cos\beta\cos\alpha \tag{2.2.31}$$

holds.

Concerning the charge asymmetries, the transformation $\vec{k_1} \to -\vec{k_1}$ corresponds to $\alpha \to \alpha + \pi$ and $\beta \to -\beta$. Considering parity invariance, an asymmetry can thus only appear in α. Consequently, the α-β frame is much more natural to study asymmetries and in the following the proton-Jackson and photon-Jackson frame are only considered because they are wildly used. For studying the full two-dimensional asymmetry, the distribution in α and β used instead, with the asymmetry defined as:

$$\mathcal{A}(\alpha,\beta) \coloneqq \frac{\frac{\mathrm{d}^2\sigma}{\mathrm{d}\alpha\mathrm{d}\beta}(\alpha,\beta) - \frac{\mathrm{d}^2\sigma}{\mathrm{d}\alpha\mathrm{d}\beta}(\alpha+\pi,\beta)}{\frac{\mathrm{d}^2\sigma}{\mathrm{d}\alpha\mathrm{d}\beta}(\alpha,\beta) + \frac{\mathrm{d}^2\sigma}{\mathrm{d}\alpha\mathrm{d}\beta}(\alpha+\pi,\beta)}. \tag{2.2.32}$$

2.2.4 Model Parameters and Limitations

The discussed model represents an effective field theory which should in principle follow from QCD. However, for reasons discussed previously, the reaction cannot be calculated starting directly from the QCD Lagrangian. As a consequence, the model depends on a large set of unknown parameters which determine couplings, Regge-trajectories form factors and such. A list of which is provided by Bolz et al. [32, Table 1].

For some of the parameters the measurements have been performed and they are known fairly well; others underlie theoretical restrictions. Yet others are not known at all. For the plots presented in Chapter 3 the values provided by Bolz et al. [32] are used. Some of these are chosen more or less arbitrarily and in particular not tuned to adapt the model to experimental data. A detailed study of parameter dependencies goes beyond the scope of this thesis. However, eventually a fit of the model parameters to suitable experimental data should be performed or at least the parameters could be tuned towards a better agreement with data.

2.3 A New Event Generator for $\pi^+\pi^-$ Photoproduction

The model discussed in the previous section provides a set of matrix elements which can be used to calculate a cross section for $\pi^+\pi^-$ photoproduction using the

formula given in Equation (2.2.7). However, performing the phase space integral is an all but trivial task. Since finding an analytic solution for the integral - if it even exists - is impossible one has to calculate it numerically. A variety of algorithms can be used to estimate integrals. At higher dimensions the Monte Carlo integration scheme [17] turns out to be the most efficient.

Monte Carlo Integration

Monte Carlo Integration can be used to estimate the integral of a function $f(\vec{x})$ of arbitrary dimension over a volume $\Omega = \int \mathrm{d}\vec{x}$. The simple approach is to uniformly sample N random points $\vec{x_1} \dots \vec{x_N}$ on Ω. The integral can then be approximated by

$$\frac{1}{\Omega} \int_\Omega f(\vec{x})\, \mathrm{d}\vec{x} \simeq \frac{1}{N} \sum_{i=1}^{N} f(\vec{x_i}) \simeq \langle f(\vec{x}) \rangle. \tag{2.3.1}$$

If $f(\vec{x})$ varies strongly over Ω importance sampling is a more efficient alternative. Here the points $\vec{x_i}$ are not sampled uniformly but rather according to probability density $p(\vec{x})$ which is chosen such that it reflects the variation of $f(\vec{x})$. That is, points $\vec{x}$ where $f(\vec{x})$ is large are sampled with a higher probability. The integral in this case is estimated via

$$\frac{1}{\Omega} \int_\Omega f(\vec{x})\, \mathrm{d}\vec{x} = \frac{1}{\Omega} \int_\Omega \frac{f(\vec{x})}{p(\vec{x})}\, p(\vec{x})\, \mathrm{d}\vec{x} = \frac{1}{N} \sum_{i=1}^{N} \frac{f(\vec{x_i})}{p(\vec{x_i})}, \tag{2.3.2}$$

where the property $\int p(\vec{x})\, \mathrm{d}\vec{x} = \Omega$ is used.

Event Generator

The total and differential cross sections that are presented in Chapter 3 are obtained from an event generator written by Sauter [36] which relies on the Monte Carlo integration scheme just described. While a full description of the technicalities of this generator goes beyond the scope of this thesis, the basic concepts and ideas behind it shall be briefly discussed along the lines of Appendix D the publication by Bolz et al. [32].

The generator performs the following steps: First, the spin-sum of all the matrix elements is calculated using the FeynCalc package [37]. It is then expressed in terms of five independent variables, where for convenience

$$m_{\pi^+\pi^-},\ t,\ \varphi_{p'},\ \cos\theta_\pi,\ \text{and}\ \varphi_\pi \tag{2.3.3}$$

are chosen. $m_{\pi^+\pi^-}$ is the invariant $\pi^+\pi^-$ mass, t the proton momentum transfer, $\varphi_{p'}$ the azimuthal angle of the outgoing proton in the γp rest frame, and θ_π and φ_π are the angles of one of the pions in the $\pi^+\pi^-$ rest frame. The three particle phase space in Equation (2.2.7) can be expressed in terms of these variables:

$$\mathrm{d}\Pi_3 = \frac{1}{(2\pi)^9}\frac{1}{16 m_{\pi^+\pi^-}}\frac{\lambda^{1/2}(m^2_{\pi^+\pi^-}, m^2_\pi, m^2_\pi)}{\lambda^{1/2}(s, m_p^2, m_q^2)}\,\mathrm{d}m_{\pi^+\pi^-}\,\mathrm{d}t\,\mathrm{d}\varphi_{p'}\,\mathrm{d}(\cos\theta_\pi)\,\mathrm{d}\varphi_\pi. \tag{2.3.4}$$

Here, $s = W_{\gamma p}$ is proton photon center of mass energy, m_p, m_π and $m_q = 0$ are the masses of proton, pions and photon, respectively and

$$\lambda(x, y, z) = x^2 - 2(y + z)x + (y - z)^2. \tag{2.3.5}$$

The accessible phase space is given by [38]

$$G(s, t, m^2_{\pi^+\pi^-}, m_p^2, m_q^2, t) \leq 0 \quad \text{and} \tag{2.3.6}$$

$$G(m^2_{\pi^+\pi^-}, t_\pi, m_\pi^2, t, m_p^2, m_\pi^2) \leq 0 \tag{2.3.7}$$

with

$$\begin{aligned} G(x, y, z, u, v, w) = {} & x^2y + xy^2 + z^2u + zu^2 + v^2w + vw^2 + xzw && (2.3.8)\\ & + xuv + yzw + yuw - yuw - xy(z + u + v + w) && (2.3.9)\\ & - zu(x + y + v + w) - vw(x + y + z + u) && (2.3.10) \end{aligned}$$

and $t_\pi = (q - k_\pi)^2$, with k_π being the four-momentum of one pion in the $\pi^+\pi^-$ rest frame.

Putting everything together the differential cross section in Equation (2.2.7) takes the form[1]

$$\begin{aligned} \mathrm{d}\sigma = {} & \frac{(\hbar c)^2}{2(s - m_p^2)}\,|\mathcal{R}|^2\,\frac{1}{(2\pi)^9}\frac{1}{8}\frac{1}{2m_{\pi^+\pi^-}}\frac{\lambda^{1/2}(m^2_{\pi^+\pi^-}, m^2_\pi, m^2_\pi)}{\lambda^{1/2}(s, m_p^2, m_q^2)} \\ & \times \Theta(-G(s, t, m^2_{\pi^+\pi^-}, m_p^2, m_q^2, t))\;\Theta(-G(m^2_{\pi^+\pi^-}, t_\pi, m_\pi^2, t, m_p^2, m_\pi^2)) \\ & \times\; \mathrm{d}m_{\pi^+\pi^-}\;\mathrm{d}t\,\mathrm{d}\varphi_{p'}\,\mathrm{d}(\cos\theta_\pi)\,\mathrm{d}\varphi_\pi. \end{aligned} \tag{2.3.11}$$

To evaluate Equation (2.3.11) N phase space points

$$(m_{\pi^+\pi^-},\ t,\ \varphi_{p'},\ \cos\theta_\pi,\ \varphi_\pi)_i, \quad i = 1 \ldots N, \tag{2.3.12}$$

are randomly sampled. The right hand side of Equation (2.3.11) without the volume element is evaluated for each of those points and divided by N to define an associated weight w_i. In the spirit of MC integration, the total cross section for $\gamma\, p \,\to\, \pi^+\pi^-\, p$ is then given by the sum of these weights.

Generally, the phase space points can be interpreted as weighted events for the process $\gamma\, p \,\to\, \pi^+\pi^-\, p$. The distribution of any variable in a sample of such events then gives the corresponding differential cross section in said variable. The plots presented in Chapter 3 are obtained in this fashion.

[1] The factor $(\hbar c)^2$ is explicitly introduced here in order to get results in S.I. units.

2.4 Diffractive Electron Proton Scattering

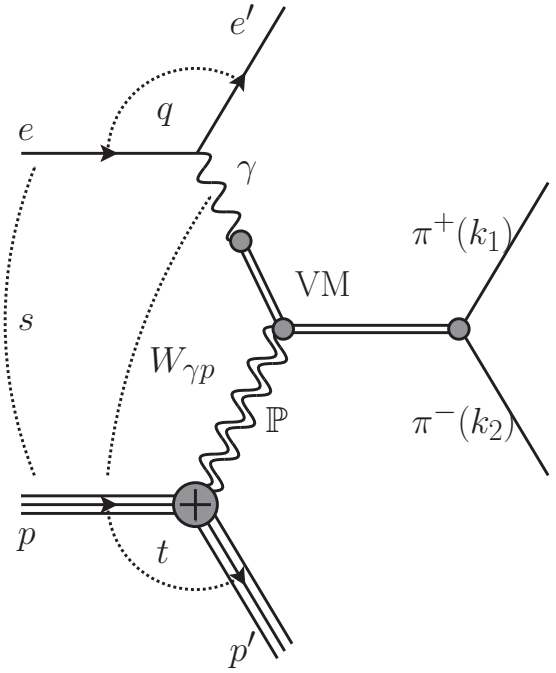

Figure 2.4.1: Feynman diagram for diffractive electron-proton scattering process $e\,p \to e\,\pi^+\pi^-\,p$ in the Vector Dominance Model including symbolic definitions of various kinematic variables.

To put diffractive photon-proton scattering as discussed in Section 2.2 into context with the HERA electron-proton collider, diffractive electron-proton scattering is briefly discussed here. Figure 2.4.1 shows a generic Feynman diagram for such a scattering process. The incoming electron emits a photon, which in the VDM oscillates into a virtual vector meson. In the high energy limit, this vector meson interacts strongly with the incoming proton by exchange of a pomeron ($\mathbb{P}$) or a reggeon. By the interaction the vector meson is put onto its mass shell, i.e., it becomes a real particle. In the context of diffractive $\pi^+\pi^-$ production, in the figure the vector meson is shown to decay into a $\pi^+\pi^-$ final state.

Electron-proton scattering thus allows to study the hadronic properties of the photon. The big advantage over direct photon scattering experiments is that the electron can be accelerated to very high energies and in turn become a source of highly energetic photons. Similar studies have been performed at the HERA electron-proton collider experiments H1 and ZEUS, where ρ^0 [39–54], ϕ [40, 43, 46, 50, 55–58], ω [59, 60], J/ψ [43, 46, 47, 52, 61–71], $\psi(2S)$ [72, 73], and Υ [67, 74–76] production were investigated.

2.4.1 *ep* Scattering Kinematics

On the basis of Figure 2.4.1 kinematic relations of the scattering process

$$e\,p \;\rightarrow\; e\,\pi^{+}\pi^{-}\,p \tag{2.4.1}$$

relevant for this thesis are introduced. The four-momenta of the incoming(outgoing) electron and proton are denoted with $e(e')$ and $p(p')$, respectively. The proton is allowed to scatter both *elastically*, i.e.,

$$p'^{2} = m_p^2, \tag{2.4.2}$$

where m_p is the proton mass, and *dissociatively*, i.e., p' is an excited state with

$$p'^{2} > m_p^2. \tag{2.4.3}$$

k_1 and k_2 denote the four-momenta of the π^+ and π^- meson in the final state, such that the four-momentum of the intermediate vector meson is given by

$$k = k_1 + k_2. \tag{2.4.4}$$

In the following, given a four-momentum p the subscripts E, x, y, z, and t denote its energy, x, y, z and transverse component, where the latter is given by

$$p_t = \sqrt{p_x^2 + p_y^2}; \tag{2.4.5}$$

and θ_p and φ_p denote its polar and azimuthal angle.

In reaction 2.4.1 the Lorentz invariant variables

$$s = (e+p)^2, \quad q^2 = (e-e')^2, \quad \text{and } t = (p-p')^2 \tag{2.4.6}$$

denote the electron-proton center of mass energy, the electron and the proton momentum transfer. For the t-channel processes considered here $t < 0\,\mathrm{GeV}^2$ holds.

$q = e - e'$ is the four-momentum of the (virtual) photon. It can be used to define the photon-proton center of mass energy

$$W_{\gamma p}^2 = (q+p)^2. \tag{2.4.7}$$

As $q^2 < 0\,\mathrm{GeV}^2$, historically, the *photon virtuality* is introduced as

$$Q^2 = -q^2, \tag{2.4.8}$$

so that it is a positive number. Two kinematic regimes are distinguished:

- In the *photoproduction* regime $Q^2 = 0\,\mathrm{GeV}^2$, i.e., the photon is on-shell and real.
- In the *deep inelastic scattering* (DIS) regime $Q^2 > 0\,\mathrm{GeV}^2$ and the photon is virtual.

Under experimental conditions the boundary between these two regimes is blurred and typically given by the acceptance of the detector for the scattered electron.

Further variables used in the context of deep inelastic electron-proton scattering are the the fraction of the electron energy carried by the photon

$$y = \frac{q \cdot p}{e' \cdot p}, \tag{2.4.9}$$

and the Bjorken scaling variable

$$x = \frac{Q^2}{2q \cdot p}, \tag{2.4.10}$$

i.e., the fraction of the proton-momentum carried by the struck parton in DIS in the infinite momentum frame. y and x relate to other variables in the following ways:

$$Q^2 = xys, \text{ and} \tag{2.4.11}$$
$$W^2_{\gamma p} = ys - Q^2 - m_p^2. \tag{2.4.12}$$

3 $\gamma p \to \pi^+\pi^- p$ Model Studies

The tools described in Section 2.3 allow to evaluate the model introduced in Section 2.2 and to study many features of $\pi^+\pi^-$ photoproduction. In the following, two of the main aspects are investigated. First, total and differential model cross sections are qualitatively compared to the measured ones in various kinematic variables. A quantitative comparison is not done here, because several parameters in the model are only estimated and would have to be measured first. Secondly, $\pi^+\pi^-$ charge asymmetries are studied. Of particular interest is of course the question how they can be measured and whether they open the door for a possible discovery of the odderon.

3.1 Cross Sections

The model should describe the two main characteristics of diffractive photon-proton scattering: the behavior of the total cross section as a function of the photon-proton center of mass energy $W_{\gamma p}$, and the proton momentum transfer dependence of the differential cross section $\frac{\mathrm{d}\sigma(\gamma p \to \pi^+\pi^- p)}{\mathrm{d}t}$ (see also Section 2.1). In Figure 3.1.1 the total cross section as a function of $W_{\gamma p}$ is compared with experimental data. The cross section as given by the model is integrated over the invariant dipion mass in the range

$$2m_\pi \leq m_{\pi^+\pi^-} \leq 1.5\,\mathrm{GeV} \tag{3.1.1}$$

and over the proton momentum transfer in the range

$$0 \leq |t| \leq 1\,\mathrm{GeV}^2. \tag{3.1.2}$$

The shown experimental data points, which are obtained from measurements at the HERA electron-proton collider as well as fixed target experiments [48, 51, 53], are taken under comparable conditions. At large energies, $W_{\gamma p} \gtrsim 10\,\mathrm{GeV}$, the model describes the data very well. The discrepancies at lower energies come to no surprise as the model is explicitly constructed for high energies. For it to be valid also at low energies, more processes must be taken into account.

In addition to the full prediction, various contributions from sub-processes are shown. At all energies the scattering is dominated by vector meson production.

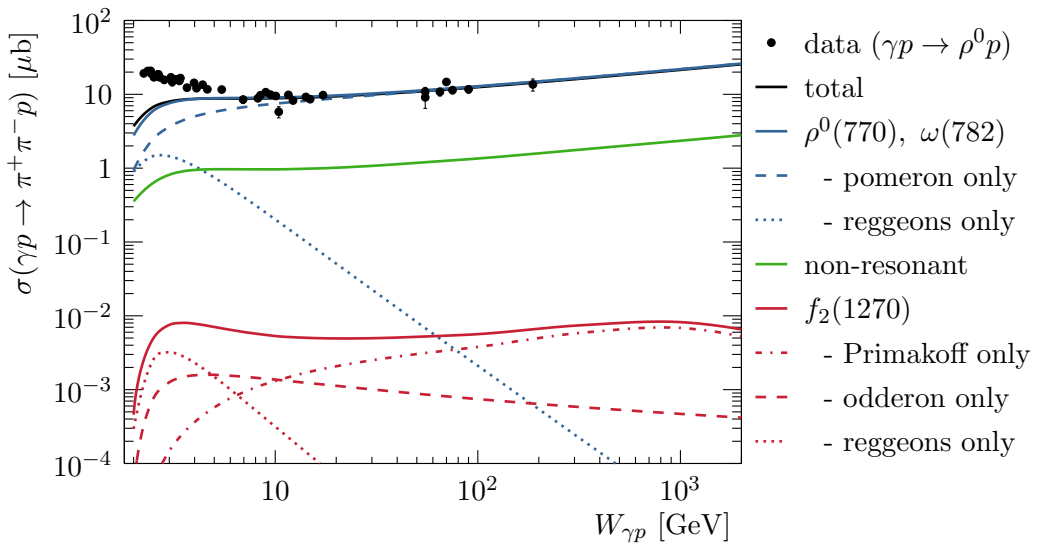

Figure 3.1.1: Total cross section $\sigma(\gamma\, p \to \pi^+\pi^-\, p)$ as a function of the center of mass energy $W_{\gamma p}$. The cross section is integrated over $2m_\pi \leq m_{\pi^+\pi^-} \leq 1.5$ GeV and $0 \leq |t| \leq 1\,\mathrm{GeV}^2$. The full model, as well as individual contributions from vector mesons, non-resonant processes and the f_2 resonance are shown. For comparison, measured data from the HERA H1 [51] and ZEUS [48, 53] experiments and several fixed target experiments as referenced in ZEUS publication [48] are also plotted. Figure published by Bolz et al. [32].

This can be further split up into contributions from reggeon and pomeron exchange. While the reggeon contributions steeply drop with $W_{\gamma p}$, the exchange of a pomeron causes the slight rise in the total cross section with energy. The the second largest contribution to $\pi^+\pi^-$ photoproduction in the considered mass range comes from the non-resonant processes shown in 2.2.2 e) and f). It is about one order of magnitude smaller than vector meson production and rises in a similar manner with $W_{\gamma p}$ due to the pomeron exchange contribution. The production cross section for the f_2 lies approximately three orders of magnitude below that for the vector mesons. As for the vector mesons, reggeon exchange only contributes at very low energies, where it is dominant. At intermediate energies odderon exchange and the Primakoff process take over. While odderon exchange falls slowly towards larger energies, the Primakoff cross section rises such that at high $W_{\gamma p}$ it dominates f_2 meson production.

In the following, differential cross sections are evaluated at fixed

$$W_{\gamma p} = 30\,\mathrm{GeV}. \tag{3.1.3}$$

This value is chosen because here the odderon contribution relative to the pomeron

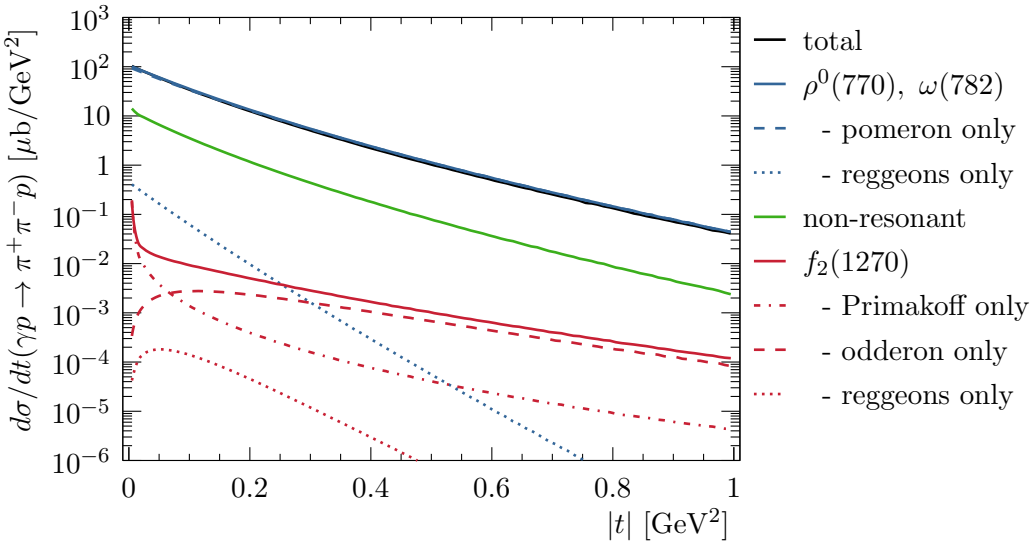

Figure 3.1.2: Differential cross section $\frac{d\sigma(\gamma p \to \pi^+\pi^- p)}{dt}$ as a function of the proton momentum transfer t. The cross section is evaluated at $W_{\gamma p} = 30\,\text{GeV}$ and integrated over $2m_\pi \leq m_{\pi^+\pi^-} \leq 1.5\,\text{GeV}$. The full model, as well as individual contributions from vector mesons, non-resonant processes and the f_2 resonance are shown. Figure published by Bolz et al. [32].

is strongest so that odderon effects can be studied best.

The differential cross section $\frac{\mathrm{d}\sigma(\gamma p \to \pi^+\pi^- p)}{\mathrm{d}t}$ as a function of the proton momentum transfer t is presented in Figure 3.1.2. As discussed, it is calculated for fixed $W_{\gamma p} = 30\,\text{GeV}$ and integrated over the mass range defined in Equation (3.1.1). Again, the full model as well as contributions from various individual sub-processes are shown. The full cross section shows the very steep exponential fall that is also present in the experimental data, see for example Figure 3.1.3. A direct comparison with the measured data is not possible here, because of the incompatible energy ranges.

By themselves not all of the shown contributions exhibit the exponential dependence on t. Most prominently, the cross section for f_2 production diverges[1] at $t = 0\,\text{GeV}^2$. This divergence originates from the photon exchange, whereas in contrast, odderon and reggeon contributions drop down towards small $|t|$. This is all expected and theoretically understood, as explained by Bolz et al. [32, Appendix C]. Concerning the odderon contribution, it should be noted that it dominates f_2 production in the range $|t| \gtrsim 0.1\,\text{GeV}^2$.

[1] An actual diverging cross section is stopped by the accessible phase space with a minimum possible $|t|$.

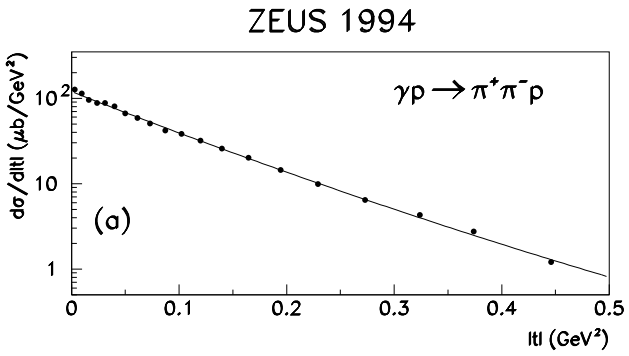

Figure 3.1.3: Measured differential cross section $\frac{\mathrm{d}\sigma(\gamma p \to \pi^+\pi^- p)}{\mathrm{d}t}$ as a function of the proton momentum transfer t. The cross section is integrated over $50 \leq W_{\gamma p} \leq 100\,\mathrm{GeV}$ and $0.55 \leq m_{\pi^+\pi^-} \leq 1.2\,\mathrm{GeV}$. Figure from the ZEUS Collaboration [48].

In Figure 3.1.4 the differential cross section $\frac{\mathrm{d}\sigma(\gamma p \to \pi^+\pi^- p)}{\mathrm{d}m_{\pi^+\pi^-}}$ is shown as a function of invariant dipion mass. The cross section is given at fixed $W_{\gamma p} = 30\,\mathrm{GeV}$ and integrated over $|t|$ in the range given in Equation (3.1.2). In addition to the full model, the contributions from the ρ^0, ω, f_2, and ρ' mesons are also shown, as well

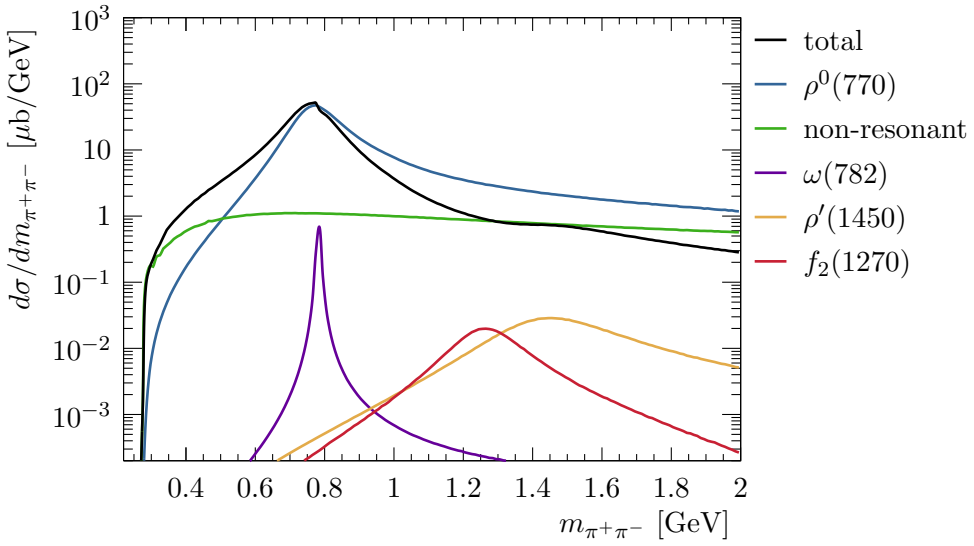

Figure 3.1.4: Differential cross section $\frac{d\sigma(\gamma\, p \to \pi^+\pi^-\, p)}{dm_{\pi^+\pi^-}}$ as a function of the invariant dipion mass. The cross section is evaluated at fixed $W_{\gamma p} = 30\,\mathrm{GeV}$ and integrated over $0 \leq |t| \leq 1\,\mathrm{GeV}^2$. The full model, as well as the contributions from the ρ, ω, f_2 and ρ' resonances and from the non-resonant processes are shown. Figure published by Bolz et al. [32].

as the non-resonant contribution. The overall cross section is largely dominated by the ρ^0 resonance with other contributions being several orders of magnitude smaller. However, those processes can still have significance via interference effects.

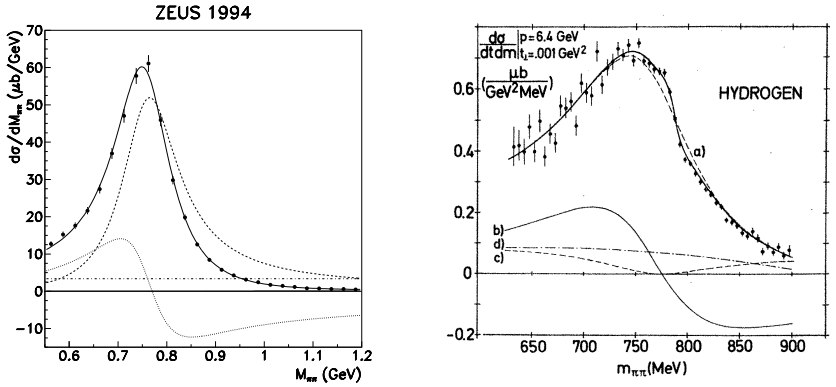

Figure 3.1.5: Left: Measured differential cross section $\frac{\mathrm{d}\sigma(\gamma p \to \pi^+\pi^- p)}{\mathrm{d}m_{\pi^+\pi^-}}$ as a function of $m_{\pi^+\pi^-}$ integrated over the $50 < W_{\gamma p} < 100\,\mathrm{GeV}$ and $|t| < 0.5\,\mathrm{GeV}^2$. The data is fitted with the model given in Equation (3.1.4). The resonant contribution to the model A, the constant contribution B, and the mixed term are also shown individually. Figure from the ZEUS Collaboration [48].
Right: Measured differential cross section $\frac{\mathrm{d}^2\sigma(\gamma\, p \to \pi^+\pi^-\, p)}{\mathrm{d}t\, \mathrm{d}m_{\pi^+\pi^-}}$ as a function of $m_{\pi^+\pi^-}$. The fit illustrates how the ρ^0-ω-interference introduces the steep edge right on top of the ρ^0 mass peak. Figure from Alvensleben et al. [77].

The largest consequence of such an interference effect is the glaring difference in the shapes of the full model and the isolated ρ^0 resonance. At masses below the ρ^0 peak the cross section in the full model is enhanced while at masses above the peak it is reduced with respect to the ρ^0 contribution. This skewing of the ρ^0 resonance shape is a clear characteristic seen in experimental data. As an example, a measurement of the dipion mass distribution performed at the ZEUS experiment [48] is shown in Figure 3.1.5. There the measured ρ^0 resonance clearly deviates from the expected Breit-Wigner [78] shape in the discussed manner.

Drell [79, 80] and Söding [81] first explained this skewing as a consequence of an interference of the ρ^0 with non-resonant contributions. From this assumption a phenomenological shape for the differential cross section was derived, which has been successfully used to describe the measurements:

$$\frac{\mathrm{d}\sigma(\gamma p \to \pi^+\pi^- p)}{\mathrm{d}m_{\pi^+\pi^-}}(m_{\pi^+\pi^-}) = \left| A \frac{\sqrt{m_{\pi^+\pi^-} m_\rho \Gamma_\rho}}{m^2_{\pi^+\pi^-} - m^2_\rho + i m_\rho \Gamma_\rho} + B \right|^2 . \tag{3.1.4}$$

In Equation (3.1.4) the contribution A, corresponding to a resonance described by a regular Breit-Wigner with nominal mass m_ρ and momentum dependent width Γ_ρ, is extended at amplitude level by a constant, non-resonant contribution B. On the cross section level, this gives rise to a mixed, i.e., interference, term causing the skewing of the ρ^0 resonance. A fit of Equation (3.1.4) to ZEUS data is also shown in Figure 3.1.6, together with the contributing two direct terms and the interference term.

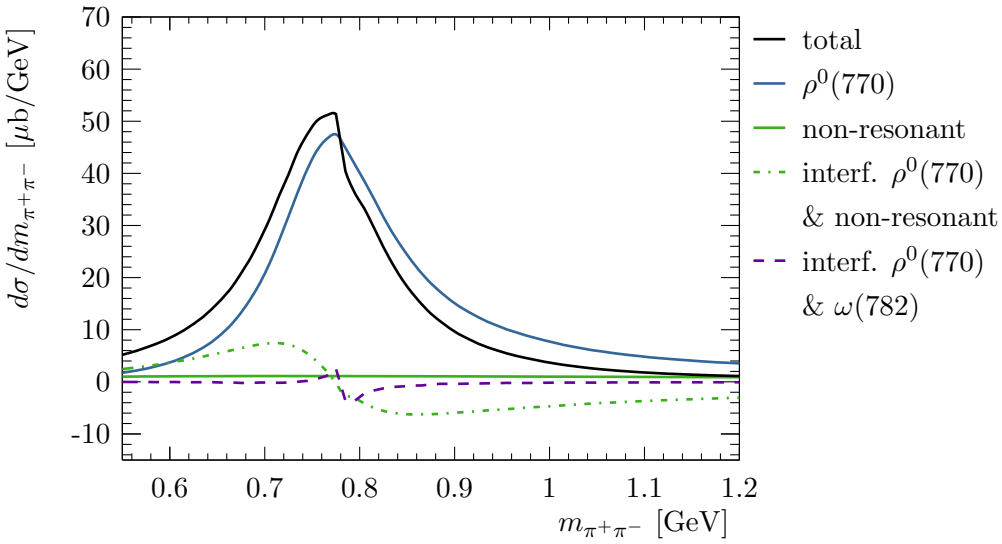

Figure 3.1.6: Differential cross section $\frac{d\sigma(\gamma p \to \pi^+\pi^- p)}{dm_{\pi^+\pi^-}}$ as a function of the invariant dipion mass $m_{\pi^+\pi^-}$. The cross section is evaluated at fixed $W_{\gamma p} = 30\,\text{GeV}$ and integrated over $0 \leq |t| \leq 1\,\text{GeV}^2$. The full model, as well as the ρ^0 and the non-resonant contribution are shown together with the interference of the ρ^0 with the non-resonant contribution, as well as with the ω. Figure published by Bolz et al. [32].

In the model the interference of the ρ^0 with the non-resonant contribution as the origin of the skewing becomes explicit. Figure 3.1.6 shows in analogy to the ZEUS plot the differential cross section $\frac{\mathrm{d}\sigma(\gamma p \to \pi^+\pi^- p)}{\mathrm{d}m_{\pi^+\pi^-}}$ split up into direct and interference terms. A direct comparison of the model with the data at this point is not possible for two reasons. Again, the data are shown for different energies and, more importantly, the exact ρ^0 shape is very sensitive to the choice of model parameters which have not been tuned yet.

A second characteristic feature of the ρ^0 shape is a very steep fall off directly above the ρ_0 mass. It comes from an interference of the ρ^0 with the ω. In Figure 3.1.5 the dipion mass distribution measured in $\pi^+\pi^-$ photoproduction on a hydrogen target

is shown [77] where this fall off is clearly present. The responsible interference term as it results from the model is included in Figure 3.1.6 as well.

One last, small interference effect to be noticed is the plateau seen at the ρ' mass in the region $m_{\pi^+\pi^-} \simeq 1.5\,\text{GeV}$, see Figure 3.1.4. While the ρ' resonance is not directly visible, it interfering with other contributions is responsible for this plateau.

3.2 Angular Distributions and Charge Asymmetries

In the previous section total and differential cross sections for $\pi^+\pi^-$ photoproduction as calculated in the model are discussed. While the total cross section is clearly dominated by ρ^0 resonance production, the other contributions can have a significant influence on the differential cross section via interference effects, as can be seen in particular in the skewing of the ρ^0 shape. Interference effects play a similarly important role in the angular distributions and in particular give rise to the charge asymmetries discussed in Section 2.2.2.

The angular distribution of $\cos\theta_{k_1,p}$, i.e., the cosine of the polar angle of the positive pion in the proton-Jackson frame, is shown in Figure 3.2.1. It is considered in two $\pi^+\pi^-$ mass windows separately: one around the ρ^0 resonance:

$$0.45 < m_{\pi^+\pi^-} < 1.1\,\text{GeV}, \tag{3.2.1}$$

and a second one around the f_2 resonance:

$$1.1 < m_{\pi^+\pi^-} < 1.35\,\text{GeV}. \tag{3.2.2}$$

The full model as well as various significant contributions are shown.

In the ρ^0 mass window, the angular distribution of the full model is again clearly dominated by vector meson production and the f_2 contributions are not even visible on the scale. In particular it is perfectly symmetric under the transformation $\cos\theta_{k_1,p} \to -\cos\theta_{k_1,p}$. In the f_2 mass window on the other hand, the f_2 resonance has a significant influence, which presents itself in the asymmetry of the distribution. The totally antisymmetric contribution to the differential cross section $\frac{\mathrm{d}\sigma(\gamma p\to\pi^+\pi^- p)}{\mathrm{d}(\cos\theta_{k_1,p})}(\cos\theta_{k_1,p})$, coming from the $\mathcal{R}_-$ part of the squared amplitude as introduced in Section 2.2.2, enhances the cross section for negative and reduces it for positive values of $\cos\theta_{k_1,p}$. In the f_2 mass window, $\mathcal{R}_-$ obtains the largest contributions from the interference of $\pi^+\pi^-$ production via the f_2 meson with both the production via the vector mesons, and non-resonant production. The two interference terms contribute with opposite sign, however because of a difference

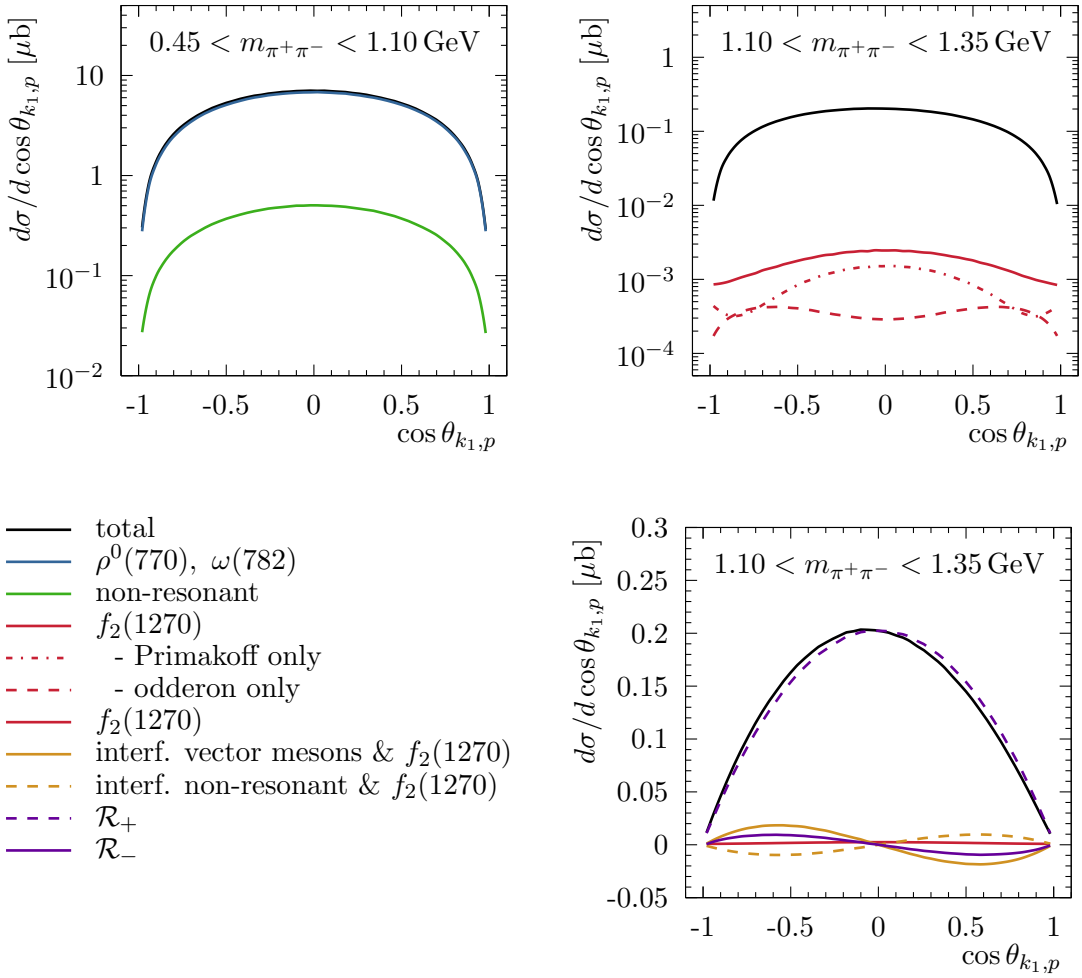

Figure 3.2.1: Differential cross section $\frac{\mathrm{d}\sigma(\gamma p \to \pi^+\pi^- p)}{\mathrm{d}(\cos\theta_{k_1,p})}(\cos\theta_{k_1,p})$ in the proton-Jackson reference frame. The cross section is shown integrated over $W_{\gamma p} = 30\,\text{GeV}$ and $0 \leq |t| \leq 1\,\text{GeV}^2$. It is considered separately in the ρ^0 mass window (top left) and the f_2 mass window (top right). The distribution in the f_2 mass window is also shown on a linear scale (bottom right). The total model as well as interesting contributions as listed in the legend are shown. Figure published by Bolz et al. [32].

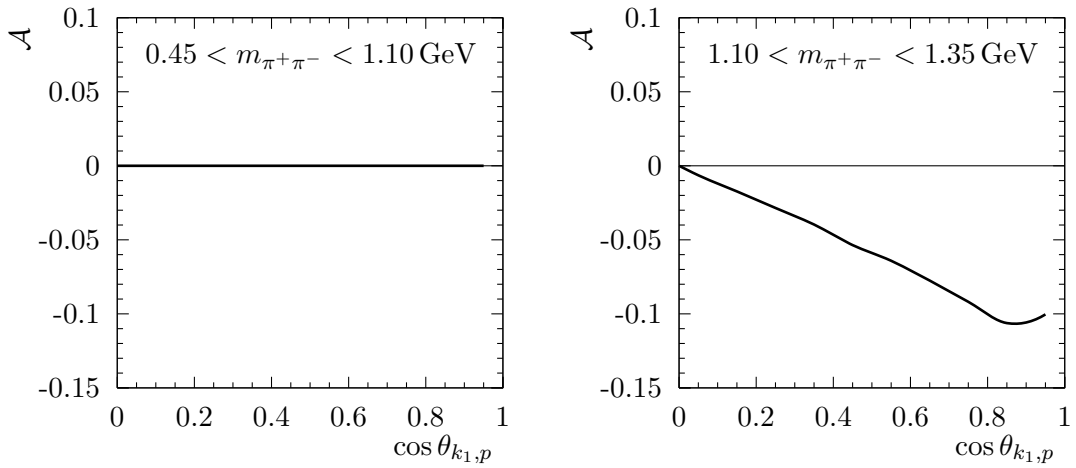

Figure 3.2.2: Asymmetry in the proton-Jackson frame as a function of $\cos\theta_{k_1,p}$ in the ρ^0 (left) and f_2 mass window (right). The asymmetries are shown for $W_{\gamma p} = 30\,\mathrm{GeV}$ and $0 \leq |t| \leq 1\,\mathrm{GeV}^2$.

in strength a net asymmetric term remains. As expected, the interference terms are much larger than the direct f_2 contribution to the angular distribution.

From the differential cross section $\frac{\mathrm{d}\sigma(\gamma p \to \pi^+\pi^- p)}{\mathrm{d}(\cos\theta_{k_1,p})}(\cos\theta_{k_1,p})$ an asymmetry $\mathcal{A}(\cos\theta_{k_1,p})$ can be calculated according to Equation (2.2.22). It is shown for the ρ^0 and f_2 mass window in Figure 3.2.2. In compliance with the discussion along Figure 3.2.1 an asymmetry is present in the f_2 mass window, only. As is discussed in Section 2.2.2, this asymmetry corresponds to a charge asymmetry under the exchange $\pi^+ \leftrightarrow \pi^-$.

To obtain a complete picture of this charge asymmetry, also the asymmetry in the φ_{k_1} distribution should be studied. The φ_{k_1} distribution is shown in Figure 3.2.3, again for various model contributions and separately for the ρ^0 and the f_2 mass window. According to Equation (2.2.21), a charge asymmetry corresponds to an asymmetry of the differential cross section $\frac{\mathrm{d}\sigma(\gamma p \to \pi^+\pi^- p)}{\mathrm{d}\varphi}(\varphi_{k_1})$ under $\varphi_{k_1} \to \varphi_{k_1} + \pi$. As is expected from the discussion along Figure 3.2.1, such an asymmetry is present in the f_2, but not in the ρ^0 mass region.

With respect to measuring a charge asymmetry, the choice of reference frame turns out to be quite crucial. In Figure 3.2.4 the differential cross section $\mathrm{d}\sigma/\mathrm{d}\cos\theta_{k_1,\gamma}(\cos\theta_{k_1,\gamma})$ and asymmetry $\mathcal{A}(\cos\theta_{k_1,\gamma})$ in the f_2 mass window are shown in the photon-Jackson frame. The asymmetry in $\cos\theta_{k_1,\gamma}$ exhibits a sign flip at about 0.8 and thus has a completely different quality than the asymmetry in $\cos\theta_{k_1,p}$. This becomes particularly important, if in a measurement only total asymmetries according to Equation (2.2.23) are considered, where integrating over a sign flip might hide the presence of an asymmetry.

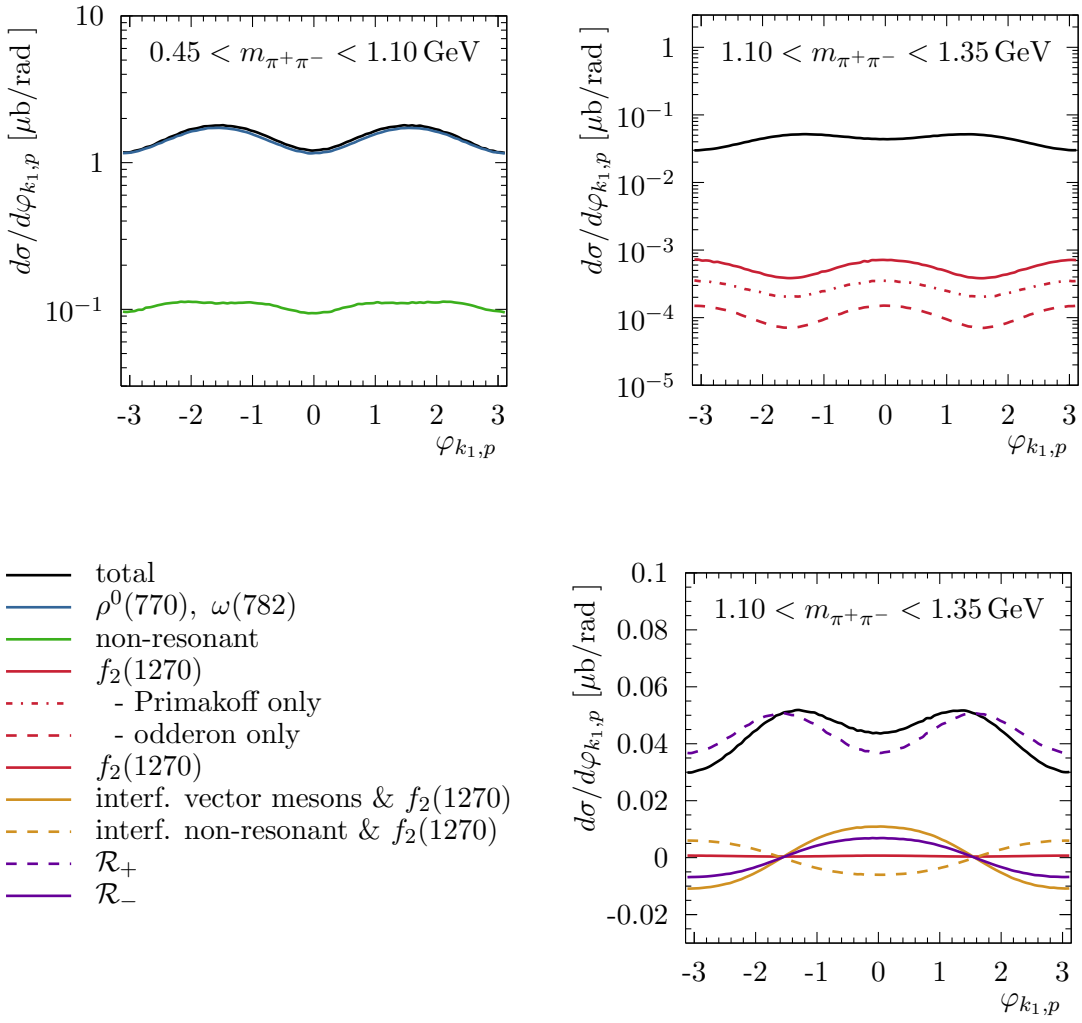

Figure 3.2.3: Differential cross section $\frac{d\sigma(\gamma p\to\pi^+\pi^- p)}{d\varphi}(\varphi_{k_1})$ in the proton-Jackson reference frame. The cross section is shown integrated over $W_{\gamma p} = 30\,\text{GeV}$ and $0 \leq |t| \leq 1\,\text{GeV}^2$. It is considered separately in the ρ^0 mass window (top left) and the f_2 mass window (top right). The distribution in the f_2 mass window is also shown on a linear scale (bottom right). The total model as well as interesting contributions as listed in the legend are shown.

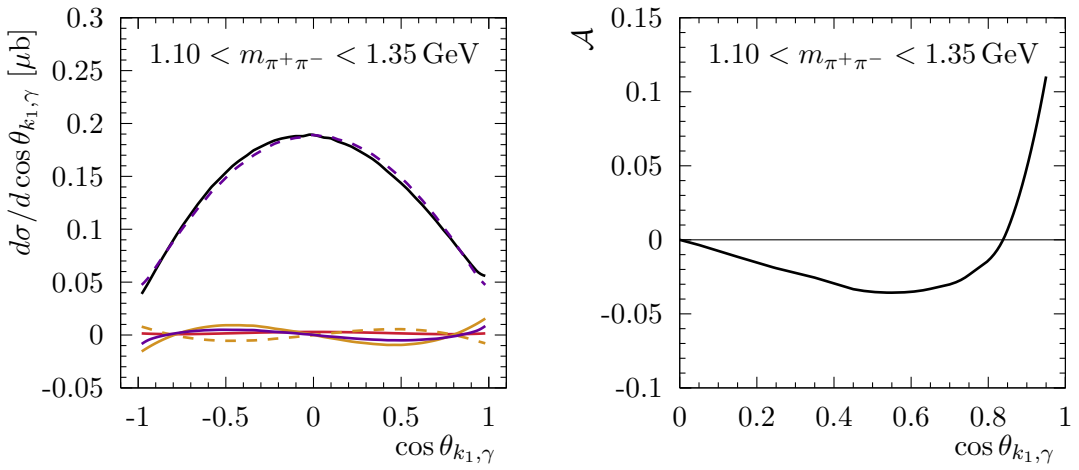

Figure 3.2.4: Differential cross section $\frac{\mathrm{d}\sigma(\gamma p \to \pi^+\pi^- p)}{\mathrm{d}(\cos\theta_{k_1,p})}(\cos\theta_{k_1,\gamma})$ (left) and asymmetry $\mathcal{A}(\cos\theta_{k_1,\gamma})$ (right) in the photon-Jackson frame for the f_2 mass window. Both are shown for $W_{\gamma p} = 30\,\text{GeV}$ and $0 \leq |t| \leq 1\,\text{GeV}^2$. For a definition of the various curves, see Figure 3.2.1.

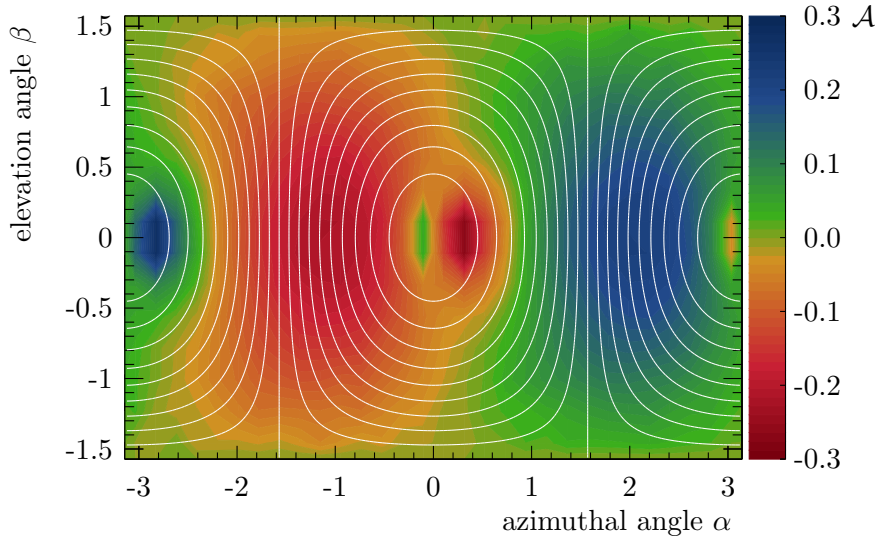

Figure 3.2.5: Asymmetry in the f_2 mass window as a function of the angles α and β. The asymmetry is shown for $W_{\gamma p} = 30\,\text{GeV}$ and $0 \leq |t| \leq 1\,\text{GeV}^2$. The white lines indicate lines of constant $\cos\theta_{k_1,p}$. Figure published by Bolz et al. [32].

To understand where the difference in the asymmetries in the proton-Jackson and the photon-Jackson frame stems from it is illustrative to consider the full

charge asymmetry in the two-dimensional angular distribution. Rather than using the polar and azimuthal angle in either the proton- or the photon-Jackson frame, the angles α and β are used here. As is discussed in Section 2.2.3, they are the natural choice when it comes to studying the charge asymmetries. In Figure 3.2.5 the asymmetry in the twodimensional α-β-plane is shown. While the overall α-β-dependence is rather non-trivial there are two important symmetries. First, by construction $\mathcal{A}(\alpha, \beta) = -\mathcal{A}(\alpha + \pi, -\beta)$. Second, the asymmetry also satisfies $\mathcal{A}(\alpha, \beta) = -\mathcal{A}(\alpha, -\beta)$, which must hold to ensure parity-invariance of $\pi^+\pi^-$ photoproduction as discussed in Section 2.2.3.

The lines in the plot represent contour levels of constant $\cos\theta_{k_1,p} = cos\beta\cos\alpha$. They connect the asymmetry as a function of α and β to the asymmetry as a function of $\cos\theta_{k_1,p}$, which is shown in Figure 3.2.2. The relation between α and β and $\cos\theta_{k_1,\gamma}$, on the other hand, is more complex. In the $\pi^+\pi^-$ center of mass system photon and proton momenta do not point into opposite directions because the $\pi^+\pi^-$ system carries a small transverse momentum k_t. As a consequence $\cos\theta_{k_1,\gamma} = -\cos(\alpha + \delta(k_t))\cos\beta$, i.e., lines of constant $\cos\theta_{k_1,\gamma}$ in Figure 3.2.5 are shifted along α by 180° plus a small k_t dependent angle. Integrating along those lines yields Figure 3.2.4.

3.2.1 Origin of the Asymmetries

From the previous discussion it became clear, that the strength of the observed charge asymmetry depends strongly on the considered invariant dipion mass window. A strong asymmetry is present in the mass region of the f_2 meson but not at the ρ^0 mass peak. To study how exactly the asymmetry depends on the dipion mass the total asymmetry that is defined in Equation (2.2.23) is shown in Figure 3.2.6 as a function of $m_{\pi^+\pi^-}$. As expected, a strong total asymmetry of up to -5% is present in the region of the f_2 resonance peaking at about 1.2 GeV. Looking at lower $\pi^+\pi^-$ masses, the asymmetry vanishes, whereas at higher masses it changes sign at about 1.35 GeV and then decreases slowly.

To understand this mass behavior and in particular the sign flip, it is illustrative to consider in more detail the origins of the charge asymmetry. As is discussed in Section 2.2.2, it is due to interferences between model contributions with $C = -1$ and $C = +1$ exchange. In order to see how the various possible interferences contribute to the total asymmetry in the full model, the asymmetry is also shown in Figure 3.2.6 with selected model contributions turned off. Most importantly, the large asymmetry in the f_2 mass region vanishes, if there are no f_2 contributions to $\pi^+\pi^-$ photoproduction. Further, it can be explicitly seen that the asymmetry arising from the interference between the f_2 and the vector mesons is negative and thus has the opposite sign than the positive asymmetry from the interference between the f_2 and the non-resonant background. For the

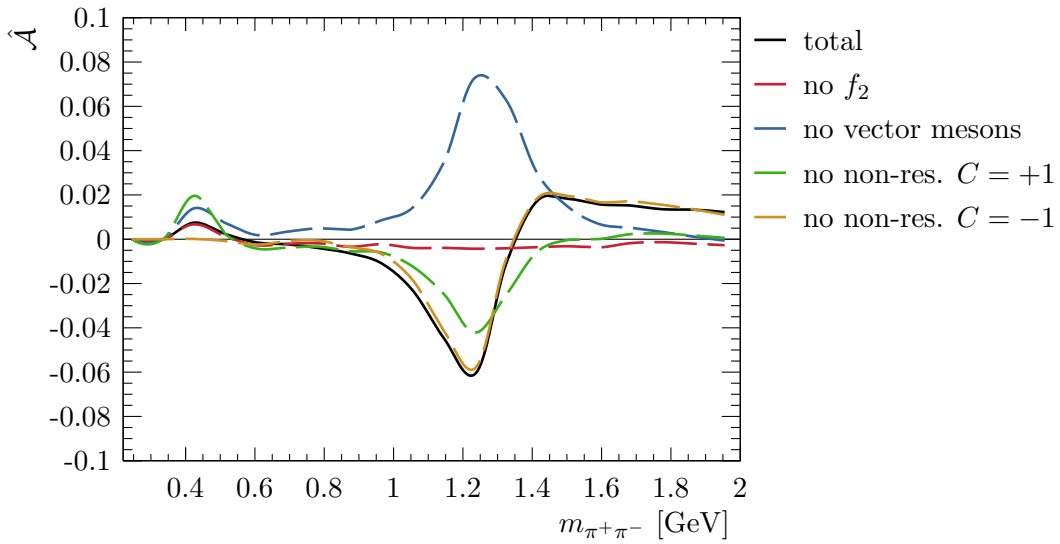

Figure 3.2.6: Total asymmetry as a function of the invariant dipion mass $m_{\pi^+\pi^-}$ shown for $W_{\gamma p} = 30\,\text{GeV}$ and $0 \leq |t| \leq 1\,\text{GeV}^2$. To illustrate which processes generate the asymmetry it is shown not only for the full model but also for the model without the f_2, vector meson, or non-resonant contributions as denoted in the legend.

latter, only the component with $C = +1$ exchange plays a rôle. Interestingly, the absolute value the asymmetry due to the non-resonant background is larger than the asymmetry due to the vector mesons, and yet the total asymmetry is negative. This is a consequence of the previously discussed skewing: Without the non-resonant contribution also the cross section in the f_2 mass region and thus the denominator in Equation (2.2.23) increases (see Figure 3.1.4). As a consequence the the asymmetry becomes smaller.

3.2.2 The Odderon Contribution

Now that the presence of asymmetries arising from the interference of the f_2 with the vector meson and non-resonant contributions is established, the role of the odderon shall be further investigated. In particular, features of the odderon in the asymmetries that could allow to discover it experimentally are discussed. Figure 3.2.7 shows the asymmetry as a function of $\cos\theta_{k_1,p}$ in the proton-Jackson frame with the Primakoff and odderon contribution being shown individually. For the given model parameters, the odderon part is slightly larger than the photon part, other than that the two contributions show a very similar behavior.

The total asymmetry as a function of the proton momentum transfer t is shown in Figure 3.2.8 (left). There the Primakoff contribution is almost constant,

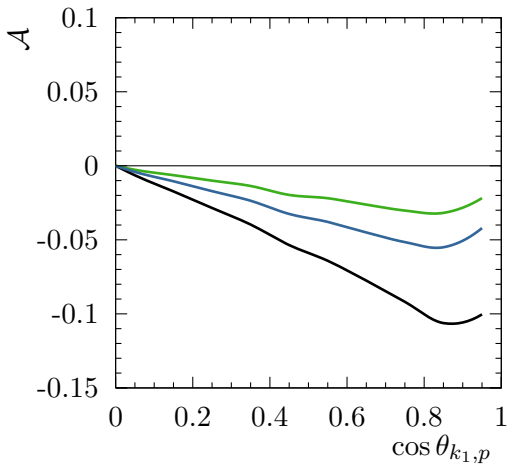

Figure 3.2.7: Asymmetry in the proton-Jackson frame as a function of $\cos\theta_{k_1,p}$ in the f_2 mass window. The asymmetry is shown for $W_{\gamma p} = 30\,\text{GeV}$ and $0 \leq |t| \leq 1\,\text{GeV}^2$. The black line corresponds to the full model, the blue and green line show the asymmetry appearing if either only odderon exchange or photon exchange contribute to f_2 resonance production. Figure published by Bolz et al. [32].

whereas. the odderon contribution becomes significantly stronger with increasing $|t|$. This is a consequence of the earlier discussed difference in t-dependence of the two respective cross sections: At small $|t|$ photon exchange dominates the f_2 production, at large $|t| \gtrsim 0.1\,\text{GeV}^2$ the odderon contribution becomes dominant. Furthermore, at large $|t|$ the vector meson production cross section drops faster than the f_2 cross section so that as a consequence the asymmetry becomes stronger. However, the precise shape of the asymmetry should not be taken too seriously because the precise t-dependence of the odderon exchange is not known and only estimated in the model. Nonetheless, since the Primakoff contribution is a well understood QED process, a strong dependence of the asymmetry on t would be a good indication for an odderon contribution.

The energy dependence of the total charge asymmetry is shown in Figure 3.2.8 (right), again including both the Primakoff and the odderon contribution. At high energies, $W_{\gamma p} > 10\,\text{GeV}$, the Primakoff part of the asymmetry stays constant with energy, while the odderon part becomes smaller with increasing $W_{\gamma p}$. The exact dependence of the odderon asymmetry is particularly sensitive to the odderon parameters. As the rise of the cross section for pomeron and odderon exchange is determined by the intercept of the corresponding Regge trajectory, the energy dependence of the asymmetry is given by them as well. While the odderon intercept is not known and thus the energy dependence of the charge asymmetry can differ from what is shown in the plot, the asymmetry has to fall with energy,

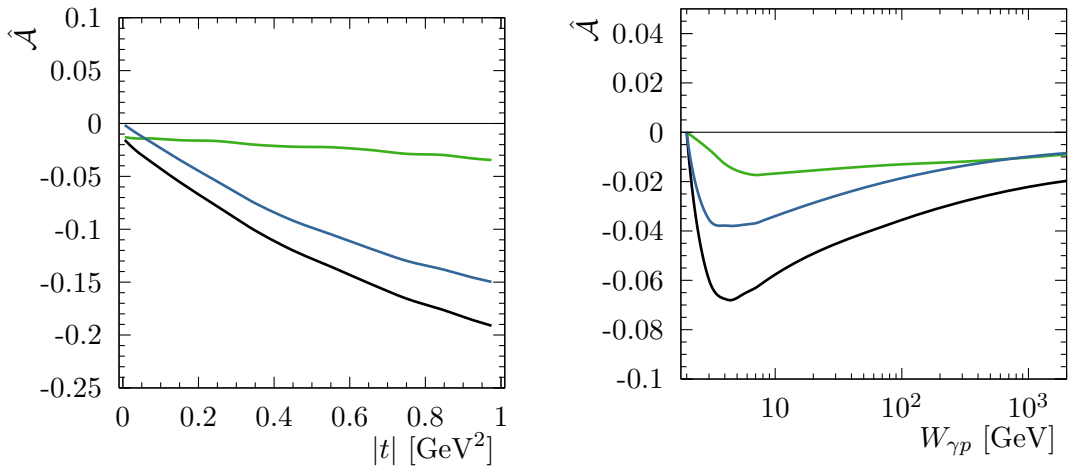

Figure 3.2.8: Total asymmetry in the proton-Jackson frame as a function of t (left) and $W_{\gamma p}$ (right) in the f_2 mass window. In the left plot the asymmetry is shown for $W_{\gamma p} = 30\,\text{GeV}$, in the right plot for $0 \leq |t| \leq 1\,\text{GeV}^2$. The black lines corresponds to the full model, the blue and green lines show the asymmetry appearing if either only odderon exchange or photon exchange contribute to f_2 resonance production. Left figure published by Bolz et al. [32].

because the odderon intercept has to be smaller than the pomeron intercept [10].

3.3 Experimental Challenges

To establish a connection to the second part of this thesis, where detector effects leading to charge asymmetries are studied at the H1 detector, issues and challenges related to detector effects are briefly discussed in this section. Ideally, one would like to process the events obtained from the event generator described in Section 2.3 through a detector simulation. Unfortunately, this was not possible within the scope of this thesis. As an alternative, possible detector effects are mimicked directly on the generator level, which allows to study their impact on the charge asymmetries in the model qualitatively.

Acceptance Effects

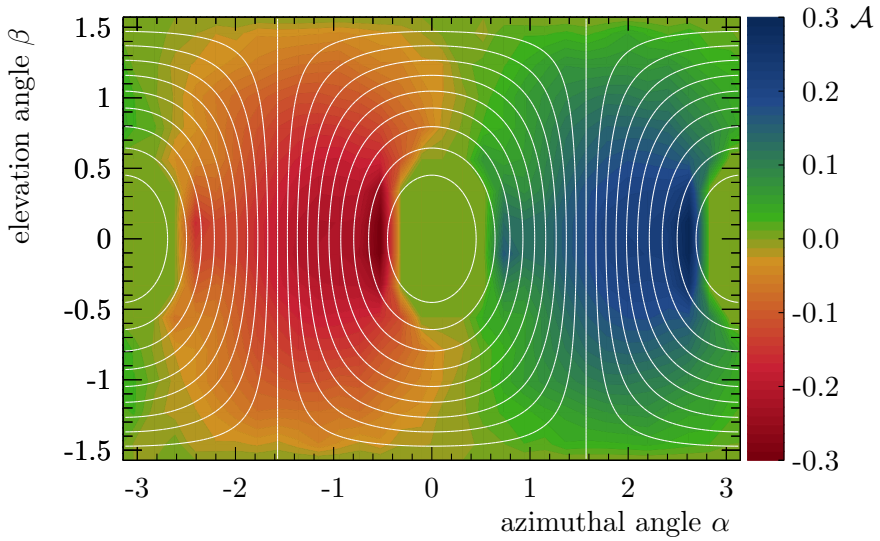

Figure 3.3.1: Asymmetry in the f_2 mass window as a function of the angles α and β. The asymmetry is shown for $W_{\gamma p} = 30\,\text{GeV}$ and $0 \leq |t| \leq 1\,\text{GeV}^2$. Additionally, in the laboratory frame both pion tracks are required to have a transverse momentum $p_t^{lab} > 200\,\text{MeV}$ and a polar angle in the range $20° < \theta^{lab} < 160°$. The white lines indicate lines of constant $\cos\theta_{k_1,p}$.

First, the consequence of a limited detector acceptance is discussed. For the H1 central tracking system the observable phase space region is given by

$$p_t^{lab} \gtrsim 0.2\,\text{GeV} \quad \text{and} \quad 20° < \theta^{lab} < 160° \tag{3.3.1}$$

where p_t^{lab} is the transverse momentum of a track in the laboratory frame and θ^{lab} its polar angle with respect to the flight direction of the incoming proton. The

lab frame is chosen such, that the incoming proton has a momentum of 920 GeV and flies anti-parallel to the incoming photon.

The charge asymmetry for events within the acceptance region is shown in the α-β plane in Figure 3.3.1. An area around $\alpha = 0, \pm\pi$ (corresponding to the direction of the incoming proton in the $\pi^+\pi^-$ center of mass frame) has become inaccessible and no asymmetry is left there compared to the original plot shown in Figure 3.2.5.

Detector Asymmetries

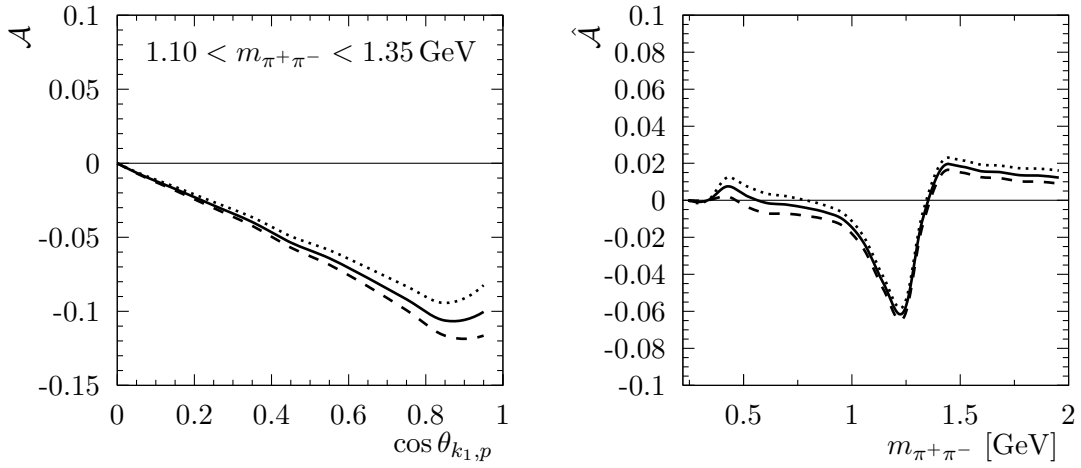

Figure 3.3.2: Asymmetry at presence of a systematic shift of the $k_{1,t}^{lab}$ spectrum as a function of $\cos\theta_{k_1,p}$ in the f_2 mass window (left) and total asymmetry in the proton-Jackson frame as a function of the $\pi^+\pi^-$ invariant mass (right). The continuous lines show the original model, the dashed ($b > 0$) and dotted ($b < 0$) lines correspond to the model with a distorted $k_{1,t}^{lab}$ spectrum as described in the text.

Secondly, consequences of detector effects resulting in charge asymmetries at the detection of particles are discussed. With respect to the H1 detector two possible scenarios are considered. First, the H1 Central Tracker (compare Chapter 4) is asymmetric in the transverse plane which can cause charge asymmetries in the tracking efficiency for low p_t^{lab}, i.e., strongly bent, tracks. In particular the Fast Track Trigger, used at H1 to trigger photoproduction events, is prone to this, as is discussed in detail in Chapter 7. Effectively, p_t^{lab} dependent trigger efficiencies can lead to distortions of the measured p_t^{lab} spectra in a data sample, which can in particular be charge asymmetric if the underlying effect is. To simulate the impact

this might have on the observation of the model asymmetries, the generated pion p_t^{lab} spectra can be artificially modified by applying p_t^{lab} and charge dependent event weights:

$$w_{\pm}(p_t^{lab}) = \frac{f_{\pm}(p_t^{lab})}{\int f_{\pm}(p_t^{lab})\,\mathrm{d}p_t^{lab}}, \tag{3.3.2}$$

with arbitrary weigh functions f_+ and f_- for positive and negative tracks, respectively.

As two possible examples $f_- := 1$ and $f_+ := a + b\,k_{1,t}^{lab}$, with $a = 1$ and $b = \pm 0.2\,\mathrm{GeV}^{-1}$ are chosen here, by which the the p_t^{lab} spectrum of the positive pion track is shifted towards higher ($b > 0$) or lower values ($b < 0$) and the spectrum of the negative track remains undisturbed. In Figure 3.3.2 the corresponding distorted asymmetry as a function of $\cos\theta_{k_1,p}$, as well as the distorted total asymmetry as a function of $m_{\pi^+\pi^-}$ are shown. Depending on the sign of b the asymmetry is in- ($b > 0$) or decreased ($b < 0$). Fortunately, the way the distortions are applied here, they shift the asymmetry in the same direction independent of the invariant mass $m_{\pi^+\pi^-}$. Assuming detector effects do not change too rapidly with the dipion mass, they are thus unlikely to fake or hide the sign change in the total asymmetry, making this sign change a very robust observable.

While not being shown explicitly here, charge dependent distortions of the pions' lab frame polar angle θ^{lab} distributions distort the charge asymmetries in a similar manner.

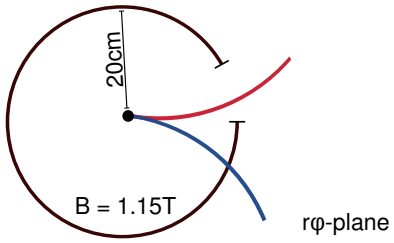

Figure 3.3.3: Illustration on how a dead detector region in φ can effect bent tracks of opposite charge differently and thus induce a charge asymmetry.

A second possibility to consider are blind detector regions along the azimuthal angle φ^{lab}. Such a situation is again present at the H1-detector, where dead wires in the outer Central Drift Chamber (compare Chapter 4 and Chapter 7) cause a significant drop in the trigger efficiency for events with tracks in the corresponding region. This is particularly interesting for low p_t^{lab} tracks that are strongly bent and thus, depending on their charge need a different angle φ^{lab} at the vertex in order to hit a dead wire as is illustrated in Figure 3.3.3.

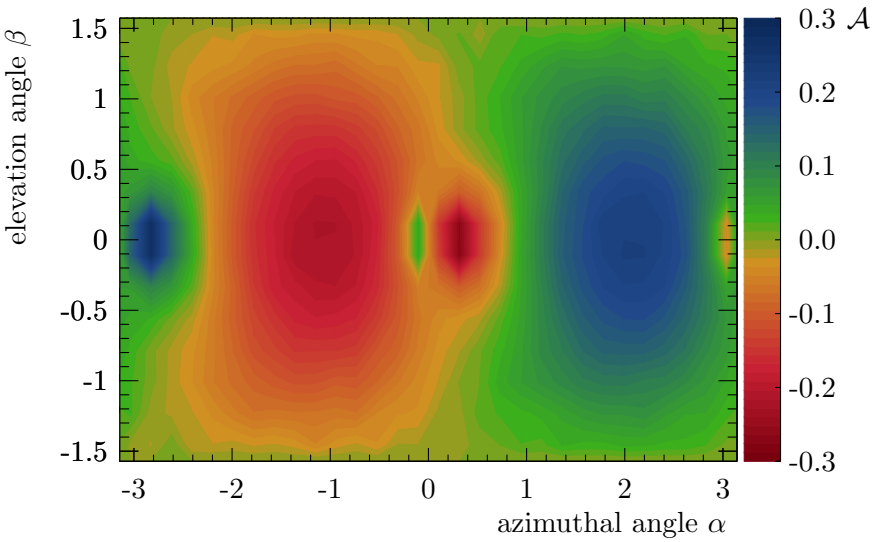

Figure 3.3.4: Distorted asymmetry in the f_2 mass window as a function of the angles α and β. The asymmetry is shown for $W_{\gamma p} = 30\,\text{GeV}$ and $0 \leq |t| \leq 1\,\text{GeV}^2$ and with charge and p_t^{lab} dependent cut on φ^{lab} as described in the text.

To study the consequences for the model asymmetry, in the event generator a cut is implemented to reject events with a track hitting a 15° wide window at a radius of 20 cm, assuming a 1.2 T magnetic field. The model asymmetry for this scenario is shown in Figure 3.3.4 as function of the angles α and β in the f_2 mass window. A comparison to the asymmetry in the undisturbed model, as shown in Figure 3.2.5, yields that such dead detector regions do not seem to influence the model asymmetries on a visible scale.

Part II

DETECTOR ASYMMETRY MEASUREMENTS AT THE H1 EXPERIMENT

4 The H1 Experiment at HERA

The analysis performed in this thesis uses data taken by the H1 experiment sited at the HERA electron proton collider. In this chapter an overview over the experimental setup is be given.

4.1 The HERA Collider at DESY

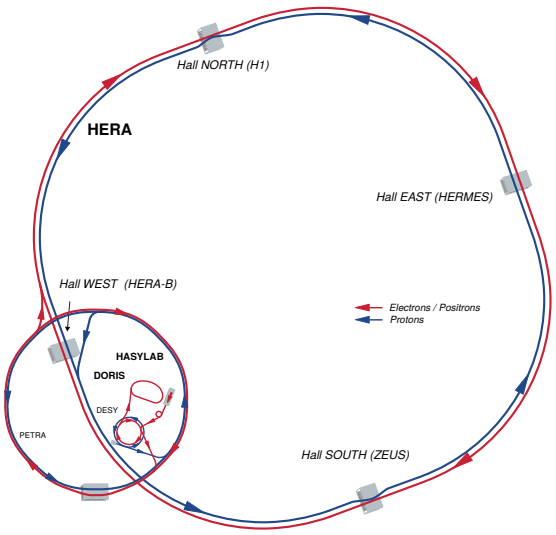

Figure 4.1.1: The HERA and pre-accelerators at DESY. Figure from DESY [82] and adapted.

The HERA (*Hadron Elektron Ring Anlage*) collider at the DESY (*Deutsches Elektronen Synchrotron*) laboratories in Hamburg combined an electron and a positron accelerator in a unique setup in one ring tunnel of 6.3 km length. In the electron machine, electrons or positrons[1] were accelerated clockwise and stored at an energy of 27.5 GeV. The protons in the other machine traveled counterclockwise at a maximum energy of 920 GeV. The two beams, having a center of mass energy of $\sqrt{s} = 318\,\text{GeV}$, were brought to collision inside the two large general purpose

[1] In the following, "electron" refers to electrons and positrons if not stated otherwise.

detectors H1 and ZEUS. In addition, HERA accommodated the spin physics experiment HERMES, where the electron beam was scattered at a hydrogen or deuterium target, and the b-physics experiment HERA-B. An overview of the DESY accelerator complex showing HERA and various preaccelerators is given in Figure 4.1.1.

Table 4.1.1: HERA II design parameters as specified in by the H1 Collaboration [83].

	electron beam	proton beam
energy [GeV]	27.5	≤ 920
number of bunches total/colliding	180/174	180/174
particles per bunch	$4.2 \cdot 10^{10}$	$10 \cdot 10^{10}$
beam current [mA]	58	140
beam size $\sigma_x \times \sigma_y$ [μ m $\times$ μ m]	118×32	118×32
bunch crossing rate [Mhz] / bunch spacing [ns]	10.4 / 96	
luminosity [$\mathrm{cm}^{-2}\, s^{-1}$]	7.36×10^{31}	
specific luminosity [$\mathrm{cm}^{-2}\, s^{-1}\mathrm{mA}^{-2}$]	1.64×10^{30}	
total integrated luminosity (2004-2007) [pb^{-1}]	612	

HERA first went into operation in 1992, received a major luminosity upgrade over the turn of the century [83, 84] and was ultimately shutdown in 2007. Table 4.1.1 lists the design parameters for the upgraded machine. The core of the HERA physics program was the study of the internal structure of the proton and the dynamics of the partons comprising it. Beyond that, a wide range of other phenomena were investigated as well. Among those are the electroweak force, for which H1 and ZEUS could find direct evidence for the unification of the electromagnetic and weak forces, QCD, for which the scale dependence of the coupling constant could be measured over a wide range of energies, or, in the context of the thesis, diffractive scattering processes and the hadronic structure of the photon. For an overview of H1 and ZEUS measurements see [85].

4.2 The H1 Detector

A schematic view of the H1 detector as it was designed for the HERA II phase is given in Figure 4.2.1. The detector is asymmetric with respect to the nominal *interaction point* (IP), because incoming electrons and proton have different center

Table 4.2.1: H1 subdetector systems as indicated in Figure 4.2.1.

	detector component	abbreviation
1	nominal interaction point	IP
	Tracking Detectors	
2	Central Silicon Tracker	CST
3	Backward Silicon Tracker	BST
4	Forward Silicon Tracker	FST
5	Central Inner Proportional Chamber	CIP
	and Central Inner z-Drift Chamber	CIZ
6	Central Outer Proportional Chamber	COP
	and Central Outer z-Drift Chamber	COZ
7	Inner Central Jet Chamber	CJC1
8	Outer Central Jet Chamber	CJC2
9	Forward Tracking Detectors	FTD
10	Backward Proportional Chamber	PBC
	Calorimetry	
11	Liquid Argon Cryostat	
12	Liquid Argon Electromagnetic Calorimeter	LAr elm.
13	Liquid Argon Hadronic Calorimeter	LAr hadr.
14	Liquid Argon Cryogenic System	
15	Electromagnetic Spaghetti Calorimeter	SpaCal elm.
16	Hadronic Spaghetti Calorimeter	SpaCal hadr.
17	Plug Calorimeter	Plug
18	Toroid and Superconducting Solenoid Magnet	
19	Superconducting Focusing Magnets	GO/GG
	Muon Detectors	
20	Instrumented Iron: Central Muon and Tail Catcher	CMD/TC
21	Forward Muon Detector	FMD
22	Veto wall (time of flight system)	ToF
23	Concrete Shielding	

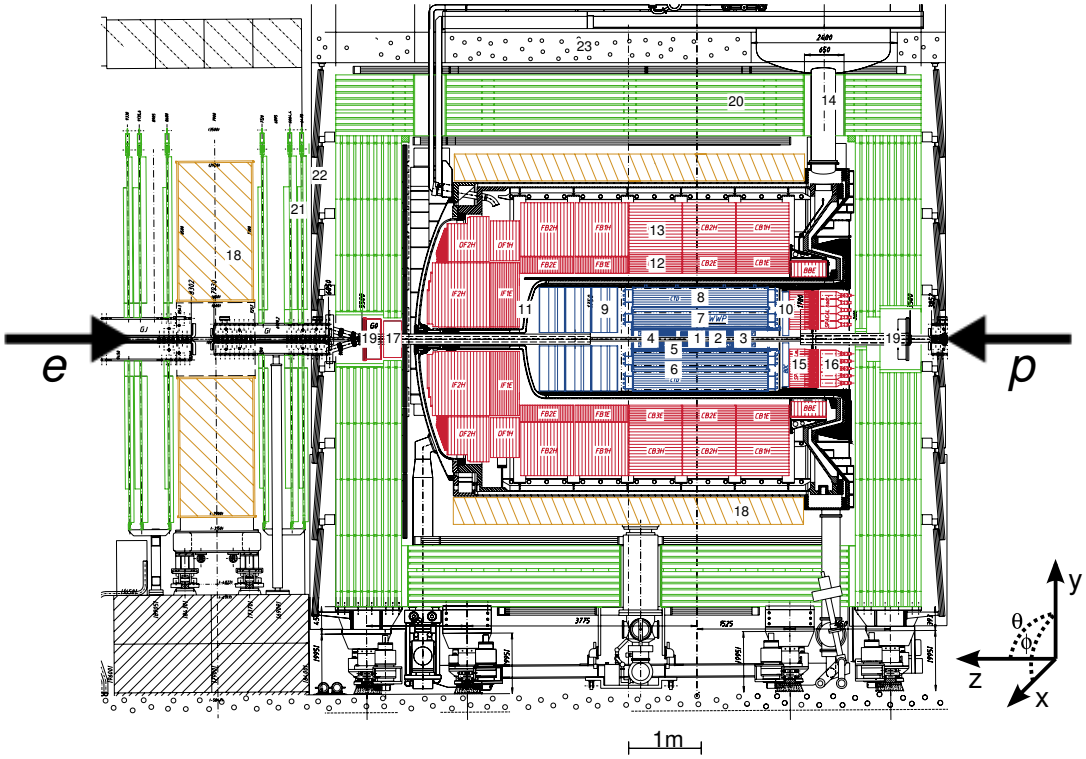

Figure 4.2.1: Schematic cut through of the H1 detector as operational at HERA II. For a list of the various subdetectors see Table 4.2.1. The coordinate system used in the following is shown as well, but for clarity is moved away from the origin at 1. Figure provided by collaboration and adapted.

of mass energies, which results in a boost of the particles created in a collision in the proton flight direction.

The H1 coordinate system, see Figure 4.2.1, has its origin at the IP. The z-axis is given by the flight direction of the protons (*forward direction*), the x and y-axis point towards the center of the HERA ring and upwards, respectively. They span the *transverse plane*. In polar coordinates, the *polar angle* θ is defined with respect to the z-axis. The *azimuthal angle* φ in the transverse plane is defined such that the x-axis corresponds to $\varphi = 0$ and that it is in the range $-\pi < \varphi < \pi$.

Like most collider experiments, H1 can be subdivided into sections for tracking, calorimetry, and muon detection, which consist of various subdetectors, each, as listed in Table 4.2.1. The tracking section is located closest to the IP to measure tracks of charged particles. Directly around the beam pipe, high resolution silicon detectors aim to resolve secondary vertices of long living particles. At larger radii, fast multiwire proportional chambers are used for triggering purposes and drift chambers to reconstruct trajectories of charged particles. Surrounding the

tracking section, in the calorimeter systems particle energies are measured. In the central and forward direction a liquid argon sampling calorimeter is used with lead (electromagnetic part) and iron (hadronic part) absorber layers. In the backward region, the *sphaghetti calorimeter*, a lead-scintillator-fibre detector, is employed mainly to measure the scattered electron. The calorimeter is surrounded by a superconducting solenoid providing a magnetic field of 1.15 T, in which charged particles are bent according to their transverse momentum. At the very edge of the detector, muons that penetrate the calorimeter are measured in designated muon detectors. Detailed descriptions of all H1 subdetectors are provided by the H1 Collaboration [86, 87]; in the following only those systems relevant for this thesis are described.

4.2.1 H1 Central Tracking System

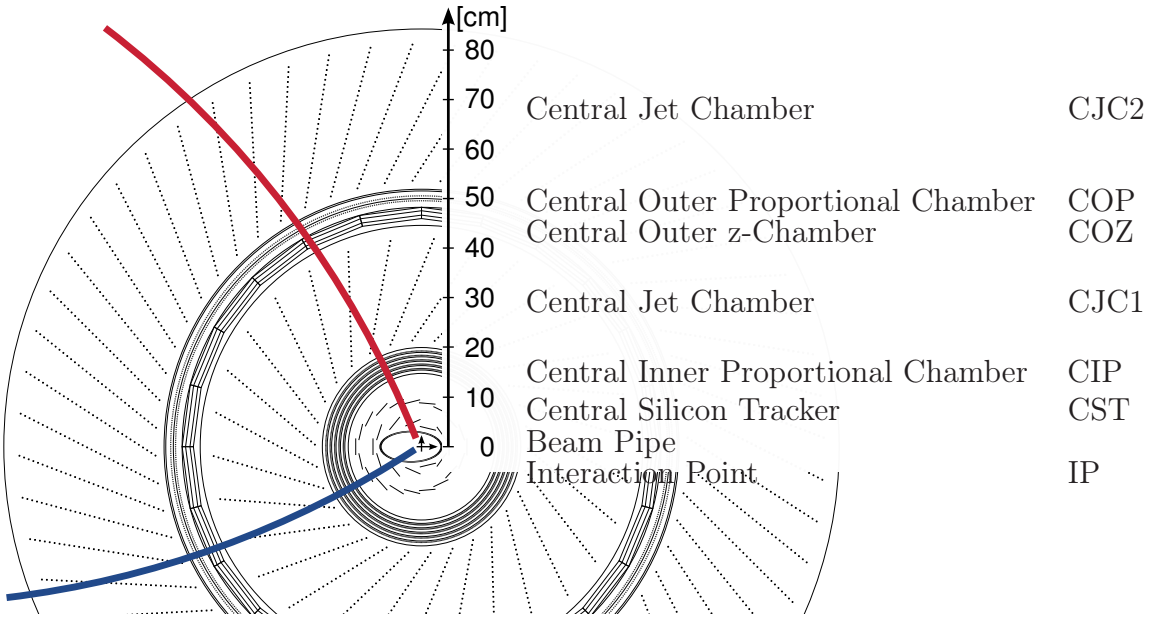

Figure 4.2.2: Radial view of the H1 Central Tracking Detector as operational during HERA II. The colored lines indicate how positive tracks(blue) and negative tracks(red) are bent in the magnetic field.

In the H1 tracking section three regions are distinguished: the *Forward Tracking Detector* (FTD) covers tracks with polar angles $7° < \theta < 20°$, the *Central Tracking Detector* (CTD) $20° < \theta < 160°$, and the *Backward Proportional Chamber* (BPC) $160° < \theta < 175°$. For this thesis only the CTD is of relevance and important components are introduced. A schematic cut through the CTD in the transverse plane is shown in Figure 4.2.2.

At the center of the CTD, closest to the beam pipe, the *Central Silicon Tracker* (CST) is used to measure the primary vertices of scattering events and the decay vertices of long-lived particles with a high spatial resolution. It is surrounded by the fast *Central Inner Proportional Chamber* (CIP) used for trigger and timing purposes. Following the CIP at even larger radii the *Central Jet Chambers* (CJC) 1 and 2, two concentric drift chambers with wires strung parallel to the z-axis, are used to precisely measure tracks in the transverse plane. The z-positions of CJC hits can be determined by charge division along the wires. For a more precise measurement of the z-position of a track the *Outer z-Drift Chamber* (COZ), which has its wires strung perpendicular to the beam axis, is installed in between the CJC1 and CJC2. Finally, a second proportional chamber, the *Central Outer Proportional Chamber* (COP), is installed between the COZ and the outer CJC. The jet chambers and the CIP are most relevant for this thesis and explained in more detail below.

In the H1 magnetic field charged particles are deflected in the transverse plane but remain undisturbed along the z-axis. Their tracks thus are described by helices which are characterized by a set of 5 parameters. Those are in the transverse plane the curvature κ, the distance of closest approach to the IP d_{ca} and the azimuthal angle φ_0 at the point closest to the IP, and in the rz-plane the z-position of the point of closes approach z_0 and the polar angle θ. The curvature κ is the inverse of the radius R of a circular track in the transverse plane:

$$\kappa = \frac{1}{R}. \tag{4.2.1}$$

R in turn is given by the transverse momentum p_t of a particle, its charge z in units of the elementary charge e, and the magnetic field B:

$$p_t = p \cos\theta = zeRB. \tag{4.2.2}$$

For the field configuration present at H1 this simplifies to

$$p_t[\,\mathrm{GeV}] = 0.345 \cdot R[\,\mathrm{m}]. \tag{4.2.3}$$

So in particular, measuring the curvature of a track allows to also measure its transverse momentum.

The Central Jet Chamber (CJC)

The *Central Jet Chamber* [88] consists of two large, concentric drift chambers, the inner CJC1 and the outer CJC2, with a geometry as specified in Table 4.2.2. They are filled with an Argon-Ethane based gas mixture. In the transverse plane the CJC1 is divided into 30 and the CJC2 into 60 drift cells as illustrated in Figure 4.2.2. Cells are defined by cathode wire planes strung parallel to the z-axis

Table 4.2.2: CJC Parameters as listed by Bürger et al. [88].

	CJC1	CJC 2
number of cells	30	60
number of sense wires/cell	24	32
inner radius [cm]	20.3	53.0
outer radius [cm]	42.6	84.4
active radius [cm]	22.5	29.6
z-min [cm]	-112.5	
z-max [cm]	$+107.5$	

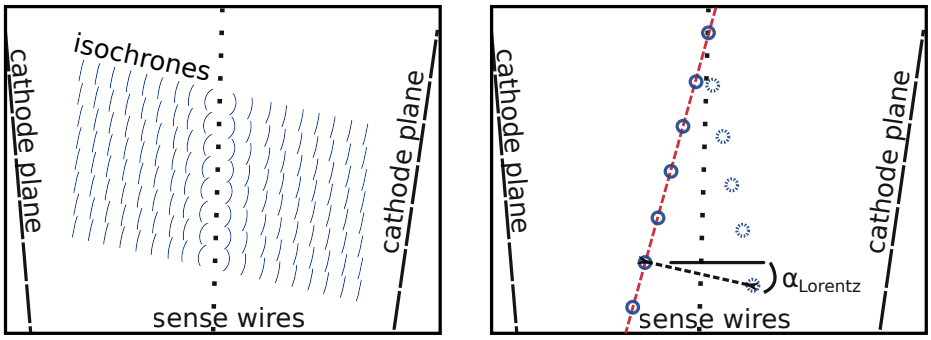

Figure 4.2.3: Schematic of a CJC drift cell consisting of cathode planes and anode wires. Potential wires are not shown. Left: Isochrones of the electric and magnetic field. Right: The charge carriers ionized by a charged track drift to the anode wires in the direction of the marked Lorentz angle and cannot be distinguished from mirror charges.

and contain 24 (CJC1) and 32 (CJC2) anode wires along a central plane. The wire planes are titled by 30° with respect to the radial direction. The application of a high voltage creates an electrostatic field, which is further shaped by several potential wires per cell. In this field charge carriers that are ionized when a charged particle traverses the gas volume drift to the anode and cathode wires. The field is shaped such, that isochrones, i.e., lines of constant field strength in the superimposed electric and magnetic field, form circles in the near field around the anode wires and charge carriers always drift to the closest wire. The Lorentz angle, i.e., the angle between the direction of the electric field and the drift direction of the charge carriers in the presence of an electric and a magnetic field, is approximately 25°. Considering the tilt of the drift cells, charge carriers ionized by a straight, high p_t ("stiff") track drift almost perpendicular to the track as illustrated in Figure 4.2.3.

The anode wires are used as *sens wires* and the signals induced by the charge

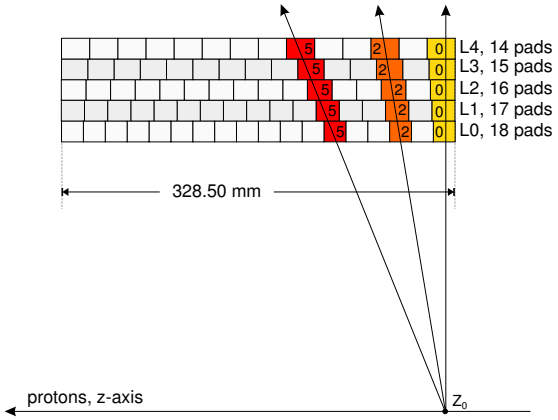

Figure 4.2.4: On the projective geometry of the CIP. Tracks originating from the same position along the z-axis create the same hit pattern, which obtains a constant offset in all layers depending on the track polar angle θ. Figure from Urban [89] and adapted.

carriers are read out. The knowledge of the field configuration allows to determine the position of a hit in the $r\varphi$-plane by measuring the drift times of the ionized charge carriers. As the trajectory of a charged particle in the transverse plane is circular, tracks can be constructed by combining several hits all lying on a circle. The left right ambiguity inherent to all drift chambers can be resolved by combining hits from two neighboring drift cells. The drift chambers are constructed such, that a stiff track always crosses at least one cell boundary. In addition a stiff track also crosses at least one sense wire plane. From this crossing point, where the drift time is minimal, the timing of a track can be determined with an accuracy $\sim 2\,\text{ns}$, which allows to distinguish tracks originating from different bunch crossings.

By measuring the total collected charge of a hit Q by reading out both ends of the signal wires, the z-position of a hit can be determined via charge division: The further a hit is from one end of a sense wire, the weaker the signal that is read out at that end. During the reconstruction of a track, the z-information obtained by this method is combined with the measurements from the COZ for an improved z-resolution.

The Central Inner Proportional Chamber (CIP)

The *Central Inner Proportional Chamber* (CIP) [90] is a five layer multiwire proportional chamber starting at a radial position of $r = 15.7\,\text{cm}$ and covering along the z-axis a range from $z = -112.7\,\text{cm}$ to $z = +104.3\,\text{cm}$. Its main purpose is to provide fast tracking information at the first H1 trigger level (see Section 4.2.3), i.e., in particular to reconstruct the z-position (z-vertex) of an interaction. The

CIP is segmented into 16 regions in the transverse plane. Along the z-axis, a total of 9600 readout pads are arranged in a projective geometry. As illustrated in Figure 4.2.4, for this geometry the origin of a track on the z-axis can be directly read off the pad hit pattern in the 5 CIP layers, independent of the track's polar angle.

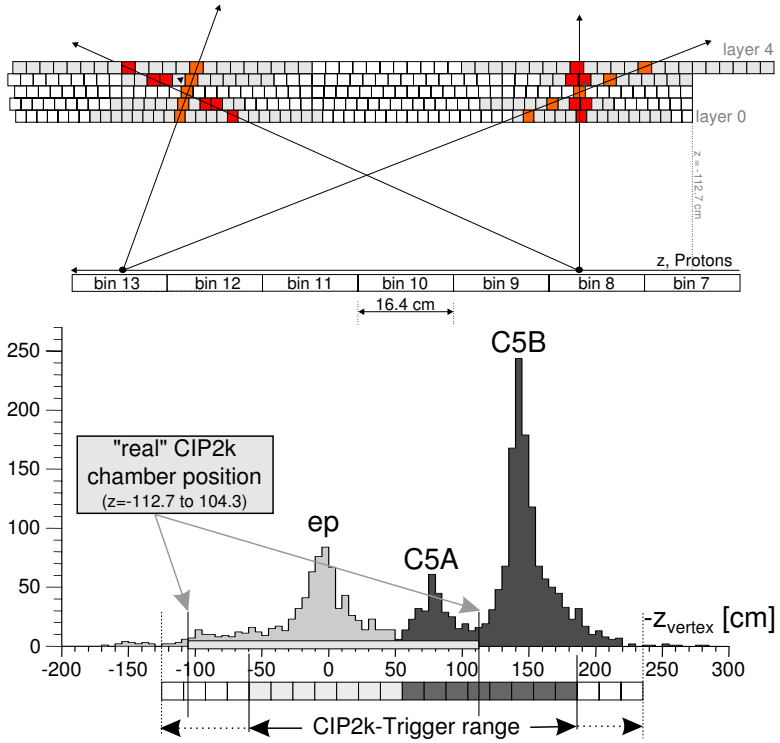

Figure 4.2.5: Top: Construction of the CIP vertex histogram for the CIP2000 trigger. Bottom: Example for such a histogram where the peak from *ep* collisions (light gray) is superimposed by backgrounds from collisions of the incoming proton beam with the collimators C5A and C5B (dark gray). The histogram is only evaluated at the marked CIP2000 trigger range, where light gray bins are considered as signal and dark gray bins as background. Figure from Urban [89] and adapted.

For the level 1 *CIP2000* trigger the z-positions along the beam axis of all tracks in an event are filled in a z-vertex histogram, as illustrated in Figure 4.2.5. From the histogram two trigger elements are constructed: the *CIP Multiplicity*, corresponding to the total number of entries in the histogram, i.e., the total number of tracks in the event, and the *CIP Significance*, corresponding to the fraction of central entries (signal) to backward entries (background), with the central and backward region being defined in Figure 4.2.5. With a very good timing resolution of $\sigma = 7.1\,\text{ns}$, which is well below the 96 ns bunch crossing

spacing, the CIP also provides timing information that can be used to determine the correct bunch crossing of an event.

4.2.2 H1 Calorimetry Systems

The Liquid Argon Calorimeter (LAr)

In the forward and central region ($4^\circ < \theta < 153^\circ$) the H1 tracking detectors are surrounded by a large *Liquid Argon Calorimeter* (LAr) [91] to measure the energies of electrons, photons and hadrons. In alternating layers of absorber material and sensitive liquid Argon, particles penetrating the calorimeter decay into particle showers and the energy loss via ionization of the low energetic shower particles is sampled. In the inner (electromagnetic) part of the calorimeter lead, and in the outer (hadronic) part steel is used as the absorber material. The LAr is highly segmented into cells, which allows in particular to assign energy clusters to particle tracks.

The Spaghetti Calorimeter (SpaCal)

In the backward region the LAr is complemented by the *Spaghetti Calorimeter* (SpaCal), a lead-scintillating fiber detector read out by photomultiplier tubes (PMTs). The main purpose of the SpaCal is to detect the scattered electron for polar angles in the range $153^\circ \lesssim \theta \lesssim 177.5^\circ$. The SpaCal is fast enough to be used as a level 1 electron trigger.

The Plug Calorimeter

Sitting directly around the beam pipe and far from the IP at $z = 4.9\,\mathrm{m}$, the *Plug Calorimeter* (Plug) covers an angular range of $1.2^\circ < \theta < 3.2^\circ$ and is in particular used to measure the scattered proton. It consists of a lead absorber followed by scintillating layers read out by PMTs. The energy deposited in the Plug can be used to distinguish proton elastic from proton dissociative events, for which on average more energy is deposited.

4.2.3 H1 Trigger System

The bunch crossing rate at HERA is 10.4 MHz. The H1 data acquisition system however only allows to read out data at 50 Hz. The rate at which data is stored permanently on tape varies between approximately $10 - 20\,\mathrm{Hz}$. It is thus necessary to reduce the data by a factor about one million. This is achieved by a four level filtering system: the H1 *Central Trigger* (CT).

Level 1

In the first trigger stage (L1, [92]) event information from various H1 sub-detectors is processed by custom-made hardware. The event is scanned for interesting physics, signaled for example by large energy deposits in the calorimeter, muons in the muon system or tracks in the central tracker. The information is encoded in 256 *Trigger Elements* (TE) that are logically combined in the *Central Trigger Logic* (CTL) to form 128 subtriggers (named `s0` ... `s127`). An event is triggered if at least one of the subtriggers fires. However, some subtriggers fire at too high a rate compared to the significance of the corresponding type of event. Those triggers are artificially prescaled [93], i.e., a trigger with prescale n is only considered every n^{th} time it fires. A subtrigger that has the trigger condition fulfilled is then called a *raw subtrigger* and only becomes an *actual subtrigger* if also the prescale condition is fulfilled.

The L1 stage is operated dead-time free, i.e., data taking continues while the trigger decision is conceived. This takes 2.3 μs corresponding to 24 bunch-crossings during which the data is temporarily stored in pipelines. To be able to read out the correct event in case a trigger decision is reached, detector components with a good timing resolution like the SpaCal or the CIP are used to generate a L1 time reference t_0 that can be used to identify the corresponding bunch-crossing.

Level 2

A positive L1 decision (*L1 Keep*) triggers the second trigger stage (L2, [94]). Within a time window of 20 μs measurements are repeated with a higher granularity to verify the L1 trigger decision. While this is ongoing, data taking is interrupted causing dead-time. Information from various sub-detectors is combined to form 96 trigger elements. If a positive trigger decision is reached a full detector read-out is initiated. The data rate is reduced to about $100 - 200$ Hz by the L2 trigger.

Level 3

The read out of the detector takes up to more than 2 ms depending on the size of the event ($\sim$ 1.3 ms on average). In order to reduce dead time, data that is available earlier, e.g. FTT information, is used by the third trigger stage (L3 [95]) to validate the L2 decision. If the validation fails, the read-out can be halted after approximately 100 μs. When this happens, or as soon as the read out is completed the pipelines are cleared and data taking is continued.

Level 4

The third trigger level provides data at a rate of 50 Hz at which it can be stored temporarily in a buffer. This allows the fourth trigger stage (L4) to work independently from and asynchronously to the detector bound first three trigger levels. L4 is a purely software based trigger running on a computer farm. The H1 reconstruction program (H1Rec) is used to fully assemble the collected data and build the event. *Finders*, special algorithms, are employed to search for certain event characteristics and to classify events into interesting and uninteresting ones. Uninteresting events, e.g. background events from beam-gas or beam-wall interactions are discarded. Interesting ones are selected and have their full detector data stored permanently on *Production Output Tapes* (POT). For easier access, reconstructed physics objects like tracks, clusters, etc. are additionally stored on *Data Summary Tapes* (DST). To be analyzed by the ROOT [96] based H1oo analysis software this data is also converted to the C++ [97] object oriented *Object Data Storage* (ODS). The event rate after the L4 is at about 10 Hz meaning that the full trigger system reduces the bunch crossing rate by six orders of magnitude.

4.3 The Fast Track Trigger

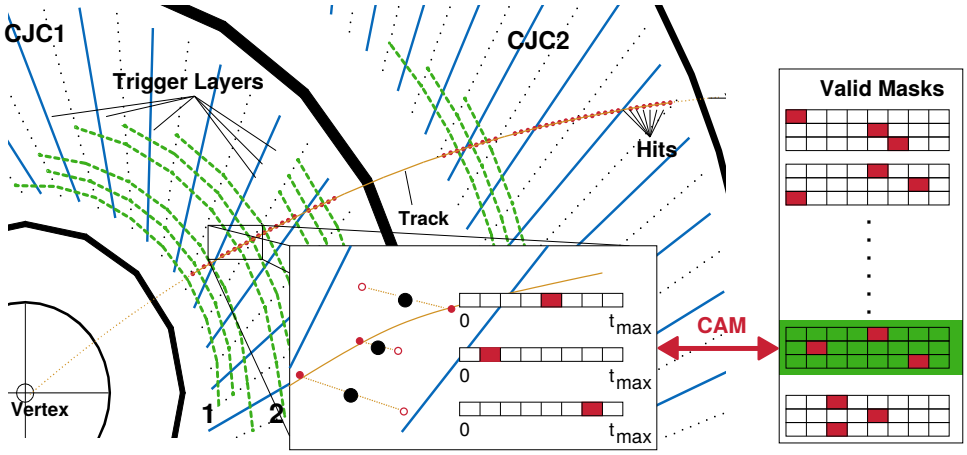

Figure 4.3.1: Working principle of the FTT. During the first trigger stage hit patterns from the 4 trigger groups are compared to predefined patterns in the Content Addressable Memory (CAM). This allows to measure curvature and angular position of the track segments. Figure from Berger [98] and adapted.

One key component of the H1 trigger system is the Fast Track Trigger [99] based on information from the two CJCs. Already on the first trigger level it can count

the number of tracks with transverse momenta down to 100 MeV. This allows the FTT to trigger events with very low Q^2 that do not leave large signals in the calorimetry system. In particular, photoproduction of light vector mesons falls into that category.

For the measurement of charge asymmetries in $\pi^+\pi^-$ photoproduction the trigger, i.e., in particular the FTT, is an important source for systematic effects. In the second part of this thesis these effects are studied. In the following the working principle of the FTT is briefly discussed. A detailed description of the FTT is given for example by Berger [98] and Baird et al. [99].

4.3.1 Working Principle

The FTT is based on information from the Central Jet Chambers. It processes information from three trigger groups in the inner and a fourth group in the outer CJC, consisting each of three wires per cell. A schematic view of this setup is shown in Figure 4.3.1.

The core task of the FTT is to measure track candidates. For this, the analog signals from the wires in the trigger layers are read out and processed by the FTTs *Front End Modules* (FEM). There they are digitized and an analysis of the sampled charges is used to distinguish hits from noise. The resulting hits are filled into shift registers with a time resolution of 20 MHz. If all three wires in a cell have a hit, the hit pattern in the shift register is compared to a set of predefined masks. These masks have been generated in advance by simulating possible tracks through the CJC and are stored on *Content Addressable Memory* (CAM) to allow for fast access. If a mask matching the hit pattern can be found, the track segment parameters can be taken from it. Track segments are parametrized by the curvature $\kappa \propto 1/p_t$ and the azimuthal angle φ of the CJC cell they are measured in. There are 16 possible κ values corresponding to 8 momentum thresholds as listed in Table 4.3.1 and the charge of the track. The granularity in φ is given by the size of the CJC1 cells, i.e., there are 30 possible values.

For each identified track segment the κ and φ value are stored in a histogram. These histograms are then used by the FTT's *L1 Linker* to identify track candidates. For identification the histograms are first smeared such that each φ column is doubled, resulting in a total number of 60 possible φ-values. Bins containing a track segment get a weight of 3 and their neighboring bins along κ get a weight of 1. A *Hough-transform* is performed to map the φ values of all trigger groups onto the φ value of the third group $\tilde{\varphi} \equiv \varphi(r_3 = 22\,\text{cm})$ as illustrated in Figure 4.3.2. The histograms from all layers are then added. Among those bins that exceed a threshold weight of 4, i.e., there are compatible track segments in at least two trigger layers, local maxima are searched. These give the track candidates. To

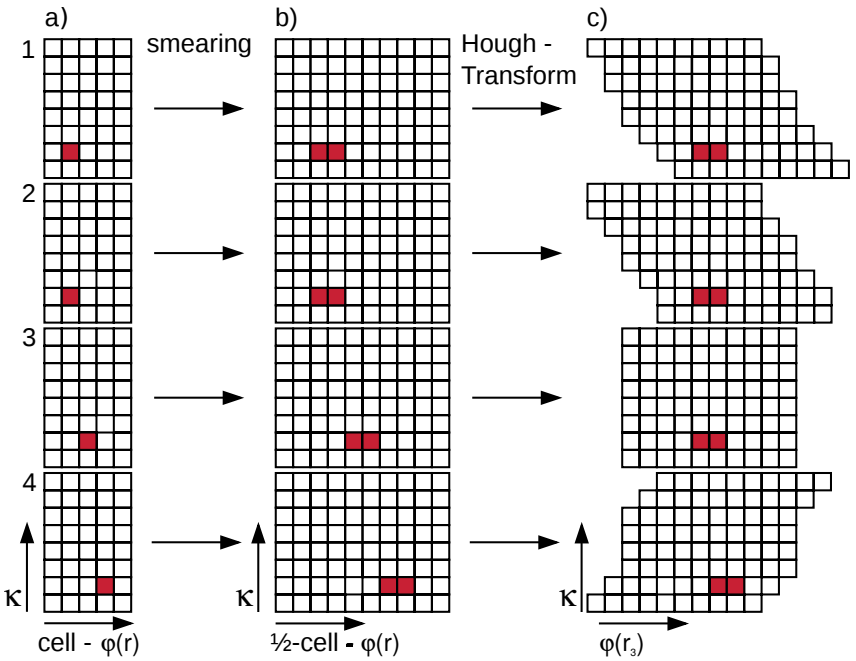

Figure 4.3.2: Illustration of the *Hough-transform* performed by the L1 Linker. a) Track segment parameters for the 4 trigger groups in a schematic κ-φ-plane, where φ corresponds to the position of the CJC cell the track segment lies in. b) Histograms are shown after smearing, i.e., duplicating each φ column. In a Hough-transform, which also takes into account the cell tilt, the track parameters are shifted so that in each histogram φ corresponds to the angle $\tilde{\varphi} \equiv \varphi(r_3)$ measured in the third trigger group. c) Track segments with compatible parameters sit in the same place in the transformed κ-$\tilde{\varphi}$-plane. Figure from Berger [98].

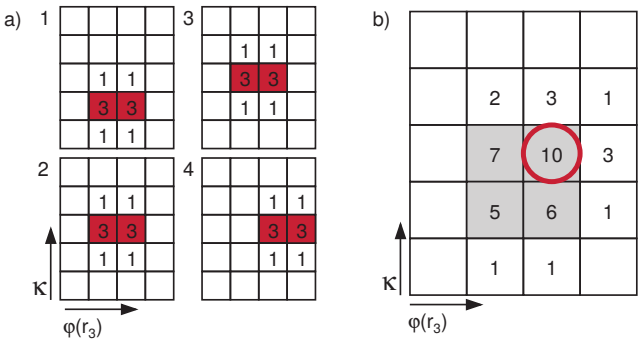

Figure 4.3.3: Working principle of the L1 Linker algorithm. a) Track segment parameters in the four trigger layers after the performing the Hough-transform. The numbers represent weights given to the bins. b) The histograms are added for the linking. Bins that exceed the linking threshold of 4 are shaded. A track candidate is given by the bin with the maximum weight, marked by a red circle. Figure from Berger [98].

Table 4.3.1: FTT L1 momentum thresholds. The number of tracks exceeding a selection of these thresholds is encoded in L1 trigger elements. As only a limited number of bits is available for each element, the highest bit state, i.e., 7 (3), indicates 7 (3) or more tracks.

κ bins	p_t [GeV]	$1/p_t$[GeV^{-1}]	trigger element	n_{max}
0, 15	0.100	10.00	`FTT_mul_Ta`	7
1, 14	0.125	8.00	–	3
2, 13	0.160	6.25	`FTT_mul_Tb`	3
3, 12	0.250	4.00	–	3
4, 11	0.400	2.50	`FTT_mul_Tc`	3
5, 10	0.600	1.66	–	3
6, 9	0.900	1.11	`FTT_mul_Td`	3
7, 8	1.800	0.55	`FTT_mul_Te`	3

avoid double counting of tracks, bins adjacent to a local maximum are vetoed. See also Figure 4.3.3.

FTT Level 1

Track reconstruction in the FTT happens within the 2.3 μs time window of the H1 L1 trigger. Most time is needed waiting for distant charges with long drift times, while the actual track finding algorithm is much faster. From the track information 16 L1 trigger bits are generated. Those provide information on track multiplicities for various momentum thresholds as defined in Table 4.3.1, on the summed charge of all tracks (provided by the sign of κ) and on the topological structure of the event. To analyze the event topology the r-φ-plane is divided into 10 sectors and the trigger bits indicate the configuration of sectors that observed a track.

FTT Level 2

The much larger time window for the L2 trigger allows to reconstruct tracks with a finer histogram binning of 40×640 bins in κ-$\tilde{\varphi}$-plane. In addition, the z-position of a track is determined by charge division. This allows to obtain the full, 3D track information for up to 48 tracks. The resolution obtained for the track parameters is comparable to that obtained in the offline reconstruction. In particular, the 3D tracks can be used to calculate more complex event variables, such as invariant masses, to be used for the trigger decision.

FTT Level 3

In the third trigger level the high resolution L2 FTT tracks are combined with information from other sub-detectors to perform a partial event reconstruction. Special finders search for well known physics processes that can have final states with more than two tracks, i.e., $D^* \to K\pi\pi$

4.3.2 Track Assignment

To be able to measure the single track FTT efficiency, i.e., the efficiency with which the FTT observes a real track, it is necessary to associate the tracks measured by the FTT to the fully reconstructed tracks. For this a track assignment algorithm has been implemented and is described here. First, it should be noted, that it is not sufficient to simply count tracks because the FTT can see ghost tracks that are not really there (see also Chapter 7). To avoid assigning such an FTT ghost to a reconstructed track only tracks that are compatible with each other should be considered for an assignment.

There are several possibilities to quantify a compatible tracks; here, a metric is defined as follows. For the reconstructed tracks the track parameters used by the FTT, i.e., the inverse transverse momentum $1/p_t$ and the geometrical angular position $\tilde{\varphi}$ of the track at a radius of $r = 22\,\text{cm}$, are calculated.[2] In the $1/p_t$-$\tilde{\varphi}$ parameter space the "distance" between a reconstructed and an FTT track can then be defined via

$$\Delta_{rec,\ FTT} = \sqrt{\left(\frac{1/p_{t_{rec}} - 1/p_{t_{FTT}}}{\sigma_{1/p_t}}\right)^2 + \left(\frac{\tilde{\varphi}_{rec} - \tilde{\varphi}_{FTT}}{\sigma_{\tilde{\varphi}}}\right)^2}, \tag{4.3.1}$$

where $\sigma_{\tilde{\varphi}}$ and σ_{1/p_t} are the resolution of the FTT in $\tilde{\varphi}$ and $1/p_t$, respectively. However, the resolution in $1/p_t$ strongly depends on p_t, which is reflected roughly in the FTT p_t threshold separation as listed in Table 4.3.1. These thresholds define a binning in $1/p_t$

$$\begin{aligned}[-10.0,\ -8.00,\ -6.00,\ -4.00,\ -2.50,\ -1.66,\ -1.10,\ -0.55,\ \ 0.0,\\ 0.55,\ \ 1.10,\ \ 1.66,\ \ 2.50,\ \ 4.00,\ \ 6.00,\ \ 8.00,\ 10.0]\end{aligned}, \tag{4.3.2}$$

where the inverse transverse momenta of the FTT tracks are always set to the central value. To account for the discretization inf the FTT system, also for the

[2] It does not make sense to do it the other way around and calculate p_t and φ at the vertex for the FTT tracks because of the significantly worse resolution of the L1 FTT parameters compared to the full reconstruction.

reconstructed tracks binned $1/p_t$ values are calculated. Using in addition the 60 equidistant $\tilde{\varphi}$ bins a "bin distance" can be defined:

$$\Delta^{bin}_{rec,\ FTT} = \sqrt{\left(\frac{i_{1/p_t,rec} - i_{1/p_t,FTT}}{\sigma_{i,1/p_t}}\right)^2 + \left(\frac{i_{\tilde{\varphi},rec} - i_{\tilde{\varphi},FTT}}{\sigma_{i,\tilde{\varphi}}}\right)^2}. \tag{4.3.3}$$

Here, i_{1/p_t} and $i_{\tilde{\varphi}}$ are the bin numbers in $1/p_t$ and $\tilde{\varphi}$ of the reconstructed and the FTT track and $\sigma_{i,\tilde{\varphi}} \simeq 0.6$ and $\sigma_{i,1/p_t} \simeq 0.8$ are the bin resolutions. They are determined from the widths of the distributions of the bin differences of assigned tracks; see Figure 4.3.4.

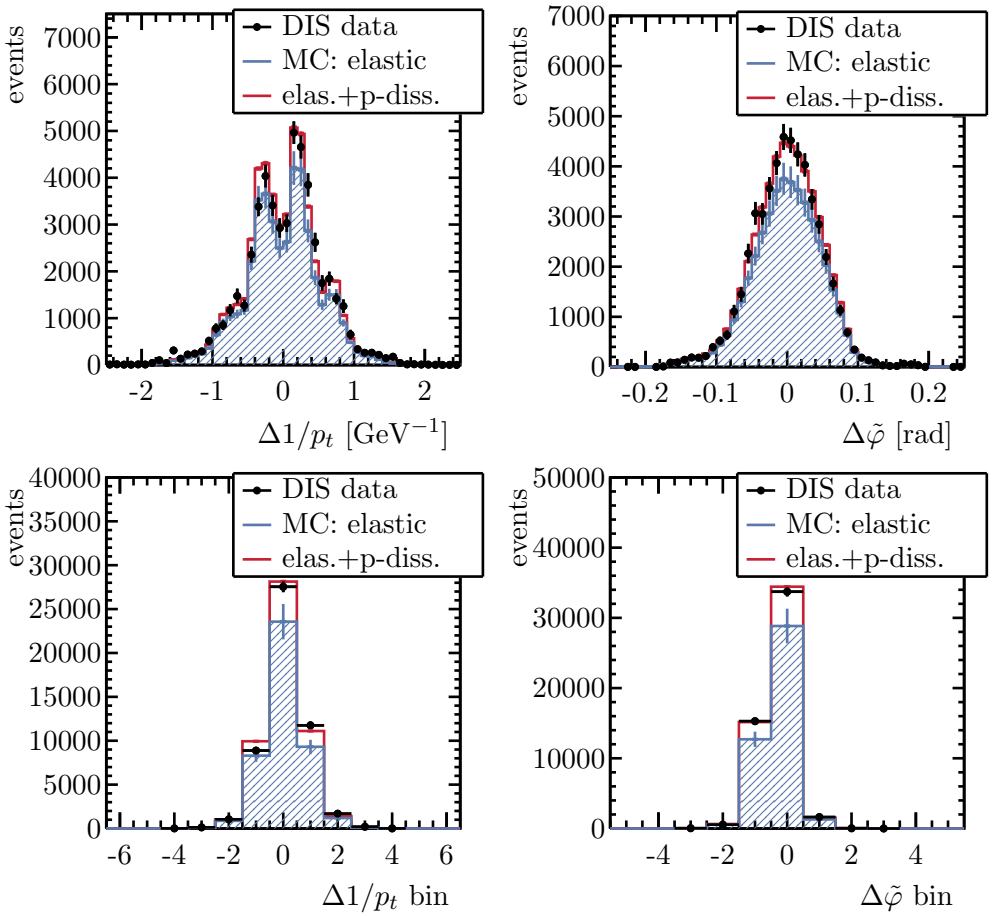

Figure 4.3.4: FTT resolution in $1/p_t$ (left) and $\tilde{\varphi}$ (right), direct (top) and binned (bottom) as measured in the DIS $\rho^0 \to \pi^+\pi^-$ data sample introduced in Chapter 6 and the corresponding MC sample introduced in Chapter 5. The structures in $\Delta 1/p_t$ are a consequence of the discretization of the FTT $1/p_t$ values.

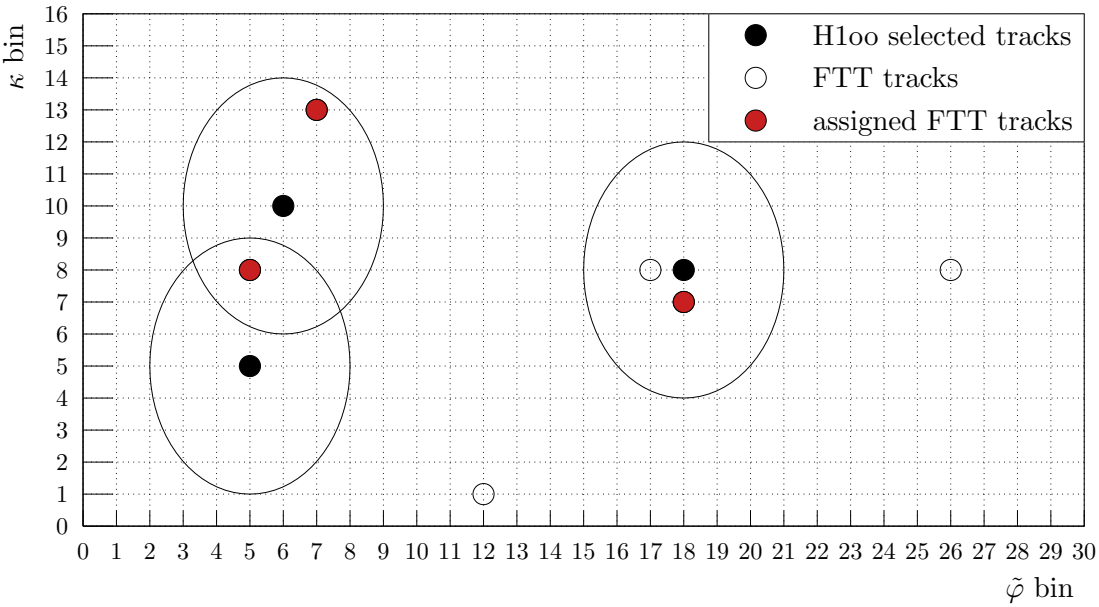

Figure 4.3.5: Example of a pseudo-event in the $1/p_t$-$\tilde{\varphi}$-plane (for simplicity only 30 $\tilde{\varphi}$ bins are shown) containing reconstructed and FTT tracks. The ellipses around the reconstructed tracks show the compatibility region. FTT tracks outside of this region are not allowed to be assigned. The red points mark the assignments obtained by using the metric defined in Equation (4.3.1) and by simultaneously maximizing the number of assignments and minimizing the sum of distances between assigned tracks.

Reconstructed and FTT tracks are considered compatible if

$$\Delta^{bin}_{rec,\ FTT} \leq 5. \tag{4.3.4}$$

In the general case a reconstructed track can have more than one compatible FTT track and one FTT track can be compatible with more than one reconstructed track. So the track matching is still not trivial and has to happen for all tracks in an event simultaneously. This is guided by two principles: First, the number of assigned tracks should be maximal. Second, the sum of distances between assigned tracks should be minimal. To achieve such an assignment an algorithm in the spirit of the *Hungarian Method* [100] was implemented.[3] The steps performed by the algorithm are summarized in Appendix A where also a small example is given. A graphic example for the assignment of FTT to reconstructed tracks is also shown in Figure 4.3.5.

[3]The implementation of the Hungarian Method in C++ was inspired by the Munkres python module: software.clapper.org/munkres/.

5 Monte Carlo Modeling and Reconstruction of Kinematic Variables

5.1 Monte Carlo Modeling

Particle detectors are lenses through which the microcosmos of high energy particle interactions can be observed. But they are incredibly complicated machines and what is seen through them is but a washed out image of what has truly happened in the interactions. The actual signals produced by a particle in the detector strongly depend on the detailed detector geometry, on the amount and position of dead material, on dead channels, and on many more fine details. In order to be able to separate true physics phenomena in the interactions from mere detector effects, these details need to be understood.
A powerful tool to help understand detector effects is computer simulation of processes to be studied and how they would be observed with the detector at hand. A full simulation thus typically contains three steps:

- **Event Generation:**
  Events for the physics process to be studied are generated according to a given model, i.e., four vectors of the stable final state particles are created by randomly sampling the model distributions. For this analysis the DiffVM [101] generator for the diffractive production of vector mesons is used.
- **Simulation:**
  The detector is modeled and the passage of the particles obtained from the event generator through the detector is simulated together with the detector response to them. The simulation software used for H1 is H1SIM, which in turn heavily relies on the GEANT [102] software package describing interactions of particles with material.
- **Reconstruction:**
  The output of the detector simulation is processed by the same reconstruction software that is also used to reconstruct true data: H1Rec. In addition information about the true underlying event is stored.

A good simulation of course requires good models for the first and second step. The evaluation of these models typically relies on random number sampling, i.e., so called *Monte Carlo* methods. That's why in the following simulated data samples are referred to as Monte Carlo (MC) samples.

5.1.1 The DiffVM Generator

For the analysis at hand MC samples of events generated by the DiffVM event generator [101] are used. DiffVM simulates the diffractive production of various vector mesons in ep scattering within the framework of Regge theory and the Vector Dominance Model. It allows simulating both proton elastic and proton dissociative scattering events. The main steps in the generation of an event shall be briefly discussed.

Weizsäcker-Williams Approximation

In the first step, the incoming electron is assumed to generate a virtual photon γ^*. This allows to treat diffractive electron-proton scattering in terms of diffractive photon-proton scattering. Given the flux $\mathcal{F}_{\gamma^*}$ of photons emitted by the electron, the ep cross section σ_{ep} is related to the $\gamma^* p$ $\sigma_{\gamma^* p}$ cross section in the following way:

$$\frac{\mathrm{d}^2\sigma_{ep}}{\mathrm{d}y\mathrm{d}Q^2} = \mathcal{F}^T_{\gamma^*}(y, Q^2)\, \sigma^T_{\gamma^* p}(W_{\gamma p}, Q^2) + \mathcal{F}^L_{\gamma^*}(y, Q^2)\, \sigma^L_{\gamma^* p}(W_{\gamma p}, Q^2). \tag{5.1.1}$$

In particular, it is considered explicitly that virtual photons can be transversely (superscript T) and longitudinally polarized (superscript L) with different respective cross sections and flux factors. y, Q^2, and $W_{\gamma p}$ are the inelasticity, photon virtuality and photon-proton center of mass energy, as defined in Section 2.4.1.

The longitudinal and transverse flux factors are obtained from the *Weizsäcker-Williams Approximation* (WWA) [103–106]

$$\mathcal{F}^T_{\gamma^*} = \frac{\alpha_{em}}{2\pi}\frac{1}{yQ^2}\left(1 + (1-y)^2 - 2m_e^2\frac{y^2}{Q^2}\right) \tag{5.1.2}$$

$$\mathcal{F}^T_{\gamma^*} = \frac{\alpha_{em}}{\pi}\frac{1}{yQ^2}(1-y^2). \tag{5.1.3}$$

From Photons to Vector Mesons

In the spirit of vector dominance models, the (hadronic) photon is interpreted as a superposition of vector mesons and the photon-proton cross sections are expressed

in terms of vector-meson-proton cross sections. For the exclusive production of one type of vector meson (VM), the production cross section for transversely polarized vector mesons in DiffVM has the phenomenological Q^2 dependence

$$\sigma^T_{\gamma^* p}(Q^2) = \sigma^{\mathrm{VM}}_{\gamma p} \left(\frac{1}{1 + \frac{Q^2,}{\Lambda^2}} \right)^l \tag{5.1.4}$$

and is assumed not to depend on $W_{\gamma p}$. $\sigma^{\mathrm{VM}}_{\gamma p}$ is the photoproduction cross section ($Q^2 = 0\,\mathrm{GeV}^2$) that needs to be measured and put into DiffVM as a normalization factor, the exponent l is a purely phenomenological parameter and Λ is typically set to the vector meson's mass m_{VM}.

For longitudinally polarized vector mesons, the cross section is of form

$$\sigma^L_{\gamma^* p}(Q^2) = R(Q^2)\, \sigma^T_{\gamma^* p}(Q^2) = \frac{\xi \frac{Q^2}{\Lambda^2}}{1 + \chi \xi \frac{Q^2}{\Lambda^2}}\, \sigma^T_{\gamma^* p}(Q^2), \tag{5.1.5}$$

where the function $R(Q^2)$ is again purely phenomenological and the parameters ξ and χ need to be specified. $R(Q^2)$ is in particular chosen such, that $\sigma^L_{\gamma^* p}(Q^2) \to 0\,\mu\mathrm{b}$ in the photoproduction limit $Q^2 \to 0\,\mathrm{GeV}^2$ of purely transversely polarized, real photons.

Pomeron Exchange

The vector-meson-proton scattering is described in terms of pomeron exchange, with the pomeron trajectory being parameterized by

$$\alpha_{\mathbb{P}}(t) = \alpha_{\mathbb{P}}(0) + \alpha'_{\mathbb{P}} t = 1 + \epsilon + \alpha'_{\mathbb{P}} t. \tag{5.1.6}$$

The differential cross section with respect to the squared proton momentum transfer t is then given by:

$$\frac{\mathrm{d}\sigma}{\mathrm{d}t} = \left.\frac{\mathrm{d}\sigma}{\mathrm{d}t}\right|_{t=0, W_{\gamma p} = W_0} e^{-b|t|} \left(\frac{W_{\gamma p}}{W_0} \right)^{4\epsilon} \tag{5.1.7}$$

with

$$b(W_{\gamma p}) = b(W_0) + 4\alpha'_{\mathbb{P}} \ln \left(\frac{W_{\gamma p}}{W_0} \right). \tag{5.1.8}$$

Again, W_0, $b(W_0)$, $\sigma(W_0) = \int_{t_{min}}^{t_{max}} \frac{\mathrm{d}\sigma}{\mathrm{d}t} \mathrm{d}t \equiv \sigma^{\mathrm{VM}}_{\gamma p}$, ϵ and $\alpha'_{\mathbb{P}}$ need to be specified by the user.

By the interaction with the proton the to this point virtual vector meson is pushed on its mass shell. Its mass is generated following a non-relativistic Breit-Wigner [78] function with mean m_{VM} and width Γ_{VM}.

Table 5.1.1: DiffVM parameter settings for exclusive $\rho^0 \to \pi^+\pi^-$ production. Parameters tagged ^{gen} are changed in the reweight procedure.

	$\sigma^{\rho}_{\gamma p}$ [μb]	l	Λ [GeV]	ξ	χ	ϵ^{gen}	α'^{gen} [GeV^{-2}]	W_0 [GeV]	b^{gen} [GeV^{-2}]
p-elastic	13.8	2.4	m_ρ	0.42	0.3	0.0808	0.0	90	5
p-dissoc.	13.8	2.4	m_ρ	0.42	0.3	0.0808	0.0	90	2

Proton Dissociation

Finally, DiffVM also allows for a diffractive dissociation of the proton in the final state. The mass spectrum of the proton remnants Y is modeled according to

$$\frac{\mathrm{d}\sigma}{dM_Y^2} \propto \frac{f(M_Y^2)}{M_Y^{2(1+\epsilon)}}, \tag{5.1.9}$$

where the function $f(M_Y^2)$ is obtained as follows: For masses below $M_Y^2 = 3.6\,\mathrm{GeV}^2$ a fit to the measured differential cross section for diffractive proton dissociative scattering off a deuterium target, $pD \to YD$ [107, 108] is used. In particular, several N^{*+} resonances ($N(1440)$, $N(1520)$, $N(1680)$, and $N(1700)$) observed there are included. Depending on the mass of the dissociated system it is assumed to be either of them and the decay is modeled along the lines of the according measured branching ratios [17]. In the continuum region, i.e., for masses $M_Y^2 \gtrsim 3.6\,\mathrm{GeV}^2$, $f(M_Y^2)$ is set to one and the proton is modeled as a quark-diquark system. The quark is assumed to be knocked free in the scattering and the following hadronization is modeled using Lund fragmentation as implemented in JETSET [109].

5.1.2 MC Data Samples

Several MC samples are used in the following analyses and shall be introduced here.

DIS $\rho^0 \to \pi^+\pi^-$ Sample

In Chapter 7 the Fast Track Trigger is studied using a data sample of real H1 $e\,p \to e\,\rho^0(\pi^+\pi^-)\,p$ events in the deep inelastic regime. To validate the studies, a corresponding MC sample is simulated. This sample contains both proton-elastic and dissociative $\rho^0 \to \pi^+\pi^-$ events generated with DiffVM. The chosen DiffVM parameters are listed in Table 5.1.1. The parameters l, Λ, ξ, and χ are set according to [18]. The normalization, i.e., $\sigma^{\rho}_{\gamma p}$, as well as ϵ, α', and b^{gen} are

only rough estimates and the kinematic distributions of the DiffVM sample are later reweighted to describe the data distributions. The reweighting procedure is discussed below.

Reweighting in $m_{\pi^+\pi^-}$

In DiffVM the differential cross section as a function of the invariant dipion mass $m_{\pi^+\pi^-}$ follows a non-relativistic Breit-Wigner parametrization.

$$BW_{nr}(m_{\pi^+\pi^-}) = \frac{0.25\Gamma^2_{\rho,0}}{(m_{\pi^+\pi^-} - m_\rho)^2 + 0.25\Gamma^2_{\rho,0}} \tag{5.1.10}$$

The measured shape of the ρ^0 mass peak, on the other hand, has the shape of a skewed relativistic Breit-Wigner [40], which can be described by the parametrization of Ross and Stodolsky [110]:

$$BW_{RS}(n; m_{\pi^+\pi^-}) = \frac{m_\rho m_{\pi^+\pi^-}\Gamma_\rho}{(m_\rho^2 - m^2_{\pi^+\pi^-})^2 + (m_\rho\Gamma_\rho)^2} \cdot \left(\frac{m_\rho}{m_{\pi^+\pi^-}}\right)^n. \tag{5.1.11}$$

To better match the measured data sample, the MC DIS sample is reweighted in the generated $\pi^+\pi^-$ mass to this shape. In agreement with [40] a skewing parameter $n = 1.5$ is chosen, which seems to describe the data in the considered phase-space best. The mass dependent weight is defined as follows:

$$w(m_{\pi^+\pi^-}) = \frac{BW_{RS}(n; m_{\pi^+\pi^-})/\int_{m_{low}}^{m_{high}} BW_{RS}(n=0; m)\mathrm{d}m}{BW_{nr}(m_{\pi^+\pi^-})/\int_{m_{low}}^{m_{high}} BW_{nr}(m)\mathrm{d}m}. \tag{5.1.12}$$

Figure 5.1.1 (left) shows the mass distribution of the DiffVM sample before and after reweighting compared to the measured data.

Reweighting in $W_{\gamma p}$ and t

For the generation of the MC samples the parameters defining the t and $W_{\gamma p}$ dependence of the cross section are only set to rough estimates. In order to bring data and MC into better agreement, the MC samples are reweighted in t and $W_{\gamma p}$ with slightly modified parameters as specified in Table 5.1.2. The parameters are tuned in agreement with measurements by the H1 Collaboration [40]. The applied weight is given by:

$$w(W_{\gamma p}, t) = \frac{\mathrm{e}^{b_0 t} \cdot b_0 \cdot \left(\frac{W_{\gamma p}}{W_0}\right)^{4(\epsilon+\alpha' t)}}{\mathrm{e}^{b_0^{gen} t} \cdot b_0^{gen} \cdot \left(\frac{W_{\gamma p}}{W_0}\right)^{4(\epsilon^{gen}+\alpha'^{gen} t)}}. \tag{5.1.13}$$

The t distribution before and after reweighting is shown in Figure 5.1.1 (right).

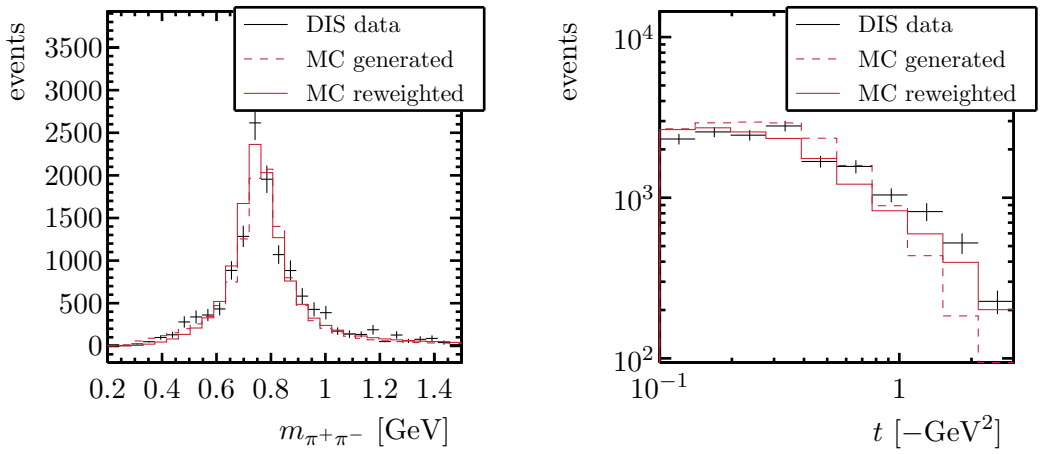

Figure 5.1.1: $m_{\pi^+\pi^-}$ (left) and t distribution (right) for DIS $\rho \to \pi^+\pi^-$ events in data and the combined elastic and proton dissociative MC sample before and after reweighting (continuous). Events are selected as described in Chapter 6. In addition the $m_{\pi^+\pi^-}$ distribution is only shown for events with $t > -0.2\,\text{GeV}^2$ and the t distribution for events in the range $625\,\text{MeV} < m_{\pi^+\pi^-} < 925\,\text{MeV}$ to exclude irreducible background (see also Chapter 6).

Table 5.1.2: Parameter settings for reweighting the MC input distributions in $m_{\pi^+\pi^-}$, $W_{\gamma p}$ and t

		proton elastic (dissociative)	
	parameter	adjusted	generated
$m_{\pi^+\pi^-}$	n_0	1.5	-
$W_{\gamma p}$ and t	ϵ	0.08	0.0808
	α' [GeV^{-2}]	0.15	0
	b_0 [GeV^{-2}]	6.9 (1.5)	5 (2)

Normalization

The measured data sample contains contributions from both proton elastic as well as proton dissociative events (and additionally from various small background contributions which were, however, not simulated for this thesis). Unfortunately, in the considered phasespace the cross sections for the two processes are not known. In order to obtain the right normalizations the combined MC sample is fitted to the measured data via a template fit.

One possible way to distinguish the proton elastic from the dissociative events is by looking at the energy deposit in the forward region of the calorimeter, i.e., in the forward region of the LAr or the plug calorimeter. The distributions of those

energy deposits are shown in Figure 5.1.2. A template fit of the form

$$N_{data}(E) = A \cdot (f \cdot N_{elas}(E) + (1 - f) \cdot N_{pdis}(E)) \,, \tag{5.1.14}$$

where $N(E)$ is the number of events in a given energy bin, A a normalization and f the fraction of elastic events, is performed to determine the correct normalizations for the two MCs. The obtained fit values are listed in Table 5.1.3.

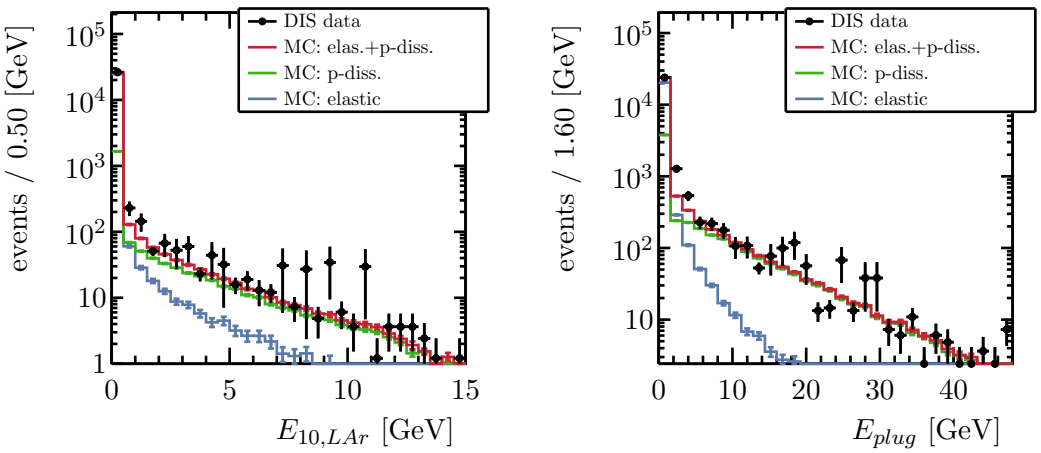

Figure 5.1.2: Energy deposit in the forward region of the LAr calorimeter ($\theta < 10°$, left) and in the plug (right) in the DIS sample (see Chapter 6). The normalization of the elastic and proton dissociative MC sample is determined by a template fit to the data distributions such that the combined sample describes the data best.

Table 5.1.3: Scaling factors for the elastic and proton dissociative MC obtained from a template fit to the distribution of the energy in the forward region of the LAr and the plug calorimeter. The combined value is the average, the uncertainty is estimated to be half the difference of the two obtained values.

	$E_{10,LAr}$	E_{plug}	combined	uncertainty
A	0.108	0.106	0.107	0.001
f	0.917	0.782	0.850	0.067

The averages of the values obtained from fitting the plug and the LAr energy distributions are used in the following to normalize the MC sample. An uncertainty on the combined values is estimated by half the differences between the two values. In all MC plots, in particular those shown in Chapter 6 and Chapter 7, the

uncertainty from the normalization is included as a systematic uncertainty and added quadratically to the (mostly negligible) statistical uncertainty.

Photoproduction $\rho^0 \to \pi^+\pi^-$ Sample

To be able to extrapolate the results obtained in the DIS regime to the photoproduction regime, a photoproduction $\rho^0 \to \pi^+\pi^-$ MC sample is used in Chapter 8. It contains elastic and proton dissociated events generated by DiffVM. The generator settings are chosen equivalently to the DIS settings as listed in Table 5.1.1. The reweighting procedure for the photoproduction sample in principle follows the steps described previously. However, in photoproduction the skewing of the ρ^0 mass peak is stronger and additionally the t-dependence of the differential cross section is more complex than a simple exponential. The reweighting is performed following the prescription of Weber [18, Chapter 3] using the weight formulae and parameters given there. Equivalently to the DIS sample, the normalization of the DiffVM photoproduction sample is obtained by fitting the forward LAr and Plug energy distributions.

Single Track MC

Single track samples of pions and muons are generated and the passage of the particles through the detector is simulated. The generated distributions are flat in track momentum p, azimuthal angle φ, and polar angle θ. These samples are used to study detector effects on isolated tracks without the influence of other tracks in an event.

5.2 Reconstruction of Kinematic Variables

The kinematic of the full $2 \to 4$ scattering process $e\,p \to e\,\pi^+\pi^-\,p$ is described by a total of 6 four momenta, corresponding to $6 \cdot 4 = 24$ free parameters. With the initial $e\,p$ state fixed - which strictly speaking is not the case because of variations in the beam conditions and initial state radiation - and energy and momentum conservation taken into account a total of 12 degrees of freedom remain. For proton elastic scattering, where all masses of the final state particles are known, this number reduces to 8 while for proton dissociative scattering the unknown invariant mass of the proton fragment gives an additional 9^{th} parameter.

This section deals with the questions, what variables can be measured with the H1 detector, with the goal of reconstructing 8 (reconstructing the mass of the proton remnant in proton-dissociation is not considered) independent parameters and thus the full event. Here, a distinction between deep inelastic scattering events,

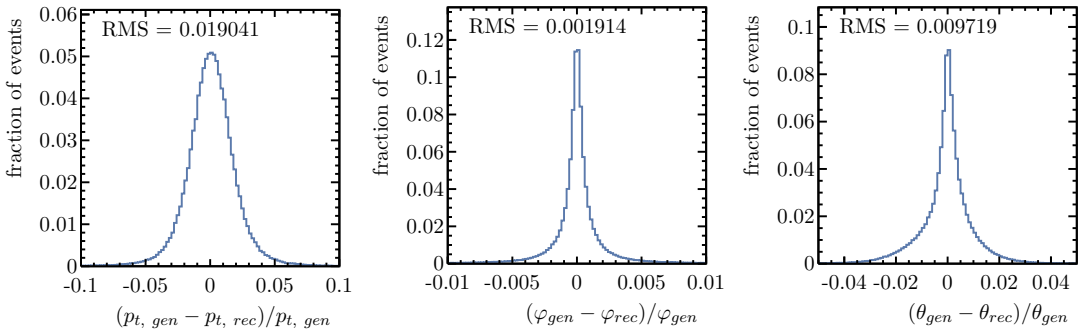

Figure 5.2.1: Resolution of the π^+ track quantities p_t, φ, and θ as measured in the elastic DIS $\rho^0 \to \pi^+\pi^-$ DiffVM MC.

where the scattered electron is measured, and photoproduction events, where it is not, needs to be made.

Of particular interest is the question how *well* a given variable X can be measured. This can be studied with MC simulated events, where the reconstructed value X_{rec} can be compared to its originally generated counterpart X_{gen}. In the following, resolution plots obtained from the elastic ρ^0 DIS sample are shown for discussed variables, i.e., distributions of the form

$$\Delta X = \frac{X_{gen} - X_{rec}}{X_{gen}}. \tag{5.2.1}$$

5.2.1 Track Parameters

The two pion candidate tracks are measured by the H1 tracking system, which determines the (transverse) track momentum and directional information. In Figure 5.2.1 the p_t, φ, and θ resolutions are shown for positive tracks. As they do not depend on the charge of the track at the given level of detail, similar plots for the negative tracks are omitted here.

In DIS events, additional information comes from the scattered electron which can be observed in the SpaCal. Given its high momentum, the directional information of the electron track can be determined from the cluster position. The energy of the scattered electron can either be taken from the SpaCal cluster size directly, or by exploiting energy-momentum conservation and the available information from the pion tracks. The latter provides a better resolution for the electron energy, which can be calculated via [111]

$$e'_E = \frac{2e_E - k_E + k_z}{1 - \cos(\theta_{e'})}, \tag{5.2.2}$$

where all involved quantities are defined in Section 2.4.1. The resolutions for e'_E, $\varphi_{e'}$ and $\theta_{e'}$, respectively, are shown in Figure 5.2.2.

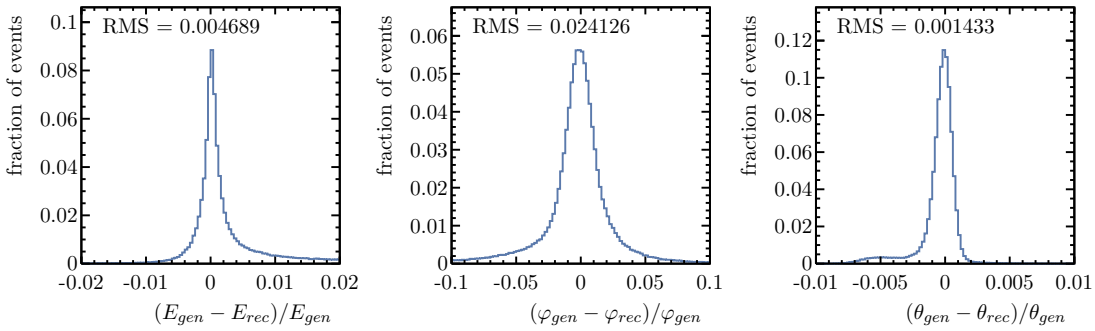

Figure 5.2.2: Resolution of the scattered electron quantities E, φ, and θ as measured in the elastic DIS $\rho^0 \to \pi^+\pi^-$ DiffVM MC. The structure in θ is due to edge effects at low scattering angles, where the electron shower is not fully contained in the SpaCal. This is responsible for the tail in the E resolution, as well.

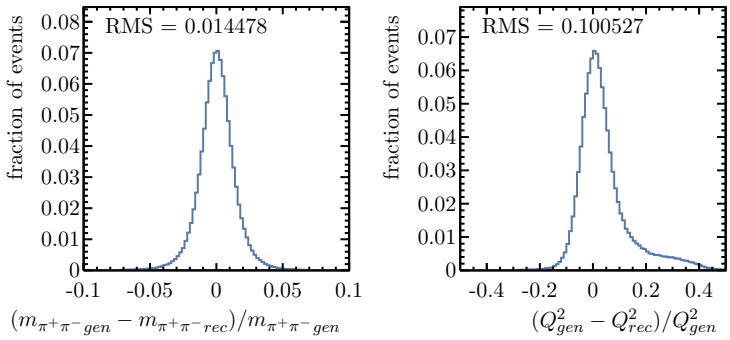

Figure 5.2.3: Respective $m_{\pi^+\pi^-}$ and Q^2 resolutions as measured in the elastic DIS $\rho^0 \to \pi^+\pi^-$ DiffVM MC.

5.2.2 Event Variables

DIS

In DIS events two pion and the electron four-momenta fully determine the event kinematics. In principle, all other kinematic variables can be calculated from them. What is used in this thesis are in particular the invariant mass of the $\pi^+\pi^-$ system $m_{\pi^+\pi^-}$, the photon virtuality Q^2, the photon-proton center of mass energy $W_{\gamma p}$, and the squared proton momentum transfer t. The first three can be directly calculated via

$$m_{\pi^+\pi^-} = \sqrt{(k_1 + k_2)^2}, \tag{5.2.3}$$

$$Q^2 = -(e - e')^2 = 4 e_E e'_E \cos^2\left(\frac{\theta_{e'}}{2}\right), \tag{5.2.4}$$

$$W^2_{\gamma p} = (p + e - e')^2. \tag{5.2.5}$$

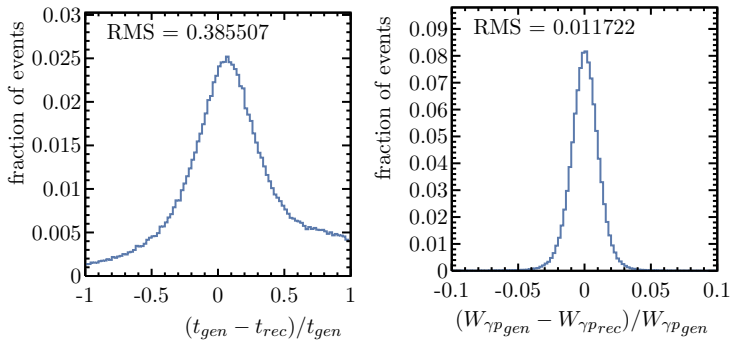

Figure 5.2.4: Respective t and $W_{\gamma p}$ resolutions as measured in the elastic DIS $\rho^0 \to \pi^+\pi^-$ DiffVM MC.

For the proton momentum transfer, on the other hand, an indirect approach is necessary, as the scattered proton is not measured. It can be calculated via [111]

$$t = (p - p')^2 \simeq -(k_t + e'_t)^2. \tag{5.2.6}$$

For all four variables, the respective DIS resolutions are shown in Figure 5.2.3 and Figure 5.2.4.

Photoproduction

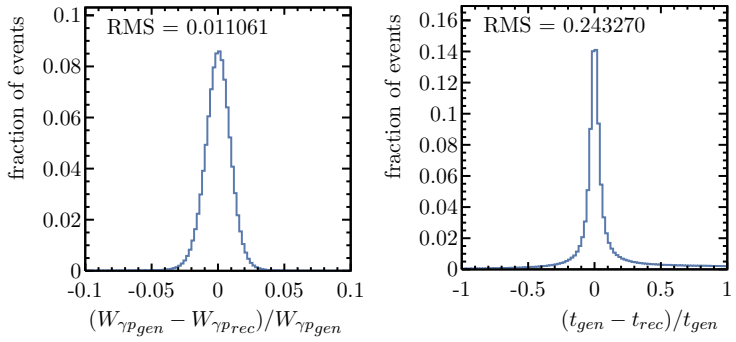

Figure 5.2.5: $W_{\gamma p}$ and t resolution as measured in the elastic photoproduction $\rho^0 \to \pi^+\pi^-$ DiffVM MC.

In the experimental context of the H1 detector, photoproduction events are per definition those, where the scattered electron is not observed. This includes events with Q^2 up to $5\,\mathrm{GeV}^2$. As only the pion track information is available the event cannot be fully reconstructed. Among the variables used here, in particular $W_{\gamma p}$ and t cannot be calculated using Equation (5.2.5) and Equation (5.2.6) anymore. Instead approximations have to be used. The underlying assumption is that if

the electron is not observed, then $Q^2 \simeq 0\,\mathrm{GeV}^2$. $W_{\gamma p}$ and t can then be estimated by [18]

$$W_{\gamma p} \simeq 2(k_E - k_z), \tag{5.2.7}$$

$$t \simeq -k_T^2. \tag{5.2.8}$$

The corresponding resolutions are shown if Figure 5.2.5.

6 DIS $\rho^0 \to \pi^+\pi^-$ Data Sample

The aim of the second part of this thesis is to study the properties of the Fast Track Trigger for triggering dipion photoproduction events (see Chapter 7). For this an unbiased reference sample triggered without relying on FTT information is needed. Also, it should have a similar event topology to dipion photoproduction, i.e., it should consist of events with nothing but two low momentum, oppositely charged pion tracks in the central tracker. The best choice for such a sample are ρ^0 events decaying into a $\pi^+\pi^-$ final state[1] in the kinematic regime of DIS. In such events the electron is strongly deflected and for $Q^2 \gtrsim 2.5\,\mathrm{GeV}$ lies in the acceptance of the SpaCal. Consequently, these events can be triggered by purely SpaCal-based subtriggers.

Kinematically, ρ^0 production in DIS is similar to ρ^0 photoproduction as long as Q^2 stays reasonably small. The main difference then is in the transverse momentum of the vector meson, i.e., the $\pi^+\pi^-$ system. In photoproduction it is of the order $p_t \sim \sqrt{-t} \simeq 0\,\mathrm{GeV}$ while in DIS it is of the order of $p_t \sim \sqrt{Q^2} \gtrsim 0\,\mathrm{GeV}$.

In this section, the selection criteria for the used DIS $\rho^0 \to \pi^+\pi^-$ data sample are documented.

6.1 Run Selection and Triggers

The sample is collected from data taken during the 2006/2007 HERA run period. Only runs at high proton energy (920 GeV) and with a colliding positron beam are considered. This corresponds to run numbers in the range 468531-500611. Additionally each of the individual runs needs to satisfy some quality criteria. Namely, it is required that the following sub-detectors were powered and active during the run:

`CJC, CIP, FPS, FTT, LAr, SpaCal, TOF, LUMI, VETO,`

and that the z-position of the primary vertex is within 35 cm of the nominal interaction point.

[1] The distinction between inclusive $\pi^+\pi^-$ production and resonant ρ^0 production is made here, because on the part of the MC sample used for comparison (see Chapter 5) only ρ^0 events are simulated. For the data sample this requires in particular an upper limit for the considered invariant $\pi^+\pi^-$ mass range, such that ρ^0 events dominate the sample.

Table 6.1.1: Subtriggers used for the data sample and their respective prescales.

subtrigger	s0	s1	s2
average prescale	5.3	24.8	1.3

Events have to be triggered by one of the SpaCal-based L1 subtriggers `s0, s1`, or `s2`. They are defined as follows

`s0: SPCLe_IET>1 v:3 f:0 z:0 L2[22]`

`s1: SPCLe_IET>2 || SPCLe_IET_Cen_3 v:3 f:0 z:1`

`s2: SPCLe_IET>2 v:3 f:0 z:1 L2[22]`,

where the trigger elements have the following meanings (`||` and `&&` are the logical *or* and *and* operators):

`SPCLe_IET`:	Two-bit inclusive electron trigger element: The three possible values indicate whether a cluster in one of 5×5 designated SpaCal regions exceeds the low (2.1 GeV), medium (6.0 GeV), or high (9.0 GeV) energy threshold.
`SPCLe_IET_Cen_3`:	Active if the energy deposited in the central IET region exceeds the high threshold.
`v:3`, `f:0`, `z:0`, `z:1`:	Various H1 standard vetoes against background, e.g. due to beam-gas interactions.
`L2[22]`:	L2-veto on clusters with a radial position smaller than 20 cm.

All three subtriggers are prescaled, i.e., only a fraction of the events satisfying the trigger criteria are actually considered. The average prescales for the run period at hand are documented in Table 6.1.1. To combine events correctly into a consistent data sample, they are reweighted according to the prescales factors under consideration of trigger overlaps. The reweighting procedure follows the prescription by Egli et al. [112]; an example can be found in Sauter's PhD thesis [113, Appendix E].

6.2 Event Selection

From the inclusive sample of SpaCal triggered DIS events, $e\,p \to e\,\rho^0(\pi^+\pi^-)\,p$ events are to be isolated. The event topology is thus very simple: In addition to the scattered electron cluster in the SpaCal, there should be precisely two low momentum tracks of opposite charge in the central tracker. In Figure 6.2.1 an

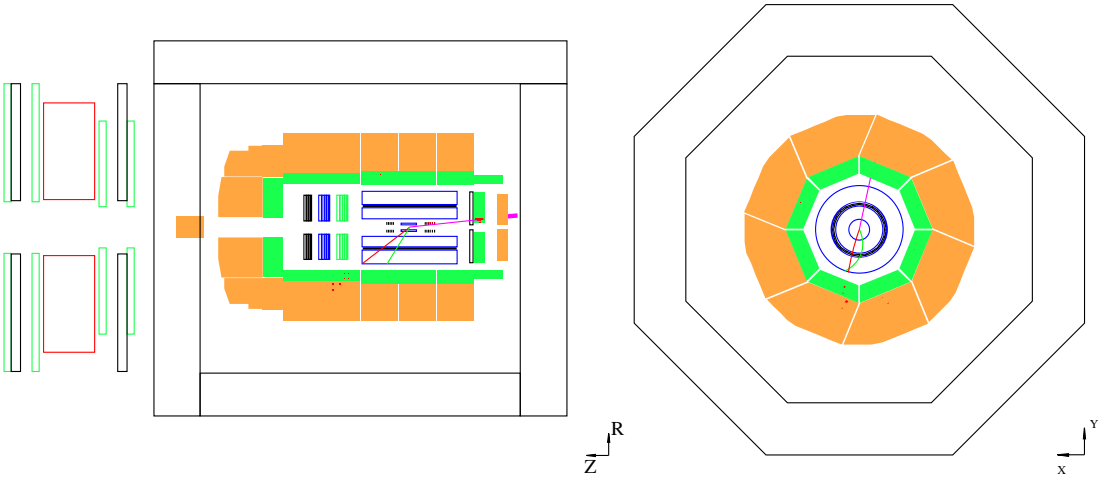

Figure 6.2.1: H1 event display for a selected DIS event. The two pion candidates in red and green are seen by the central tracker and leave a small signal in the LAr calorimeter. The scattered electron in magenta leaves hits in the BST and deposits all of its energy in the electromagnetic SpaCal.

H1 event display with such a topology is shown. Events that do not satisfy these criteria can be immediately discarded. To suppress backgrounds with the same topology, various selection cuts are implemented.

Track Multiplicity and Quality

To obtain two pion candidates, only events with precisely two tracks of opposite charge are considered; a third track is allowed only if it is associated to the scattered electron. The pion candidate tracks have to be primary vertex fitted *central tracks* reconstructed from hits in the central tracker. In particular, events with additional non-vertex fitted tracks from background processes such as beam-gas interactions or cosmic particles, are discarded.

The two pion tracks have to satisfy additional standard H1 track quality requirements:

- They need to be within the acceptance region of the CJC defined by:

$$p_t > 200\,\text{MeV} \quad \text{and} \quad 20^\circ < \theta < 160^\circ. \tag{6.2.1}$$

- The radial track length of the reconstructed tracks in the CJC must not be smaller than 10 cm.
- The distance of closest approach to the primary vertex d_{ca} should not exceed 10 mm in the transverse plane.

Vertex Constraints

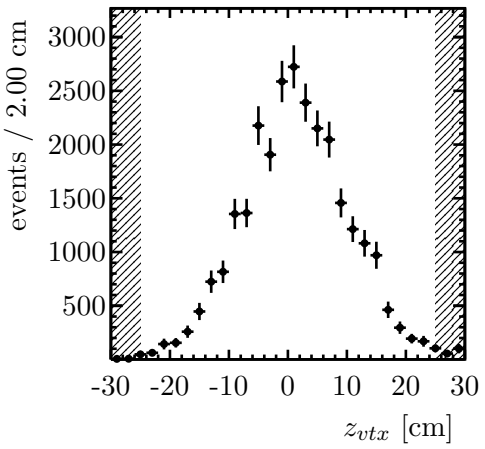

Figure 6.2.2: Z-vertex distribution. Events inside of the shaded area are excluded in order to suppress background from beam restgas interactions.

Events are required to have a z-position z_{vtx} of the reconstructed primary vertex within 25 cm of the nominal interaction point. This cut is supposed to suppress events originating from interactions between either of the beams and the rest gas atoms in the beampipe or the beampipe itself. While the z-vertices of such events are spread constantly along the beam axis, signal events from beam-beam interactions create a gaussian shaped z-vertex distribution with a width of about 8 cm. See also Figure 6.2.2. The fraction of such beam-gas interaction events can be estimated from fitting the z-vertex distribution with a gaussian plus an additional constant offset. Within the signal region it is fitted to be less than 2%.

Scattered Electron

In addition to the electron criteria imposed by the subtriggers, further measures are taken to ensure that the SpaCal signal comes indeed from the scattered electron. The SpaCal must not contain more than a single, isolated energy cluster with an energy above 17 GeV. Furthermore, events in selected regions of the SpaCal are excluded by fiducial cuts, following the prescription by Jung [114]. These selected regions are either inefficient or dead SpaCal cells or hot cells that were not implemented for the trigger. Also cells at a radial position of less than 12 cm are excluded to avoid edge effects: If the electromagnetic shower is not completely contained in the SpaCal, this leads to a false reconstruction of the scattered electron.

For small scattering angles, i.e., large polar angles $\theta_{e'} \lesssim 170°$, the electron starts

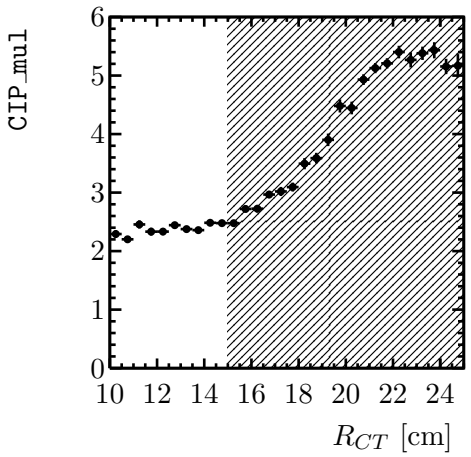

Figure 6.2.3: CIP multiplicity as a function of the electron track radius $R_{e',CT}$ at the central tracker edge $z_{CT} = -115\,\text{cm}$. The shaded area, starting at the inner radius of the CIP at 15 cm, marks the region that is excluded to avoid electrons in the central tracker.

penetrating the central tracker. Such events which have an additional track in the CJC are not wanted, if the FTT is to be studied under $\pi^+\pi^-$ photoproduction conditions. However, a simple cut on $\theta_{e'}$ is not a good way to avoid them because of the large variation in the primary vertex position. To correct for this variation the geometrical radial position $R_{e',CT}$ of the electron track at the edge of the central tracker along the z-axis is calculated. The central tracker ends at $z_{CT} = -115\,\text{cm}$ so that $R_{e',CT}$ is given by

$$R_{e',CT} = -\tan(\theta_{e'})(z_{vtx} - z_{CT}). \tag{6.2.2}$$

Figure 6.2.3 shows the average CIP multiplicity per event as a function of $R_{e',CT}$. Since the CIP is the innermost part of the central tracker, with a radius of 15 cm the rise in the multiplicity starting at $R_{e',CT} \sim 15\,\text{cm}$ indicates that the scattered electron traverses the central tracker. To avoid this, events with $R_{e',CT} > 15\,\text{cm}$ are rejected.

Unassociated Energy

Background processes with additional neutral particles in the final state (e.g. $\omega \to \pi^+\pi^-\pi^0$ [17]) cannot be rejected by track multiplicity constraints. However, the neutral particles can leave a signal in the calorimeter. To suppress such events, it is required that there is no unassociated energy cluster above a noise level of 400 MeV in the LAr calorimeter. A cluster is associated to one of the pion candidates, if it is within a cylinder of a radius of 30 cm, centered at the

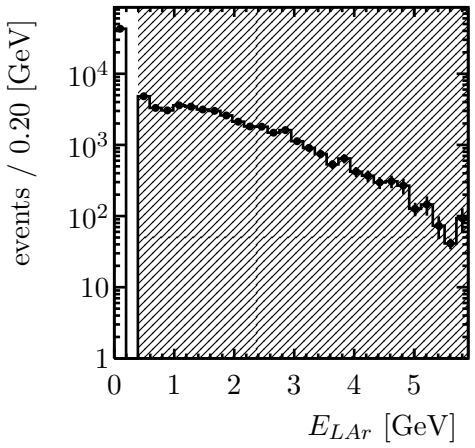

Figure 6.2.4: Total energy of all unassociated clusters above noise in the region $\theta > 10°$ in the LAr calorimeter. Events that exceed this energy are excluded, as indicated by the shaded area.

position where the track trajectory enters the calorimeter and parallel to the track momentum at that position.

Also, clusters at angles $\theta < 10°$ are not counted. This region is prone to be hit by the proton remnants in proton dissociative events and the deposited energy can later be used to estimate the contribution from proton dissociative events. See Section 5.1.2. The distribution of the summed unassociated energy in the LAr is shown in Figure 6.2.4.

Particle Identification

The energy loss via ionization in the central tracker is measured for every track and can be used for particle identification. The specific energy loss per path length, dE/dx, as described by the Bethe-Bloch formula, depends on a particle's velocity β [17]. For a given momentum it can thus be used to determine a particle's mass, i.e., the species the particle belongs to:

$$m = p\sqrt{1/\beta^2 - 1}. \tag{6.2.3}$$

However, this works well only for low momentum particles because of two reasons:

i) At small velocities $dE/dx \sim 1/\beta^2$. So at a given momentum even a small mass difference, which induces a small difference in velocity, gives rise to a large difference in the energy loss. At high velocities, on the other hand, the β-dependence is logarithmic such that the specific energy losses get similar for particles with different masses.

ii) At the same time, the difference in velocity between particles with different masses but having the same momentum is quite substantial at low momenta, but becomes more and more negligible at higher momenta.

In Figure 6.2.5 the measured dE/dx values are plotted versus the particle momentum for all tracks still considered at this point.

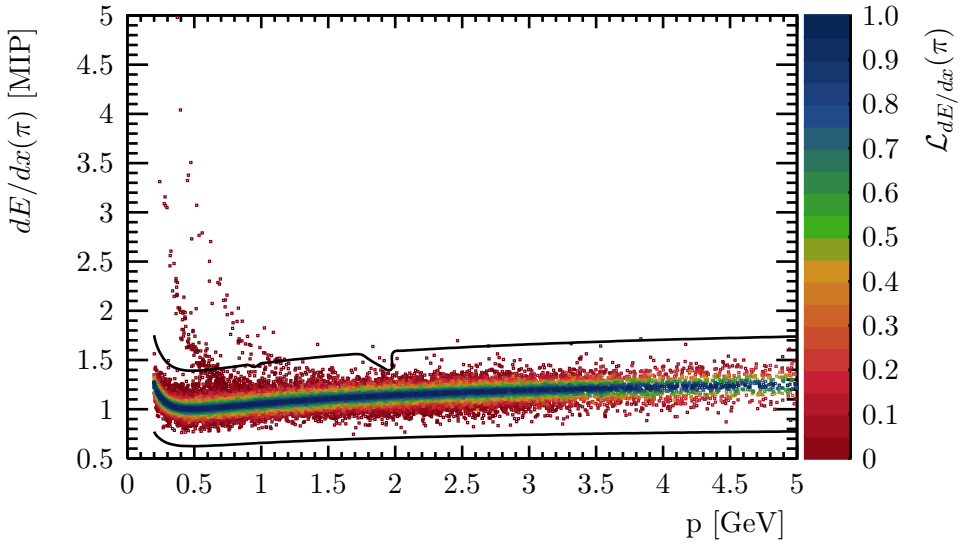

Figure 6.2.5: Scatter plot of the measured energy loss dE/dx versus track momentum for the selected tracks under the assumption that they are pions. The corresponding pion likelihood is encoded in the color of each point. The lines depict the dE/dx cuts described in Table 6.2.1.

To implement a dE/dx cut, a likelihood $\mathcal{L}_{dE/dx}(X)$ to obtain the measured dE/dx from a particle of species X is calculated for each track assuming various particle hypotheses. Events are then rejected or accepted depending on that likelihood value according to the limits defined in Table 6.2.1.

Table 6.2.1: Cuts on the dE/dx-likelihood for the various particle species and the momentum ranges they are applied in.

particle type X	pion	kaon	proton	deuteron
$\mathcal{L}_{dE/dx}(X)$ requirement	$> 10^{-3}$	< 0.1	< 0.1	< 0.1
valid p range [GeV]	-	0.0 - 0.5	0.0 - 1.0	0.0 - 2.0

Additional Cuts

Some additional selection cuts are applied specifically reduce the following kinds of background:

- **φ mesons:** If the kaons from the decay $\varphi \to K^+K^-$ are misidentified as pions, the invariant mass of the system is shifted from the region around $m_\varphi = 1020\,\text{MeV}$ towards $m_{\pi^+\pi^-} \gtrsim 280\,\text{MeV}$. This can lead to a significant background to ρ^0 production below the peak-mass $m_\rho = 775\,\text{MeV}$. To suppress such events, the two selected pion candidates are reconstructed under a kaon hypothesis. If then the dE/dx-likelihood exceeds 1% for both tracks, i.e., $\mathcal{L}_{dE/dx}(K) > 0.01$, and the invariant K^+K^- candidates' mass lies within 15 MeV of the φ-mass, the event is rejected.
- **K^0 mesons:** Events containing a K^0-decay found by the H1 K^0 finder [115] algorithm are rejected.
- **Cosmic muons:** Events due to a cosmic muon traversing the detector are rejected following the prescription by Huber [116, Section 6.6.2].

A summary of the selection cuts is given in Appendix B in Table B.1.

6.3 Kinematic Distributions

The data sample obtained from the described selection contains 17284 events. As a means of verifying that it is indeed a good $e\,p \to e\,\rho^0(\pi^+\pi^-)\,p$ sample, the kinematic distributions can be compared to MC expectations. As a reference MC the combined proton elastic and dissociative DIS ρ^0 sample described in Section 5.1.2 is used, which underwent the same selection steps as the data sample.

Table 6.3.1: Cuts on event variables defining the signal region.

lower cut		variable		upper cut
0.6 GeV	$<$	$m_{\pi^+\pi^-}$	$<$	1.1 GeV
$2.5\,\text{GeV}^2$	$<$	Q^2		
$-1\,\text{GeV}^2$	$<$	t		
35 GeV	$<$	$W_{\gamma p}$	$<$	180 GeV

Event Variables and Signal Region

First, the event variables $m_{\pi^+\pi^-}$, t, Q^2, and $W_{\gamma p}$ are presented and a signal region is defined, where an agreement between data an MC should be expected. The

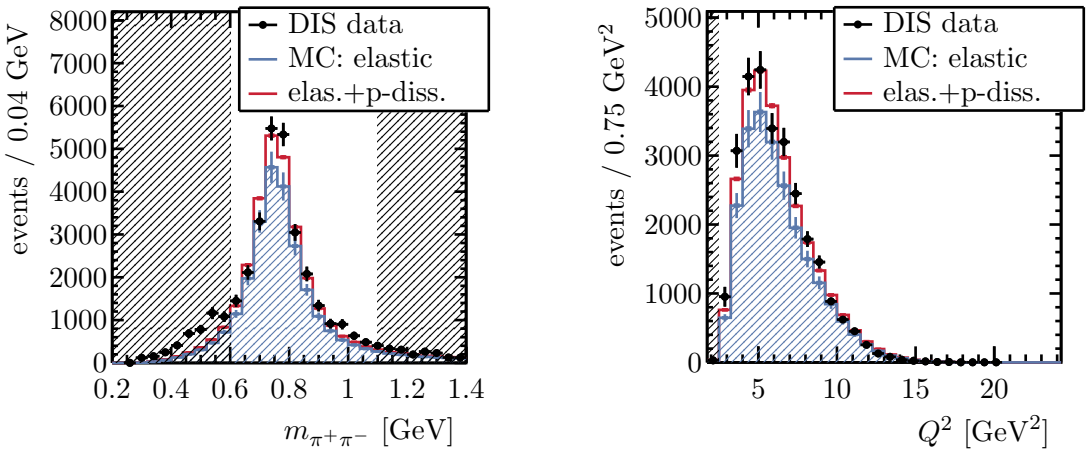

Figure 6.3.1: Distribution of the $\pi^+\pi^-$ mass (left) and Q^2 (right) for events in the signal region for data and MC. The shaded regions illustrate the cuts on $m_{\pi^+\pi^-}$ and Q^2 as defined in Table 6.3.1. The uncertainties of the MC samples represent statistical and a systematic contribution due to the scaling uncertainty (see Section 5.1.2), but the statistical uncertainties are negligible.

corresponding cuts on the event variables are listed in Table 6.3.1.

Figure 6.3.1 shows the invariant mass distribution of the $\pi^+\pi^-$ system. The data sample is clearly dominated by the ρ^0 resonance with a mass of 775 MeV. A cut $m_{\pi^+\pi^-} > 0.6\,\text{GeV}$ is implemented to reject wrongly or incompletely reconstructed events, which are typically mirrored to the threshold mass $m_{\pi^+\pi^-} = 2m_\pi$. These backgrounds have been studied in other H1 DIS ρ^0 analyses [40] and were found to have significant contributions from the following processes

- $\rho' \to \pi^+\pi^-\pi^0\pi^0$
- $\omega \to \pi^+\pi^-\pi^0$
- $\varphi \to \pi^+\pi^-\pi^0$ or $\varphi \to K^+K^-$

where either the neutral pions escape detection or the kaons are misidentified as pions. A second cut at $m_{\pi^+\pi^-} = 1.1\,\text{GeV}$ is implemented to restrict the study to the ρ^0 mass peak.

Also shown in Figure 6.3.1 is the distribution of the photon virtuality Q^2. The rise of the number of events at with Q^2 at low Q^2 is due to the SpaCal acceptance and motivates a cut at $Q^2 \geq 2.5\,\text{GeV}^2$. At large photon virtualities the sample dies out because of the cut on the maximum electron radius discussed in Section 6.2.

Figure 6.3.2 shows the distribution of the proton momentum transfer t. A cut is placed such that events with $t < -1\,\text{GeV}^2$ are rejected. This suppresses both proton-dissociative events as well as the previously discussed backgrounds, which

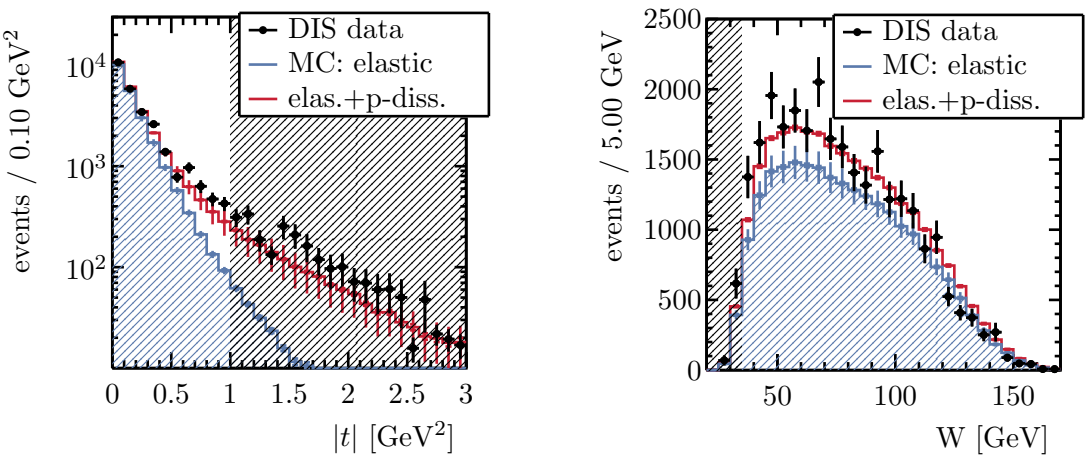

Figure 6.3.2: Distribution of t (left) and $W_{\gamma p}$ (right) for events in the signal region in the data and MC samples. The shaded regions illustrate the cuts on t and $W_{\gamma p}$ as defined in Table 6.3.1.

are predominantly found at large $|t|$ [40]. The photon-proton center of mass energy $W_{\gamma p}$ is depicted in Figure 6.3.2, as well. The lower edge of the distribution is due to the acceptance of the central tracker and events with $W_{\gamma p} < 35\,\text{GeV}$ are rejected.

Comparing the data to the MC sample overall a good agreement is found. From this study it can be concluded that the data sample does not contain any statistically relevant background processes in the signal region. Consequently, it can be assumed to consist mainly of elastic $e\,p \rightarrow e\,\rho^0(\pi^+\pi^-)\,p$ events, as well as a small proton dissociative contribution.

Track Kinematics

To further verify the MC sample, the distributions of the scattered electron and pion track quantities are studied. In Figure 6.3.3 the distribution of the energy $E_{e'}$, polar angle $\theta_{e'}$ and azimuthal angle $\varphi_{e'}$ of the scattered electron are shown. The structures in the $\varphi_{e'}$ distribution are a direct consequence of the fiducial SpaCal selection cuts introduced in Section 6.2.

In the following, the distributions of the pion candidate kinematics are presented in figures having the following structure: Each figure contains the respective distribution of the positively charged π^+ candidates in the left and of the negatively charged π^- candidate in the middle column. In addition, the bin-wise asymmetry between the two distributions is shown in the right column to explicitly study whether there are any charge asymmetries present in the reference sample. The

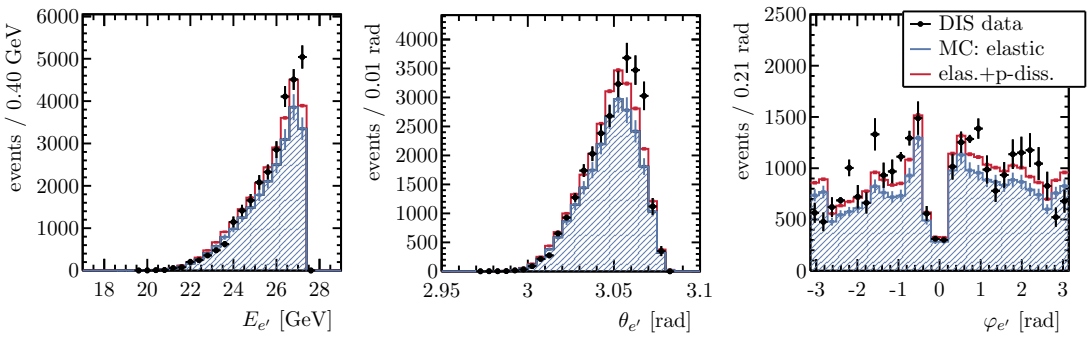

Figure 6.3.3: Distribution of the reconstructed energy $E_{e'}$ (left), polar angle $\theta_{e'}$ (center) and azimuthal angle $\varphi_{e'}$ (right) of the scattered electron in the signal region. The structure in the $\varphi_{e'}$ distribution is a direct consequence of the fiducial SpaCal selection cuts discussed in Section 6.2.

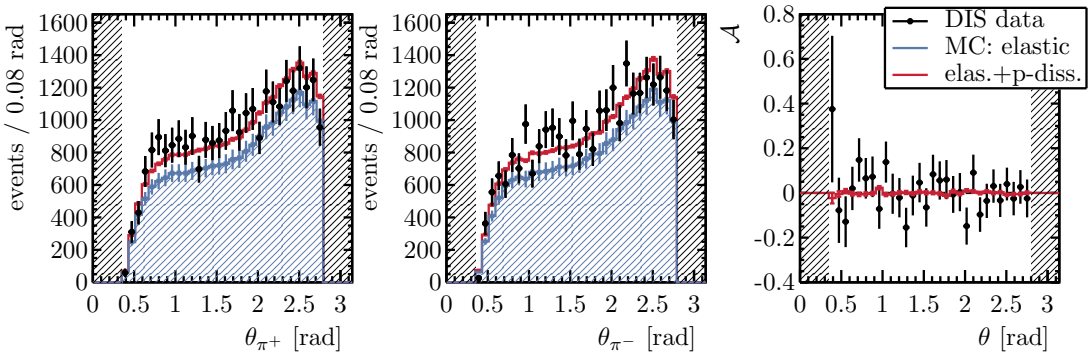

Figure 6.3.4: Distributions of the polar angle θ for the positive (left) and negative (middle) pion candidate, respectively. Only events from the signal region defined in Table 6.3.1 are considered. The asymmetry distribution is shown on the right.

asymmetry is defined as:

$$\mathcal{A}(X) = \frac{X_{\pi^+} - X_{\pi^-}}{X_{\pi^+} + X_{\pi^-}}, \tag{6.3.1}$$

where X_{π^+} and X_{π^-} denote the distribution of any variable X for positive and negative tracks, respectively.

The θ distributions are shown Figure 6.3.4 and exhibit a good agreement between data and MC. Also, there are no apparent differences between the charges. The CJC acceptance cuts discussed in Section 6.2 are marked in the plots by shaded bands. The φ distributions are shown in Figure 6.3.5. The structures in the distributions can be explained by a correlation between the azimuthal angles of the pions and of the scattered electron, which are connected via the conservation of the total transverse momentum. As a consequence of this correlation, the

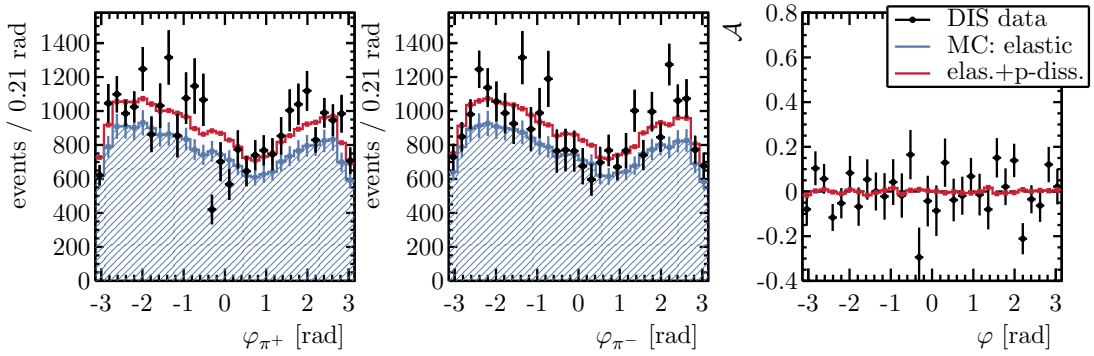

Figure 6.3.5: Distributions of the azimuthal angle φ for the positive (left) and negative (middle) pion candidate, respectively. Only events from the signal region defined in Table 6.3.1 are considered. The asymmetry distribution is shown on the right.

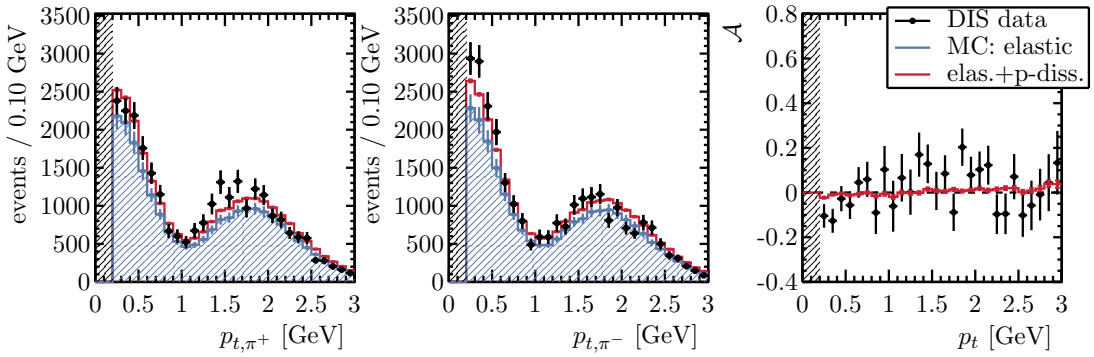

Figure 6.3.6: Distributions of the transverse momentum p_t for the positive (left) and negative (middle) pion candidate, respectively. Only events from the signal region defined in Table 6.3.1 are considered. The asymmetry distribution is shown on the right.

structures in the $\varphi_{e'}$ distribution that were explained earlier are reflected in the φ distributions of the pion candidates.

The pions' p_t distributions are shown in Figure 6.3.6. Their shape is rather peculiar and non-trivial and deserves some explanation. The two peaks in the distributions are a consequence of the angular decay structure of the ρ^0 meson, on the one hand, and the boost of the dipion system in the transverse plane, on the other. An analysis of the angular decay structure of the ρ^0 meson in DIS $e\,p \to e\,\rho^0(\pi^+\pi^-)\,p$ events, as performed for example by Clerbaux [111, Chapter 7], yields that the pion momenta in the ρ^0 of center of mass frame are preferably (anti-) parallel to the ρ^0 flight direction in the lab frame. If in the lab frame the ρ^0 carries transverse momentum, the transverse momentum of the one pion in the lab frame will then preferably be larger than the transverse momentum of the other. Now,

assuming $|t| \ll 1\,\text{GeV}$ and considering that the total transverse momentum of the initial ep state is zero, the contributions from the scattered electron and the $\pi^+\pi^-$ system to the total transverse momentum have to cancel each other in order to fulfill momentum conservation. The p_t of the electron is of the order of $\sqrt{Q^2}$ and consequently so is the p_t of the dipion system. As was seen previously, the Q^2 distribution peaks at about $5\,\text{GeV}^2$ such that the p_t distribution of the dipion system has to peak at about $\sqrt{5}\,\text{GeV}$. Putting all these things together, results in the observed structure in the pion p_t distributions. As it is important for the discussions to follow in Chapter 7, the correlation between the transverse momenta of the pions is explicitly shown in Figure 6.3.7 (left).

As second important consequence of the transverse momentum of the dipion system concerns the opening angle between the pion tracks. The larger the p_t of the $\pi^+\pi^-$ system, the closer the pions are together in the transverse plane. The distribution of the opening angle between the pions $\Delta\varphi = \varphi_{\pi^+} - \varphi_{\pi^-}$ is shown in Figure 6.3.7 (right).

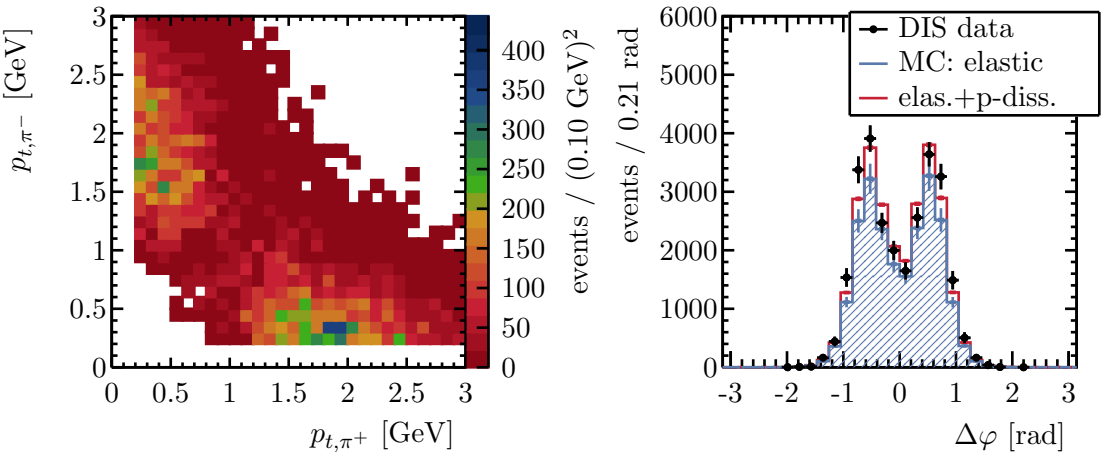

Figure 6.3.7: The correlation of the pions' transverse momenta (left) and the distribution of the opening angle between the pion tracks in the transverse plane (right). Only events from the signal region are considered. The left plot is shown for data only, but the MC sample exhibits the same features.

Summarizing, overall there is a good agreement among the data and the MC sample, both in the event and the track variables. It can thus be concluded that the event selection is appropriate for an $e\,p \to e\,\rho^0(\pi^+\pi^-)\,p$ sample. Complementary, the agreement also shows that the detector simulation works well, because so far all features caused by detector effects are correctly described by the MC sample.

7 FTT Studies in DIS

For a measurement of charge asymmetries in $\pi^+\pi^-$ photoproduction, detector systematics have to be understood. In this matter, the Fast Track Trigger that is used to trigger $\pi^+\pi^-$ photoproduction events at H1 is a potentially critical component because of various reasons: First of all, there a is geometric asymmetry inherent to the CJC (see Section 4.2.1) which might cause charge asymmetries in the CJC-based FTT. Negative low p_t tracks are bent by the magnetic field in opposite direction to the tilt of the CJC cells while positive tracks are bent in the same direction. As a consequence, on the one hand negative tracks have a different orientation with respect to the CJC sens wire planes than positive tracks, and on the other they also cross a different number of sense wire planes. An illustration is given in Figure 7.0.1.

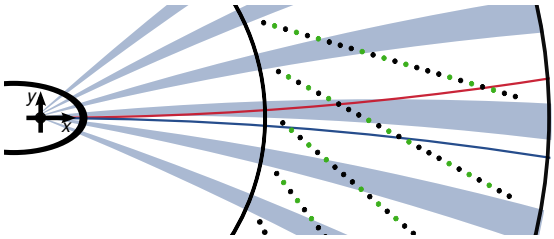

Figure 7.0.1: Sketch of the CJC1 with the FTT trigger wires marked in green. The blue and red line represent a positive and negative track with a transverse momentum of 1 GeV, respectively. Independent of the azimuthal angle, all negative tracks cross two sense wire planes. A large fraction of positive tracks, on the other hand, only crosses a single wire plane as indicated by the shaded blue regions.

Secondly, large differences in the nuclear cross sections for positive and negative pions at low p_t [17], are known to cause charge asymmetries in the offline H1 tracking efficiency [117] and thus are expected to affect the FTT, as well. The pion-proton cross section is shown in Figure 7.0.2 as a function of the pion momenta and for protons at rest.

Given this motivation, in the present chapter the FTT performance is studied with a focus on charge asymmetries. The studies are performed using the DIS $\rho^0 \to \pi^+\pi^-$ sample presented in Chapter 6, which is obtained independently from

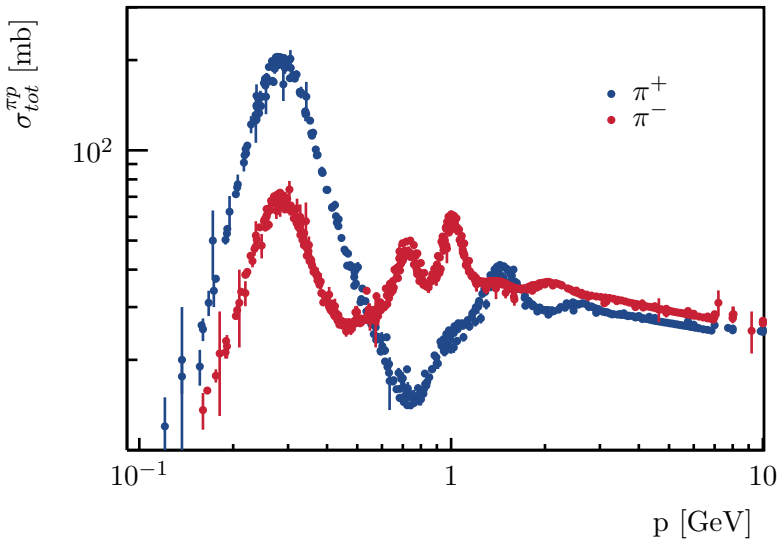

Figure 7.0.2: Total measured cross section for pion-proton interactions as a function of the pion momenta and for resting protons. Data provided by the PDG [17].

any track based information but provides an event topology similar to $\pi^+\pi^-$ photoproduction. Only events from the signal region defined in Section 6.3 are used. First, the general event structure in the FTT is investigated, then single track FTT efficiencies are studied and finally the efficiency of the dedicated ρ^0 photoproduction sub-trigger is measured.

7.1 FTT Event Characteristics

The FTT performance depends strongly on the number of tracks measured in the CJC. The track multiplicity distribution as measured by the FTT is shown in Figure 7.1.1 for the DIS sample. From the plot two important things should be noticed. First, although the fully reconstructed events are required to contain precisely two tracks, excluding in particular events with additional tracks of low quality, there are many events with fewer as well as more than two tracks in the FTT. The first case is simply due to the fact that the FTT is not fully efficient, which is discussed further in Section 7.2. The latter case is more peculiar and is studied in the following. The second observation is the large discrepancy between the data and MC sample. Both discrepancies need to be understood better, because the ρ^0 photoproduction trigger contains explicit FTT track multiplicity vetoes. In order to get a good description of the data, the MC needs to be corrected.

To find out where the additional FTT tracks originate from, correlations between

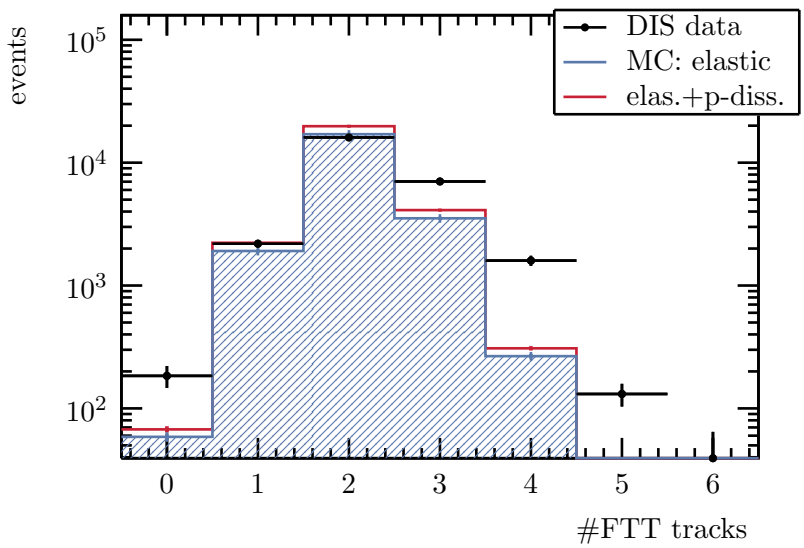

Figure 7.1.1: FTT track multiplicity distribution in the signal region of the DIS ρ^0 samples.

them and the reconstructed tracks can be studied. For this a measure for the geometrical distance between a reconstructed and an FTT track in the transverse plane is introduced:

$$\Delta\tilde{\varphi} = \tilde{\varphi}_{rec} - \tilde{\varphi}_{unassigned\ FTT}, \tag{7.1.1}$$

where $\tilde{\varphi}$ is the geometric angle of a track at $r = 22\,\text{cm}$ (see also Section 4.3.2) which provides the best azimuthal resolution. In the following, a distinction between FTT tracks that are assigned to a reconstructed as described in Section 4.3.2 and unassigned FTT tracks is made.

In Figure 7.1.2 (left) the distance $\Delta\tilde{\varphi}$ between the unassigned FTT tracks and the negative pion candidates is plotted against the distance to the positive pion candidates. The distribution shows, that additional FTT tracks are always created in the vicinity of at least one real track with a distance compatible with the FTT resolution. Beyond this, it does not clearly indicate whether the second, farther track has any influence. To study this influence, the average number of additional FTT tracks per event is plotted as function of the distance in $\tilde{\varphi}$ between the two reconstructed tracks in Figure 7.1.2 (right). It can be seen, that there is indeed a higher probability to create additional FTT tracks when the reconstructed tracks are close together, as indicated by the peak at zero. There are no additional tracks above an absolute distance of ~ 2. This is simply due to the fact that there are no events with larger opening angles between the pions, compare Figure 6.3.7. In the MC, the number of unassigned FTT tracks is smaller by a factor of approximately 2, confirming the previously observed discrepancy in the FTT track multiplicity.

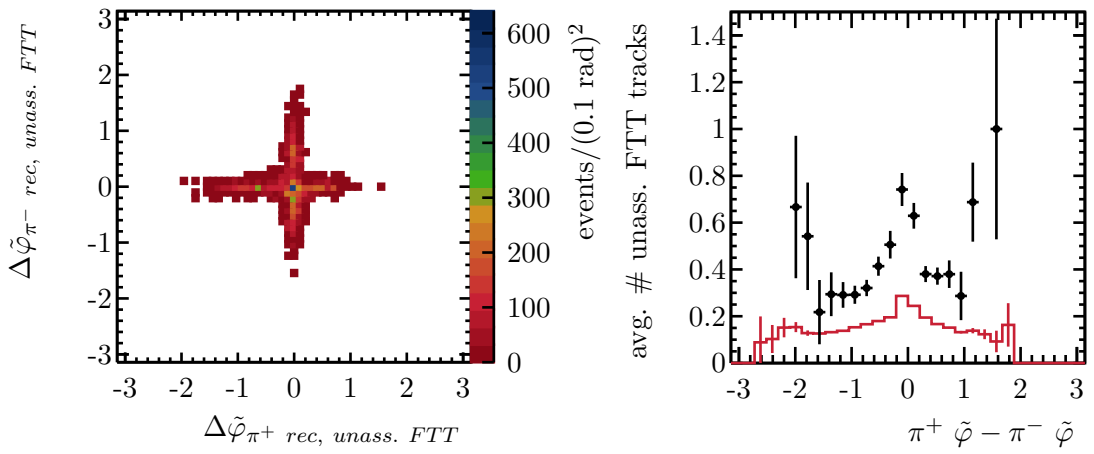

Figure 7.1.2: Left: Distance in $\tilde{\varphi}$ between the unassigned FTT tracks and the reconstructed pion candidates in the data sample. Right: Average number of unassigned FTT tracks as a function of the azimuthal distance $\tilde{\varphi}$ of the two pions for the data (black) and the MC (red) DIS sample.

In conclusion, ambiguous FTT signals lead to more tracks being observed in the FTT than are truly present in the CJC. While this happens for isolated tracks, it is significantly more likely if two real tracks are close together. The additional FTT tracks are always close to a real track, i.e., have a similar angle $\tilde{\varphi}$ but can have substantially different inverse transverse momenta $1/p_t$. The latter is not shown explicitly in a plot here, but can be learned from comparing the $1/p_t$ of FTT tracks close in $\tilde{\varphi}$. In the idealized detector simulation there are fewer effects favoring such ambiguities. In particular, the CJC geometry and the drift velocity of the charge carriers is ideal in the simulation, and there is less noise. As a consequence, double counting of tracks happens less often in the MC than in the data sample.

FTT Multiplicity Correction

Before proceeding, the discrepancy in the FTT multiplicity between the data and the MC sample needs to be resolved. In particular, for measuring and comparing the ρ^0 photoproduction trigger efficiency in data and MC in Section 7.3 this is essential, because the trigger contains explicit FTT multiplicity vetoes. A simple way to correct the MC sample such that it gives efficiencies in good agreement with those measured in data, was found in reweighting the MC in the FTT track multiplicity distribution.

The following simplified picture can be used to find a parametrization for the FTT track multiplicity. First, there are two true, reconstructed tracks in each event which can create up to $n^{rec}_{FTT} \leq 2$ FTT tracks. For this to happen a

binomial probability[1] $\mathcal{B}(p_{rec}, 2;\ n^{rec}_{FTT})$ is assumed, where the probability p_{rec} corresponds to the FTT single track efficiency. Each reconstructed track observed by the FTT can cause up to N_{add} additional FTT tracks. For the creation of $n^{add}_{FTT} \leq n^{rec}_{FTT} \cdot N_{add}$ additional FTT tracks a binomial probability distribution, $\mathcal{B}(p_{add}, n^{rec}_{FTT} \cdot N_{add};\ n^{add}_{FTT}$, is assumed with a probability parameter p_{add}.

Put together, the FTT track multiplicity distribution is parametrized by

$$\mathcal{N}(N,\, p_{rec},\, p_{add},\, N_{add};\, n) = N \cdot \sum_{i=0}^{2} \mathcal{B}(p_{rec},\, 2;\, i)\, \mathcal{B}(p_{add},\, N_{add} \cdot i;\, n-i), \quad (7.1.2)$$

where N is a normalization factor, n is the total number of FTT tracks consisting of i tracks that can be assigned to reconstructed tracks and $n-i$ additional tracks.

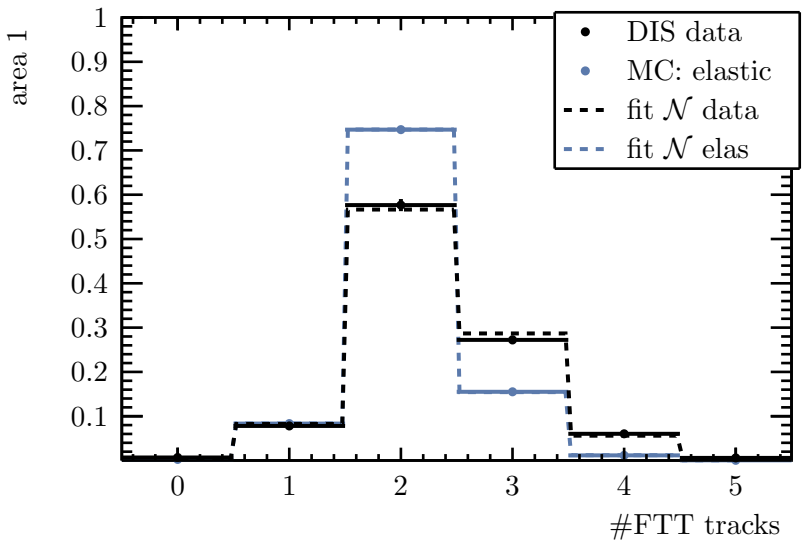

Figure 7.1.3: FTT track multiplicity distribution in data (black) and the elastic MC (blue). The lines represent a fit of the parametrization given in Equation (7.1.2). The proton dissociative MC is not shown, but the distribution there is equivalent to the elastic MC. The obtained fit parameters are summarized in Table 7.1.1.

In Figure 7.1.3 this parametrization is fitted to the FTT track multiplicity distribution of the data and the MC samples. It describes the distributions well for up to 5 FTT tracks. Events with higher multiplicities are sufficiently rare and can be safely neglected. The fit parameters are listed in Table 7.1.1. As expected, the parameter p_{rec} agrees well between data and MC, while p_{add} is much larger in

[1] $\mathcal{B}(p, N;\ k) = \binom{N}{k} p^k (1-p)^{N-k}$, where k is the number of successes in N trials where each success happens with a probability p.

data than it is in the simulation. N_{add} is not fitted but set to 2, which was found to work best.

Table 7.1.1: Parameters to reweight the MC in the FTT multiplicity distribution as obtained from the fit described in the text and shown in Figure 7.1.3.

fit parameter	data	MC
p_{rec}	0.942 ± 0.003	0.951 ± 0.0003
p_{add}	0.116 ± 0.003	0.050 ± 0.0003
N_{add}	2 (fixed)	2 (fixed)

The MC sample is reweighted by applying a multiplicity dependent weight $w(n)$ defined as:

$$w(n) = \frac{\mathcal{N}(1,\, p_{rec}^{data},\, p_{add}^{data},\, 2;\, n) \,/\, \sum_n \mathcal{N}(1,\, p_{rec}^{data},\, p_{add}^{data},\, 2;\, n)}{\mathcal{N}(1,\, p_{rec}^{MC},\, p_{add}^{MC},\, 2;\, n) \,/\, \sum_n \mathcal{N}(1,\, p_{rec}^{MC},\, p_{add}^{MC},\, 2;\, n)}. \tag{7.1.3}$$

To estimate an uncertainty on this correction, the reweighting is performed two additional times with parameters varied in the following manner: First, p_{rec}^{data} is shifted up and simultaneously p_{add}^{data} is shifted down by the corresponding fit uncertainties listed in Table 7.1.1. Secondly, the directions of the variations are inverted. This is motivated by the observation that a larger p_{rec}^{data} and a smaller p_{add}^{data} lead to an increased ρ^0 trigger efficiency in the corrected MC, while a smaller p_{rec}^{data} and a larger p_{add}^{data} have the opposite effect. In the plots shown in the following for the reweighted MC, the variation caused by modifying the parameters as described is included as a systematic uncertainty for the reweighted MC.

The reweighted MC sample has to be treated with precaution. While the purpose of the weight is to correct for an insufficient FTT simulation, it affects the sample as a whole. This is due to the number of FTT tracks depending in particular on the kinematic properties of the pion tracks (see below). So by modifying the FTT multiplicity distribution, also the kinematic distributions are altered. If they are correctly described in the original MC, as was concluded in Section 6.3, they become wrong when the weight is applied. However, within the context of this thesis the distortions of the kinematic distributions caused by the reweighting, while wrong in principle turn out to be rather small in practice so that given the limited data sample size they are mostly negligible within statistical uncertainties. Moreover, to further avoid problems, the reweighted MC is only used to measure FTT related quantities, where the applied procedure turns out to be quite successful.

7.2 FTT Single Track Efficiencies

Associating reconstructed tracks to tracks seen by the FTT (see Section 4.3.2) allows to define a FTT single track efficiency:

$$\epsilon_{trk}^{\pm} = \frac{N_{ass.\ FTT}}{N_{rec}^{\pm}}, \tag{7.2.1}$$

where $N_{rec}^{\pm}$ is the number of reconstructed tracks from either positively or negatively charged particles and $N_{ass.}$ is the fraction of these tracks that has an assigned track in the FTT. In the following the single track efficiency is studied as a function of the track kinematics. To compare the efficiency for positive and negative tracks, an efficiency asymmetry[2] is introduced as

$$\mathcal{A}_{\epsilon} = \frac{\epsilon_{trk}^{+} - \epsilon_{trk}^{-}}{\epsilon_{trk}^{+} + \epsilon_{trk}^{-}}. \tag{7.2.2}$$

In Figure 7.2.1 the FTT single track efficiency for positive and negative pion candidates is shown as a function of the azimuthal angle φ. Naïvely, one would expect the efficiency to not depend on φ because of the cylindrical symmetry of the CJCs. However, in the plots a significant drop can be observed at low φ. This is a consequence of several dead or inefficient wires in the CJC2, which are all known [117] and considered in the detector simulation. In particular, the regions give rise to a charge asymmetry in the φ dependence of the efficiency. This is due to strongly bent, low p_t tracks which cross the inefficient regions for different azimuthal angles depending on their charge, as is illustrated in Figure 7.2.2 (left).

Apart from the inefficient zone, the track efficiency is still not constant in φ, which can be observed in particular in the MC: at large φ the efficiency drops down for positive and rises for negative tracks. This is a consequence of a slight offset of the true beam axis off the CJC symmetry axis. This offset was not considered at the generation of the FTT track patterns and thus causes incompatibilities between the hit patterns created by the event tracks and the predefined patterns.

[2] In the following, efficiency uncertainties are calculated taking a Bayesian approach. This is implemented with the Root `TGraphAsymmErrors::Divide` method. See ROOT Reference Guide [118] for details. This approach gives asymmetric uncertainties on efficiencies. The uncertainty of the efficiency asymmetries is then calculated using the following modification of Gaussian error propagation:

$$\Delta(A_{\epsilon})^{up/down} = \frac{1}{(\epsilon_1 + \epsilon_2)^2} \sqrt{\left(2\,\epsilon_2\,\Delta\epsilon_1^{up/down}\right)^2 + \left(2\,\epsilon_1\,\Delta\epsilon_2^{down/up}\right)^2}$$

Furthermore, the previously used systematic uncertainty of the normalization of the MC sample is negligible and not included in total efficiency uncertainty, which then only contains a contribution from the statistical uncertainty and from the uncertainty due to the reweighting of the MC FTT multiplicity distribution.

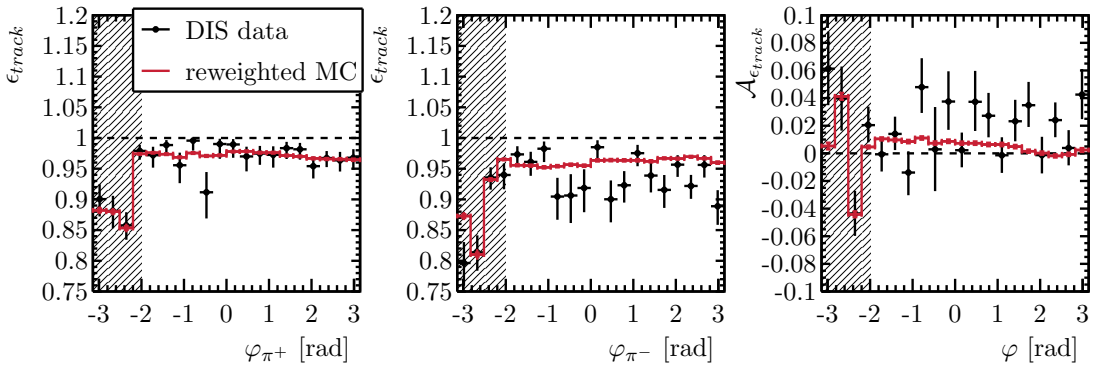

Figure 7.2.1: Track efficiency for positive (left) and negative tracks (middle), and the efficiency asymmetry (right) as a function of the azimuthal angle of the pions. Data is shown in black, the combined elastic and proton dissociative MC in red. The shaded area marks an inefficient region in φ which is excluded in the following.

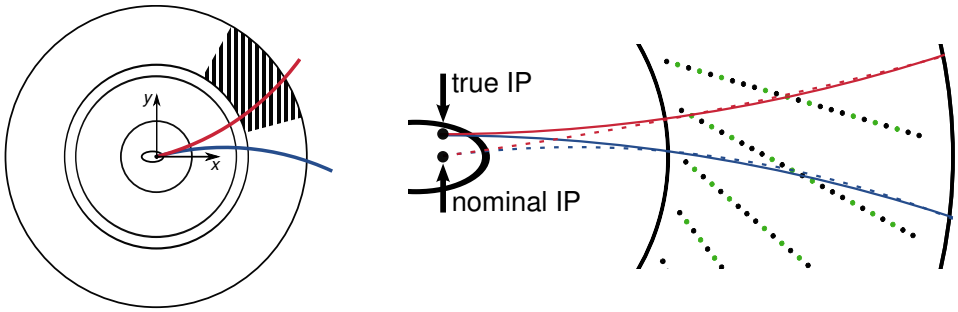

Figure 7.2.2: Left: Inefficient CJC region during the run period 2006/2007. A negative, low p_t track (red), may traverse this region while a positive track with the same p_t and φ (blue) may miss it. Right: Consequence of a vertex offset. As the offset is not considered in the FTT, negative, low p_t tracks (continuous red) perpendicular to the offset appear to be of larger p_t to the FTT (dashed red), while positive tracks (continuous blue) appear to be of smaller p_t (dashed blue). For tracks going in opposite direction the effect is reversed, while tracks going in the direction of the offset are barely affected at all.

As illustrated in Figure 7.2.2, depending on their charge and angle φ tracks are affected differently by the offset. First of all, tracks are affected most if they are perpendicular to the direction of the offset. Secondly, the hit patterns created in the FTT by the illustrated tracks appear to correspond to tracks coming from the vertex and having higher p_t in case of the negative track and lower p_t in case of the positive track. For tracks going in the opposite direction the situation is reversed. Altogether, this gives rise to a charge and φ dependence of the efficiency. This

dependence should be periodic in φ, which however is hidden by the inefficient CJC2 regions. Furthermore, it should be antisymmetric for positive and negative tracks, which in turn is hidden by an overall asymmetry in the track efficiency, which is studied further down in the text.

Table 7.2.1: FTT track efficiencies for positively and negatively charged tracks in data and MC in the efficient region $-2\,\text{rad} < \varphi < 3.14\,\text{rad}$.

	data (stat.)	FTT multiplicity reweighted MC (stat.)	algorithm uncertainty (data & MC)	FTT multiplicity weight uncertainty (MC)
ϵ^+_{trk} [%]	$97.2^{+0.4}_{-0.5}$	$97.18^{+0.04}_{-0.04}$	$+0.1$	± 0.1
ϵ^-_{trk} [%]	$94.0^{+0.6}_{-0.6}$	$96.09^{+0.04}_{-0.04}$	$+0.2$	± 0.2
$\frac{\epsilon^+_{trk} - \epsilon^-_{trk}}{\epsilon^+_{trk} + \epsilon^-_{trk}}$	$0.017^{+0.004}_{-0.004}$	$0.0056^{+0.0003}_{-0.0003}$	-0.0003	∓ 0.0003

To study further effects independently of the dead CJC wires, in the following only tracks with $-2\,\text{rad} < \varphi < 3.14\,\text{rad}$. are considered. The FTT single track efficiency values for this region are summarized in Table 7.2.1. Two things should be noted: First, there is an already mentioned difference between the efficiency for positive and negative tracks, whose origin is discussed below. Then, there is a significant difference between ϵ^-_{trk} measured in data and the MC. This difference is probably a consequence of idealized CJC conditions used for the generation of the FTT track patterns as well as for the MC simulation. An idealized CJC geometry is used there, and the gas conditions, affecting in particular the charge carrier drift velocity, are assumed to be ideal and constant. The true CJC geometry, however, is imperfect and the gas conditions change constantly. This causes inconsistencies between the generated FTT hit patterns and those created by a true track and results in a lower efficiency in data. Due to the geometry of the CJC, positive tracks are affected differently than negative tracks. For example, as illustrated in Figure 7.0.1 negative tracks cross the CJC wire planes more often than positive tracks. And is illustrated in Figure 7.2.3 a variation of the charge carrier drift velocity affects tracks crossing the wire planes more than parallel tracks. This might explain, why ϵ^-_{trk}, but not ϵ^+_{trk}, is significantly smaller in data than in the MC.

Three sources for systematic uncertainties are studied. First, the normalization of the MC sample, i.e., in particular the fraction of elastic and proton dissociative events, does not affect the FTT single track efficiency at all. Secondly, the algorithm used for the assignment of FTT tracks to reconstructed tracks as described in Section 4.3.2 gives rise to uncertainties as listed in Table 7.2.1.

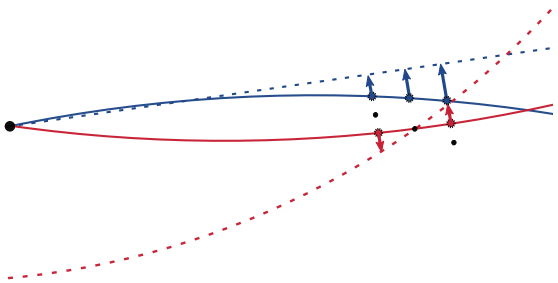

Figure 7.2.3: Consequences of a variation of the charge carrier drift velocity. If the drift velocity is smaller than was assumed for the generation of FTT hit patterns, the hit patterns caused by the true tracks (continuous lines) appear to be coming from tracks that are further from the sense wires (dashed lines). If the drift velocity is larger, the tracks appear to be closer. The distortions such variations cause are larger for tracks crossing the CJC wire planes (red) than for parallel tracks (blue).

These uncertainties are estimated by increasing the acceptable distance between compatible FTT and reconstructed tracks (compare Equation (4.3.4)) to 7.5. Increasing it further, results in an overestimation of the efficiency because of the previously observed doubling of tracks. Lowering it, on the other hand, results in an underestimation because of the limited p_t and φ resolution of the FTT. As the uncertainties arising from the the track assignment algorithm are fully correlated, they neither account for any differences between positive and negative tracks, nor for any differences between data and MC. Finally, reweighting the MC in the FTT multiplicity distribution gives rise to small systematic uncertainties in the MC values as listed in the table.

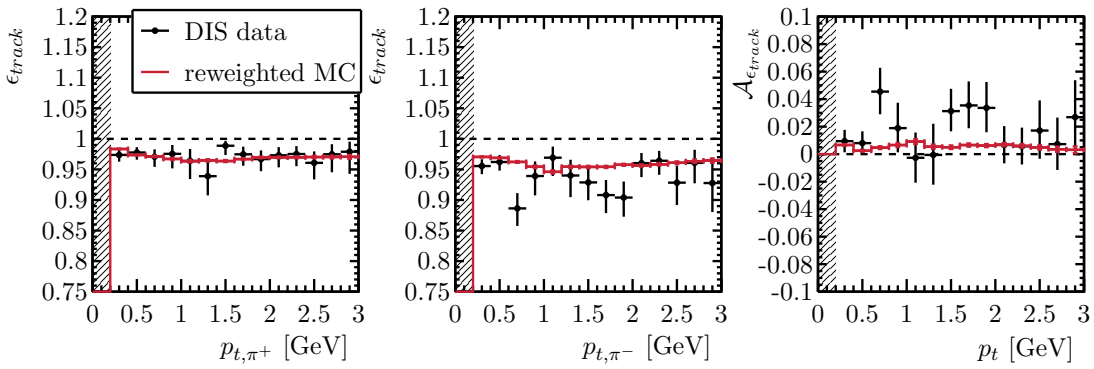

Figure 7.2.4: Track efficiency for positive (left) and negative tracks (middle), and the efficiency asymmetry (right) as a function of the transverse momentum of the pions. The shaded area marks the CJC acceptance in p_t, outside of which events are excluded.

To explain the difference in the FTT track efficiency between oppositely charged tracks, it is illustrative to study the efficiency as a function of the pions' transverse momenta as shown in Figure 7.2.4. For both charges the efficiency drops with increasing p_t until a minimum is reached at approximately 1 GeV. This is a consequence of a variation in the track length: strongly bent low p_t tracks traverse a larger gas volume in the CJC and thus ionize more charge carriers, i.e., leave a larger signal. The following rise in the efficiency with p_t is a consequence of the geometry of the CJC. More precisely, it is the reason the CJC was designed the way it was. The tilt of the CJC wire planes of 30° was chosen such (see Section 4.2.1), that the charge carriers drift perpendicular to straight high momentum tracks in the electromagnetic field. This leads to an ideal signal shape resulting in a better hit identification and consequently a higher track efficiency.

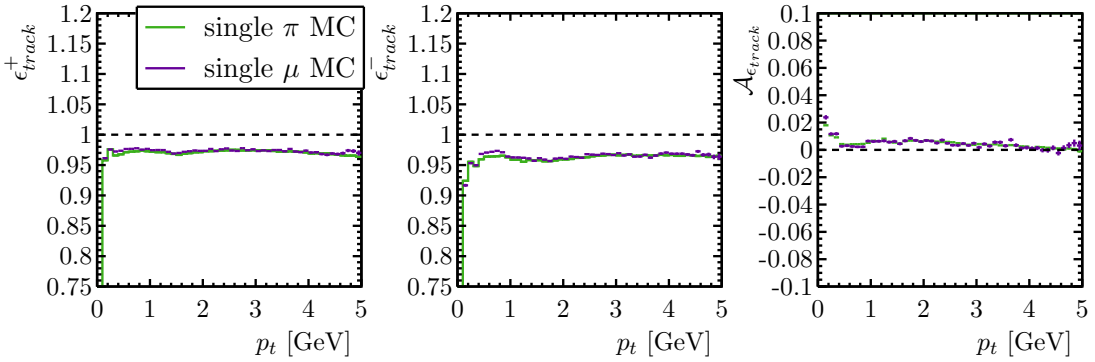

Figure 7.2.5: Track efficiency for positive (left) and negative tracks (middle), and the efficiency asymmetry (right) as a function of transverse momentum as measured in the single track pion and muon MC samples. The similarities between pions and muons, and the fact that asymmetry vanishes at $p_t \gtrsim 4\,\text{GeV}$ indicate a geometric origin. Nuclear effects cause small differences between pions and muons at small p_t only and are mostly negligible.

Looking at the asymmetry plot, again the discussed higher efficiency to detect positively charged tracks in the FTT can be observed. At the beginning of Chapter 7 two possible origins are discussed: The charge difference in the nuclear interaction cross section at low pion momenta, and the geometry of the CJC. As shown in Figure 7.0.2, large differences in the nuclear cross section can only be expected for $p_t \leq p \lesssim 1\,\text{GeV}$ but an asymmetry is still present at larger p_t. Also, the π^--proton cross section is not consistently larger than the π^+-proton cross section, which if the case would favor a larger efficiency for positive tracks. Consequently, the asymmetry presumably originates from a geometric effect. If this is indeed the case, it has to vanish for high p_t where tracks become straight and no difference in the geometry of positive and negative tracks remains. Unfortunately,

the DIS sample at hand does not provide sufficient statistics of particles with high momenta to check this.

To show the validity of the explanation nonetheless, a pure detector simulation is performed, in which the single track efficiency is measured using isolated tracks. In Figure 7.2.5 the single track efficiency is shown as a function of p_t as measured using the single track pion and muon MC samples introduced in Section 5.1.2. First of all, a comparison between pions and muons allows to completely rule out nuclear effects as the origin of the asymmetry. Nuclear effects do not play a role for muons and yet the same asymmetry as for pions is present there. Secondly, The fact the asymmetry vanishes for $p_t \gtrsim 4\,\mathrm{GeV}$ confirms a geometric origin.

To complete the picture, the single track FTT efficiency is shown as a function of the polar angles of the pion candidates in Figure 7.2.6. The most notable feature there is the drop of efficiencies in the central region at angles of about $\theta \sim 90°(1.5\,\mathrm{rad})$. This drop is a consequence of the track length variation with tracks perpendicular to the beam line traversing a smaller gas volume than tracks in forward or backward direction. As visible in the asymmetry plot, the increase in the efficiency with track length also partially compensates the discussed charge difference.

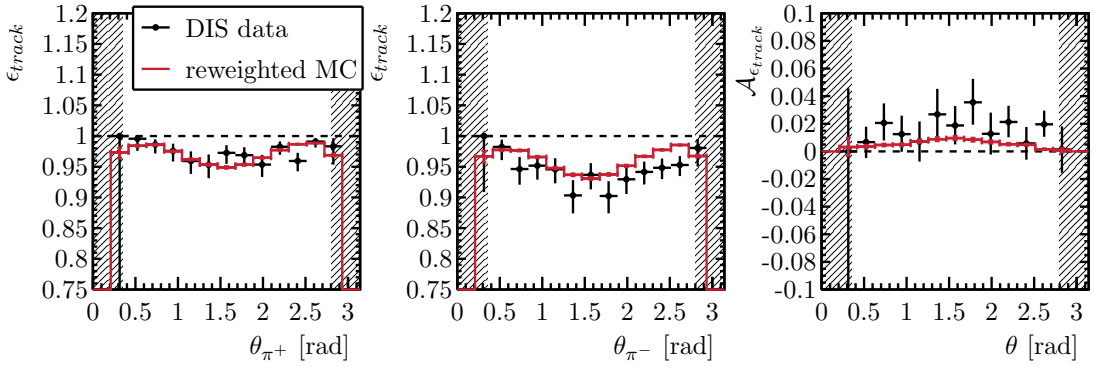

Figure 7.2.6: Track efficiency for positive (left) and negative tracks (middle), and the efficiency asymmetry (right) as a function of the polar angle of the pions. The shaded areas mark the CJC acceptance in θ.

Summarizing, most dependencies of the FTT single track efficiency on the kinematic properties and charge of the pion tracks can be understood. In particular the difference between positive and negative tracks can be explained as a feature of the CJC geometry affecting low p_t tracks. All features observed in the data sample are qualitatively also well described by the detector simulation. The track efficiency for negatively charge tracks is slightly overestimated in the MC, which might be a consequence of an idealized CJC used in the simulation.

7.3 s14 Trigger Efficiency

Studying FTT single track efficiencies has revealed insights into detector effects that cause oppositely charged tracks to be measured differently by the FTT. However, these effects do not necessarily cause charge asymmetries in a data sample obtained via FTT-based subtriggers, because these usually combine information from more than one track to form a trigger decision. Consequently, single track effects can either enhance or compensate each other. To investigate possible charge asymmetries introduced into a FTT-triggered $\pi^+\pi^-$ photoproduction sample, the efficiency of the corresponding subtrigger is studied in this section.

7.3.1 s14 Trigger Elements

At H1 the dedicated `s14` subtrigger was used to trigger $\pi^+\pi^-$ photoproduction events in the mass region of the ρ^0 resonance [18]. It relied purely on information from the central tracker, most importantly the Fast Track Trigger. The `s14` trigger decision was constructed in the following way:

```
s14:  FTT_mul_Tb>1 && FTT_mul_Ta<4 && FTT_chg_1 && (!LAr_IF) &&
      CIP_sig>2 && CIP_mul<6 v:5 t:0,
```

where ||, &&, and ! are the logical *or*, *and*, and *not* operators and the contributing trigger elements are explained below.

`FTT_mul_Tb>1:`	There have to be at least two reconstructed FTT tracks with a transverse momentum $p_t > 160\,\text{MeV}$.
`FTT_mul_Ta<4:`	There must not be more than three reconstructed FTT tracks with a transverse momentum $p_t > 100\,\text{MeV}$.
`FTT_chg_1:`	The sum of charges of all FTT tracks has to be between -1 and +1 in units of the elementary charge.
`!LAr_IF:`	Veto on activity in the LAr calorimeter above a noise threshold.
`CIP_sig>2:`	The CIP significance has to be larger than 2. See also Section 4.2.1.
`CIP_mul<6:`	The CIP multiplicity has to be less than 6. See also Section 4.2.1.
`v:5`	Standard vetoes against background due to beam-gas interactions.
`t:0`	The timing is taken from the CIP

An additional third FTT track, as well as a charge imbalance are allowed to explicitly account for track double counting in the FTT.

7.3.2 Trigger Efficiency

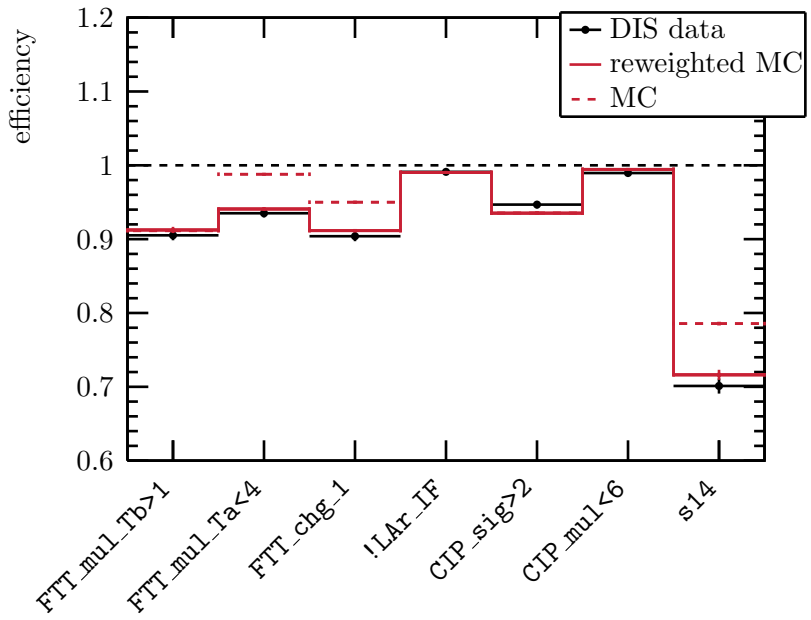

Figure 7.3.1: Efficiency of the s14 trigger elements and the full subtrigger for data and the combined elastic and proton dissociative MC before and after reweighting in the FTT multiplicity distribution. The efficiency is calculated for events in the signal region, as defined in Table 6.3.1 with the additional requirement $-2 < \varphi_{\pi^\pm}$ on the azimuthal angle of the pion tracks. The total uncertainty on the reweighted MC contains a statistical and a systematic contribution from the reweighting uncertainty.

The subtriggers used to select the DIS $\pi^+\pi^-$ sample do not rely on any of the trigger elements that constitute the s14 photoproduction trigger nor on any other central tracker based information. It can thus be used to measure trigger (element) efficiencies, i.e.:

$$\epsilon_X = \frac{N_X}{N_{ref}}. \tag{7.3.1}$$

Here X is a wildcard for any of the trigger elements (or the complete s14 subtrigger), N_X the number of events satisfying the corresponding requirement and N_{ref} the number of events in the reference sample.[3] As in the previous section, the efficiencies are measured excluding events with tracks in the inefficient CJC region $-3.14 < \varphi < -2$.

[3] Efficiency uncertainties are treated in the same way as for the single track efficiency calculations.

Table 7.3.1: Efficiency of the `s14` trigger elements and the full subtrigger for data and the combined elastic and proton dissociative MC after reweighting in the FTT track multiplicity distribution. The efficiency is calculated for events in the signal region, as defined in Table 6.3.1 with the additional requirement $-2 < \varphi_{\pi^\pm}$ on the azimuthal angle of the pion tracks.

trigger element	data ϵ_X [%] (stat.)	reweighted MC ϵ_X [%] (stat.)	weight uncertainty [%] (MC)
`FTT_mul_Tb>1`	$90.5^{+0.6}_{-0.7}$	$91.2^{+0.1}_{-0.1}$	± 0.4
`FTT_mul_Ta<4`	$93.5^{+0.5}_{-0.6}$	$94.1^{+0.05}_{-0.05}$	± 0.3
`FTT_chg_1`	$90.4^{+0.6}_{-0.7}$	$91.1^{+0.1}_{-0.1}$	± 0.1
`!LAr_IF`	$99.1^{+0.2}_{-0.2}$	$99.0^{+0.02}_{-0.02}$	± 0.0
`CIP_sig>2`	$94.7^{+0.5}_{-0.5}$	$93.5^{+0.05}_{-0.1}$	± 0.0
`CIP_mul<6`	$99.0^{+0.2}_{-0.2}$	$99.5^{+0.01}_{-0.02}$	± 0.0
`s14`	$70.1^{+1.0}_{-1.0}$	$71.6^{+0.1}_{-0.1}$	± 0.7

The overall efficiencies for the trigger elements, as well as for the full `s14` subtrigger are shown in Figure 7.3.1 and the corresponding values are listed in Table 7.3.1. In particular, the MC is shown before and after reweighting the FTT track multiplicity. It is apparent in the plot, that reweighting is necessary to bring data and the simulation in agreement. In the following, the efficiency is shown for the reweighted MC only.

7.3.3 Kinematic Dependencies

Event Variables

To further test the agreement between data and MC in DIS, the dependence of the `s14` subtrigger efficiency is studied as a function of kinematic variables.

The `s14` efficiency is is shown in Figure 7.3.2 as a function of the kinematic event variables $m_{\pi^+\pi^-}$, Q^2, $W_{\gamma p}$, and t. Overall, there is good agreement between data and the reweighted MC. The efficiency itself depends only little on the invariant dipion mass and the proton momentum transfer t but exhibits peculiar structures in the photon-proton center of mass energy $W_{\gamma p}$ and the photon virtuality Q^2, which deserve some comment. $W_{\gamma p}$ is directly correlated to the polar angle of the combined $\pi^+\pi^-$ system: for small $W_{\gamma p}$ the pions are boosted in forward direction and have a small polar angle. For large $W_{\gamma p}$, on the other hand, they

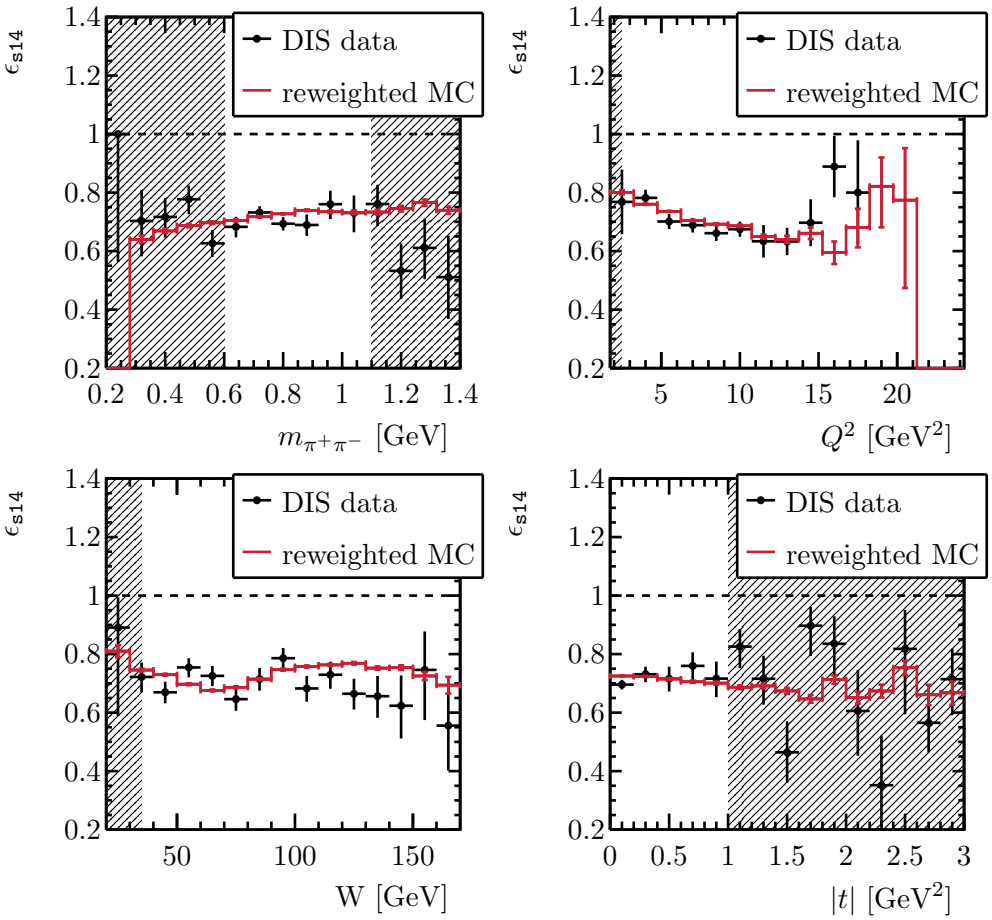

Figure 7.3.2: Kinematic dependence of the `s14` subtrigger efficiency on $m_{\pi^+\pi^-}$, Q^2, $W_{\gamma p}$, and t (from top left, clockwise). The gray bands mark the signal region introduced in Chapter 6.

are boosted in backward direction. The dip visible in the simulated `s14` efficiency at intermediate $W_{\gamma p}$ is then directly caused by the $\theta \sim 90°$ dip in the single track efficiency discussed in Section 7.2, which influences the trigger efficiency via the requirement to have at least two FTT tracks.

The Q^2 dependence of the efficiency is somewhat more difficult to explain. It is caused by the correlation between Q^2 and the transverse momentum of the $\pi^+\pi^-$ system discussed in Section 6.3. In particular, this causes the pions to be more collimated for larger Q^2. In the previous section it was shown that doubling of tracks in the FTT becomes more likely as the pion tracks get closer together. Via the `s14` FTT track multiplicity veto this results in a decline of the efficiency. To see this more explicitly, in Figure 7.3.3 the `s14` efficiency is shown as a function of the azimuthal distance in $\Delta\varphi$ between the reconstructed pion tracks. The drop of the efficiency with Q^2 is further aggravated by the relation between Q^2 and the

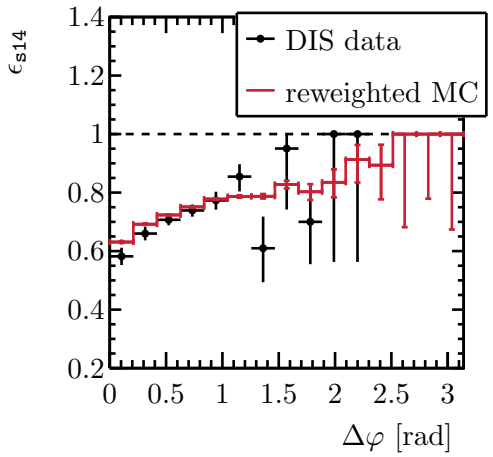

Figure 7.3.3: Dependence of the `s14` subtrigger efficiency on the azimuthal opening angle between the reconstructed pion tracks for data and the combined MC in DIS.

transverse momenta of the pion tracks. As discussed in Section 6.3 the transverse momenta of the pion tracks become larger with increasing Q^2. Further down in the text it is shown that for events with high p_t tracks the trigger efficiency suffers because the FTT has more and more difficulties measuring the correct charge of those.

Charge Asymmetries

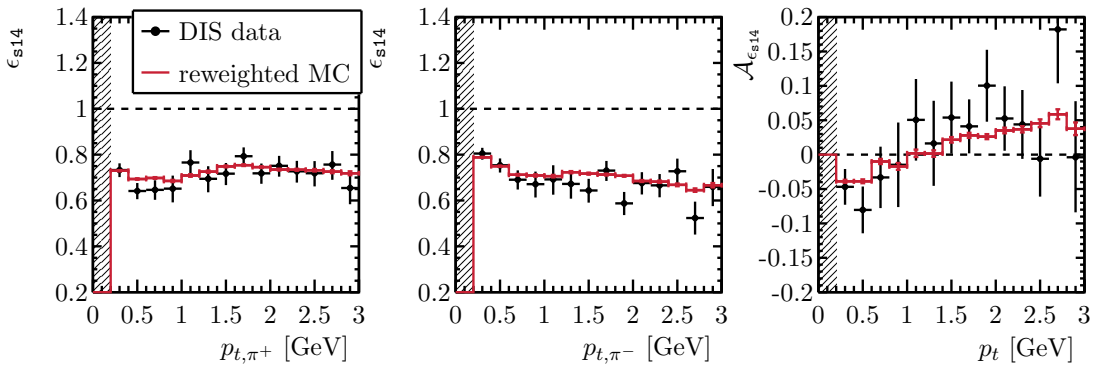

Figure 7.3.4: `s14` efficiency as a function of the pion candidates' p_t in the signal region for data and the combined elastic and proton-dissociative MC in DIS.

In this section, the question whether the `s14` subtrigger can give rise to charge asymmetries in a `s14` selected data sample shall finally be addressed. The

most interesting effect in this respect can be observed in the dependency of the s14 efficiency on the transverse momenta of the pion candidate tracks. The corresponding plot is shown in Figure 7.3.4. There a significant difference between the dependence on the momentum of the positive track and the momentum of the negative track is observed: while the efficiency is flat as a function of p_{t,π^+}, it drops down with p_{t,π^-}. To understand this behavior, several things need to be considered. First, and most important it is a consequence of the previously discussed anti-correlation of the pion tracks' transverse momenta in DIS (compare Figure 6.3.7), which links low p_t ($p_t \lesssim 1\,\text{GeV}$) negative to high p_t ($p_t \gtrsim 1\,\text{GeV}$) positive tracks and vice versa. As a consequence, the s14 efficiency ratio at low p_t is also anti-correlated to the ratio at high p_t. What remains to explain then, is where the charge differences at high p_t originate from.

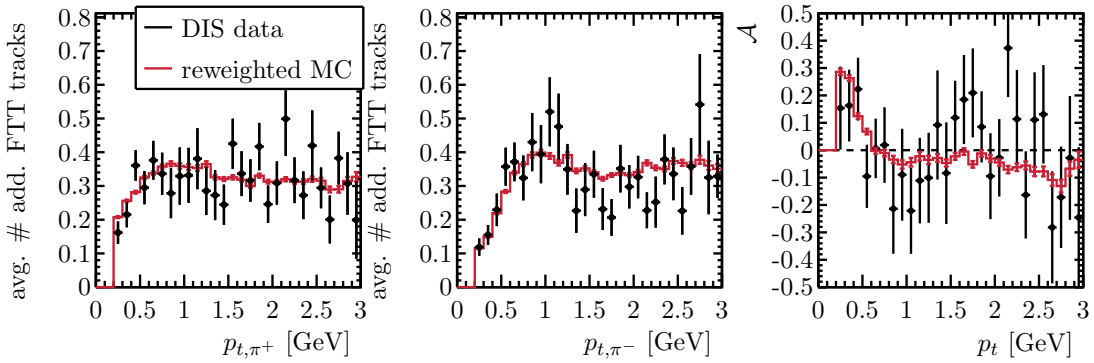

Figure 7.3.5: Average number of tracks seen by the FTT close to a reconstructed track in addition to the assigned FTT track for data and the combined elastic and proton-dissociative MC in DIS.

It turns out that two of the trigger elements that constitute the s14 subtrigger cause the observed asymmetry, namely the requirements FTT_mul_Ta<4 and FTT_chg_1 which in turn are related to two underlying asymmetric effects. The first of these effect is the previously discussed doubling of FTT tracks. In Figure 7.3.5 the number of FTT tracks that are created on average per event in the vicinity of a reconstructed pion candidate, i.e., in a region $\Delta\tilde{\varphi} < 0.314\,\text{rad}$, in addition to the assigned FTT track is shown as a function of the pions' transverse momenta and separately for both charges. In the plot, mostly the asymmetry is relevant for the discussion here, where it becomes apparent that a low p_t positive track has a significantly higher probability to be double counted by the FTT than a low p_t negative track while at higher p_t the situation is inverted. Consequently, the combination positive low p_t track and negative high p_t track results in an on average higher number of total FTT tracks than the opposite situation. This in turn causes a low subtrigger efficiency via the condition FTT_mul_Ta<4 in favor of the observed asymmetry. The effect appears to be slightly more pronounced in

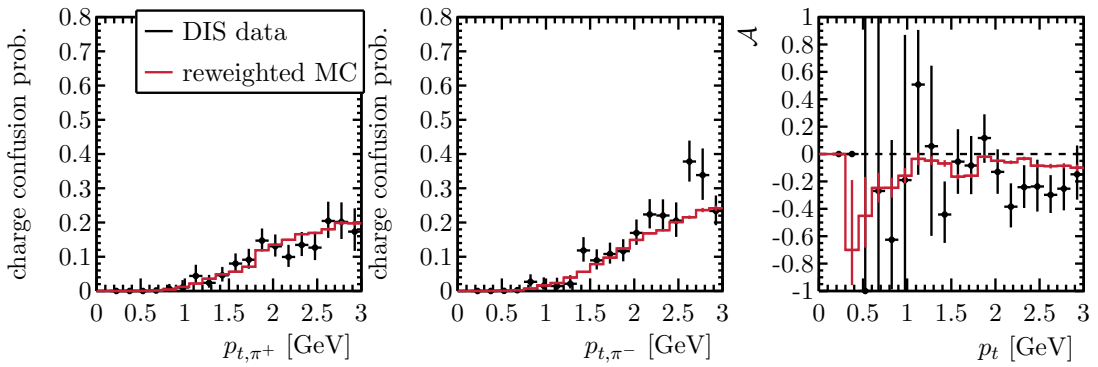

Figure 7.3.6: Fraction of positive and negative reconstructed tracks with an assigned FTT track having the opposite charge for data and the combined elastic and proton-dissociative MC in DIS.

the simulation than in the real data.

The second effect is related to the challenge to measure the charge of high p_t tracks with the FTT. Figure 7.3.6 shows the fraction of positive and negative reconstructed tracks that have an assigned FTT track with the opposite charge as a function of their respective transverse momenta. Starting at about 1 GeV, which corresponds to the second highest FTT p_t threshold, an increasing probability for charge confusion is observed. Also this effect shows a slight asymmetry such that charge confusion is more likely to happen for negative than for positive tracks. The requirement `FTT_chg_1` demands the total charge seen by the FTT to not deviate from zero by more than one. Consequently, confusing one charge lowers the `s14` efficiency, if the other charge is determined correctly. As this happens more often for the combination of a positive low p_t and negative high p_t track this combination is penalized which further contributes to the observed asymmetry in the efficiency.

From Figure 7.3.6 it should be noted that the charge confusion probability rises with p_t which contributes to the previously observed decline of the `s14` efficiency with Q^2.

In Figure 7.3.7 the `s14` efficiency is shown as a function of the azimuthal and in Figure 7.3.8 as a function of the polar angles of the tracks. The angular dependencies exhibit the same features as the previously studied FTT single track efficiency, which enter mostly via the trigger requirement to have at least two FTT tracks: A slight dependence of the `s14` efficiency on φ is observed coming from the inefficient CJC2 regions and the discussed transverse offset of the primary vertex position. In the θ dependence a 90° efficiency dip is still present. However, neither of these effects result in a larger charge asymmetry of the `s14` efficiency.

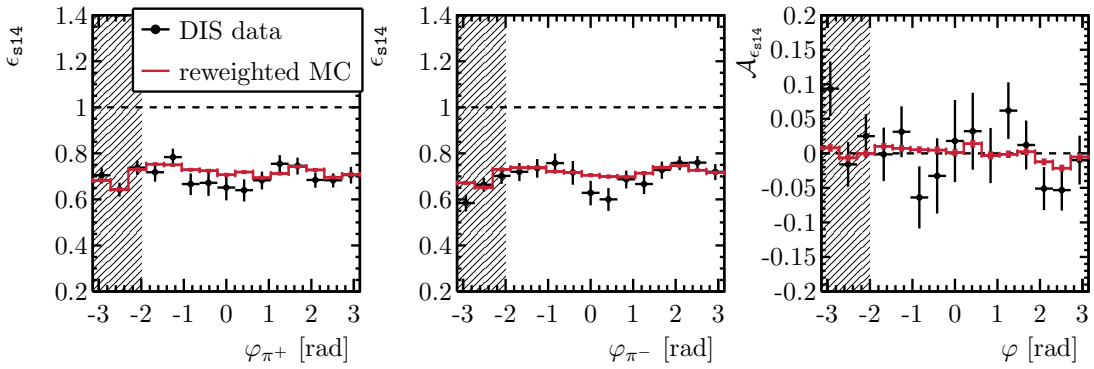

Figure 7.3.7: `s14` efficiency as a function of the pion candidates' φ in the signal region for data and the combined elastic and proton-dissociative MC in DIS.

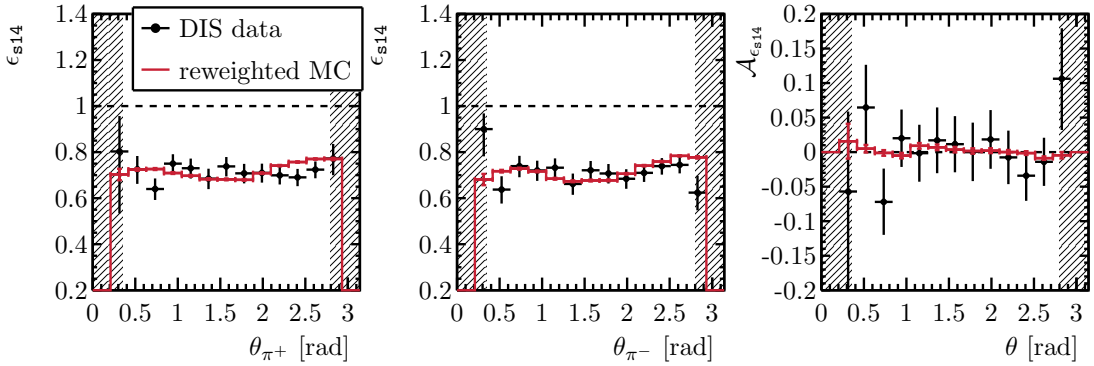

Figure 7.3.8: `s14` efficiency as a function of the pion candidates' θ in the signal region for data and the combined elastic and proton-dissociative MC in DIS.

7.4 Conclusion

In the previous sections the FTT is studied in the DIS $\rho^0 \to \pi^+\pi^-$ data and MC samples, and single track efficiencies and the `s14` trigger efficiency are measured. A large discrepancy between data and the simulation is observed only in the FTT track multiplicity distribution, where significantly more tracks are observed in data than in the MC. After correcting the MC by reweighting it in the FTT track multiplicity, a good agreement between FTT efficiencies measured in data and the MC is found. In particular, all studied kinematic dependencies of the efficiencies are compatible within the statistical uncertainties, including such that arise from complex detector effects.

Concerning charge asymmetries in the FTT, several things are observed. The CJC geometry and inefficient wires result in a φ and p_t dependent difference in the single track efficiency for positive and negative particles. Concerning the `s14`

trigger efficiency, charge asymmetric track doubling and charge confusion in the FTT result in a strong charge asymmetry in the dependence of the efficiency on the transverse momenta of the pion candidates. These effects become more important for high p_t and are particularly dramatic in the DIS regime, where the transverse momenta of the pions are strongly anti-correlated.

Many of the observed effects depend on Q^2, because the kinematics of the pion tracks change with Q^2. This is reflected explicitly in the observed Q^2 dependence of the `s14` efficiency. It is thus difficult to draw quantitative conclusions for the performance of the FTT under photoproduction conditions from the DIS sample. However, the simulation was shown to describe the data very well, even under the complex DIS conditions. In photoproduction the situation is much simpler and many problematic effects do not play a rôle. For example, the transverse momenta of the pions are small ($p_t \leq 1\,\text{GeV}$) and uncorrelated in photoproduction so that charge confusion in the FTT is less likely. Also, in photoproduction both Q^2 and t are very small, so that the transverse momentum of the $\pi^+\pi^-$ system is small as well. As a consequence, the pions tend to be back-to-back in the transverse plane which results in less track double counting (compare Figure 7.1.2). It can thus be assumed, that the `s14` trigger efficiency can be accurately measured in a photoproduction $\rho^0 \to \pi^+\pi^-$ MC and then used to correct the corresponding data sample.

To be able to do this, first one important issue needs to be solved. While in photoproduction the performance of the FTT in data and the simulation should agree much better than in DIS, e.g. because there is less track double counting in photoproduction, a correction of the MC, which was vital in DIS, might still be necessary. In DIS, reweighting the MC in the FTT track multiplicity distribution has shown itself to be very successful. Unfortunately, in an `s14` triggered data sample the trigger requirements only allow for events with either two or three FTT tracks. However, this might be enough to apply the correction method introduced in Section 7.1. If the two assumptions hold that, first, the parametrization introduced in Equation (7.1.2) is correct also in photoproduction, and secondly, that the single track FTT efficiency, i.e., the parameter p_{rec} in the fit model, is same in DIS and photoproduction, only two free model parameters remain, i.e., p_{add}, and N_{add}. Both assumptions can bet tested in the MC. The two available entries in the FTT track multiplicity distribution then suffice to fit the two remaining model parameters which allows to correct the photoproduction MC in the same way the DIS MC is corrected in this thesis.

8 Outlook: FTT Efficiency in $\pi^+\pi^-$ Photoproduction

In the previous section it is verified that the `s14` trigger efficiency can be measured correctly in a simulated DIS $\rho^0 \to \pi^+\pi^-$ sample, if the sample is reweighted in the FTT track multiplicity distribution. In this section it is briefly illustrated how something similar can be done in a simulated photoproduction $\rho^0 \to \pi^+\pi^-$ sample. This allows to measure the `s14` efficiency in MC and use it to correct a photoproduction $\rho^0 \to \pi^+\pi^-$ data sample.

8.1 DIS $\rho^0 \to \pi^+\pi^-$ Data Sample

For the photoproduction $\rho^0 \to \pi^+\pi^-$ data sample events from the same run period the DIS events are selected from in Chapter 6 are considered. For the MC sample simulated events as introduced in Section 5.1.2 are used. Events that are triggered by the `s14` ρ^0 subtrigger are collected and filtered by similar selection criteria as introduced for the DIS sample. Solely the electron requirements are changed and for the photoproduction sample the scattered electron must not be observed. Q^2 is set to $0\,\mathrm{GeV}^2$ for all events. A summary of the selection criteria is given in Appendix B in Table B.1.

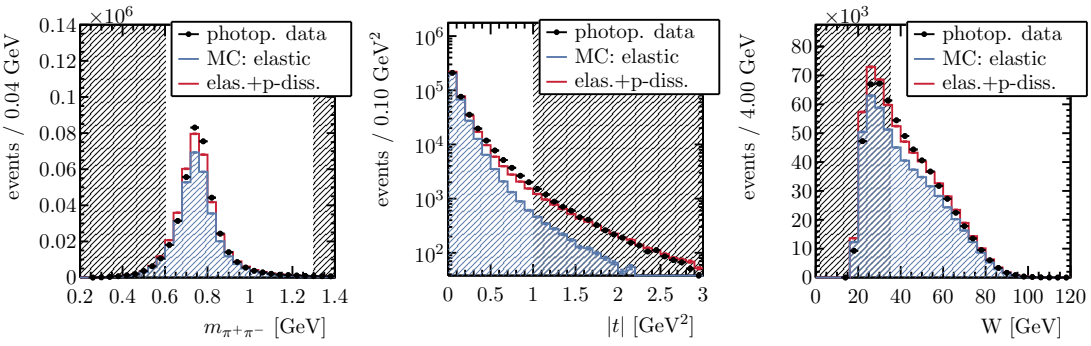

Figure 8.1.1: Distributions of $m_{\pi^+\pi^-}$ (left), t (center), and $W_{\gamma p}$ (right) in the `s14` triggered $\rho \to \pi^+\pi^-$ photoproduction data and MC sample. The gray bands limit the signal region.

In Figure 8.1.1 the $m_{\pi^+\pi^-}$, t, and $W_{\gamma p}$ distributions are shown for the data and MC photoproduction sample. The shaded regions limit the signal region. The cuts on t and $W_{\gamma p}$ are chosen as in Chapter 6. The upper cut on $m_{\pi^+\pi^-}$ is raised to 1.3 GeV to be able to study the efficiency also in the f_2 meson's mass region. The signal region cuts are summarized in Table B.1.

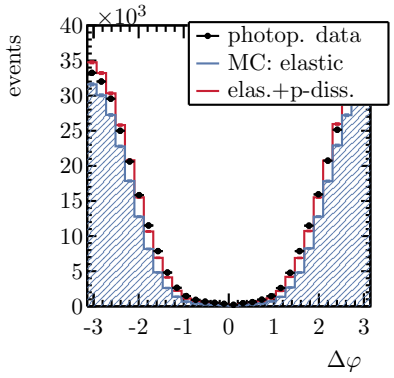

Figure 8.1.2: Distribution of the transverse opening angle $\Delta\varphi$ between the two pion candidates in the $\rho \to \pi^+\pi^-$ photoproduction sample.

As discussed in the previous chapter, key features of $\rho^0 \to \pi^+\pi^-$ production in photoproduction as compared to DIS are the smaller transverse momenta of the pion candidates and the larger azimuthal opening angle between the pions. The distribution of the azimuthal opening angle is shown in Figure 8.1.2 and yields that the pion candidates indeed tend to be back-to-back in photoproduction.

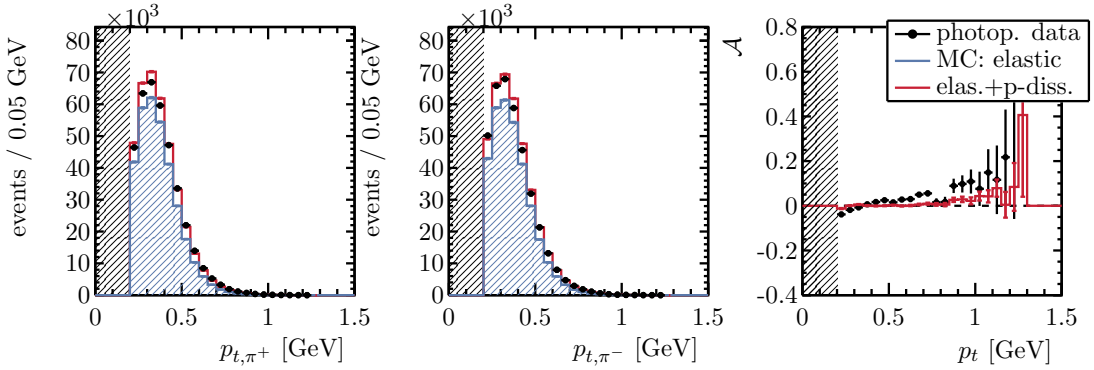

Figure 8.1.3: Transverse momentum distribution for positive (left) and negative (center) pion candidates and the corresponding asymmetry distribution (right) in the $\rho \to \pi^+\pi^-$ photoproduction sample. The gray bands mark the acceptance region.

The pion p_t for the positive and negative track are shown in Figure 8.1.3 together with the respective asymmetry plot. Interestingly, there is a large asymmetry between the p_t distributions of up to 5% in the data sample, which is missing in the MC. In the following, it is investigated whether this asymmetry is caused by the `s14` trigger.

8.2 `s14` Trigger Efficiency

The efficiency of the `s14` subtrigger can be measured in the MC sample, where the trigger requirement is not mandatory for events to be reconstructed. The efficiency is defined as

$$\epsilon^{MC}_{\texttt{s14}} = \frac{N_{sel,\texttt{s14}}}{N_{sel}}, \tag{8.2.1}$$

where N_{sel} is the number of selected events without requiring the `s14` condition, and $N_{sel,\texttt{s14}}$ is the fraction of those that in addition satisfy a positive `s14` decision.

8.2.1 FTT Track Multiplicity Correction

To obtain correct efficiency values in the MC, the sample is corrected by reweighting it in the FTT track multiplicity distribution. The `s14` trigger explicitly requires two or three tracks in the FTT (compare Section 7.3). The parametrization introduced in Section 7.1 to describe the track multiplicity distribution contains three parameters. To be able to reweight the MC anyhow, the assumption is made that the values for p_{rec}, which are closely related to the FTT single track efficiency, are the same for DIS and photoproduction. The remaining parameter p_{add} and the normalization can be obtained by fitting the two available entries in the FTT track multiplicity distribution. The fit is shown in Figure 8.2.1 and the fitted values are listed in Table 8.2.1.

In the MC, the FTT multiplicity distribution can be studied in the sample without the FTT track multiplicity `s14` trigger requirements `FTT_mul_Tb>1` and `FTT_mul_Ta<4`. This distribution can be fitted without fixing any parameters, which can be used to test the previously made assumptions. The corresponding fit is also shown in Figure 8.2.1 and the fit parameters are listed in Table 8.2.1. They deviate from the previously obtained parameters by approximately 1 percentage point. This could in principle be used to estimate a systematic uncertainty on the reweighting procedure and propagate it to the efficiency. However, this was not done for this thesis.

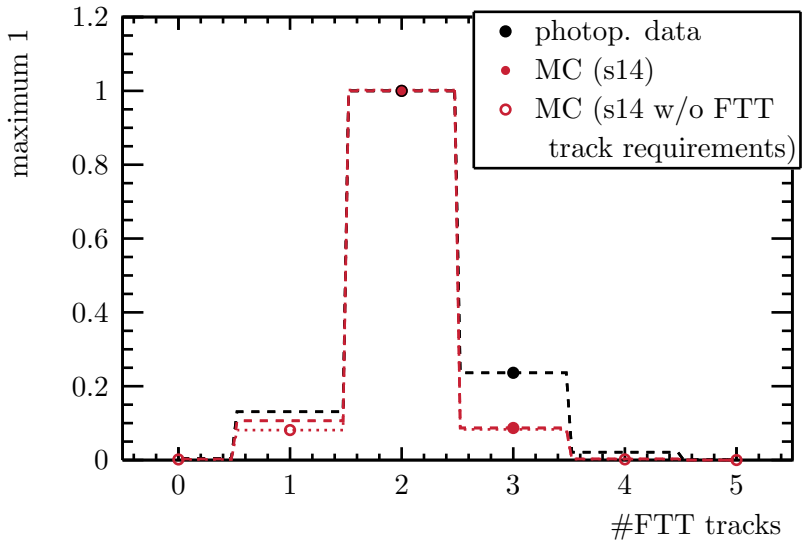

Figure 8.2.1: FTT track multiplicity distribution in the photoproduction data and MC sample. The parametrization from Equation (7.1.2) is fitted (dashed lines) to the two bins available after requiring a positive `s14` trigger decision. In the MC the fit is repeated (dotted line) in the sample without requiring the trigger bits `FTT_mul_Tb>1` and `FTT_mul_Ta<4`.

Table 8.2.1: Fit parameters obtained from fitting Equation (7.1.2) to the FTT track multiplicity distribution in the photoproduction sample.

fit parameter	data	MC: `s14`	MC: `s14` w/o FTT track requirements
p_{rec}	0.942 (fixed)	0.951(fixed)	0.963 ± 0.0003
p_{add}	0.056 ± 0.0003	0.021 ± 0.0002	0.020 ± 0.0002
N_{add}	2 (fixed)	2 (fixed)	2 (fixed)

8.2.2 `s14` Trigger Efficiency

The `s14` trigger efficiency measured in the photoproduction MC is listed in Table 8.2.2 before and after reweighting in the FTT multiplicity distribution. The differences between the values from the uncorrected and corrected MC are as small as about 1.4 percentage points and give a feeling for the importance and uncertainty of the reweighting procedure.

The `s14` trigger efficiency as a function of the invariant mass of the dipion system is shown in Figure 8.2.2 for both the unweighted and reweighted MC. For the reweighted MC the efficiency drops down by about ten percentage points over the considered mass range, for the unweighted MC the variation is less strong. This behavior is a consequence of the transverse momenta of the pion candidates

Table 8.2.2: `s14` trigger efficiency measured in the photoproduction MC in the signal region defined in Table B.1. The values are given before and after applying the FTT track multiplicity correction.

	reweighted MC	MC
`s14` [%]	84.49 ± 0.04(stat.)	85.85 ± 0.03(stat.)

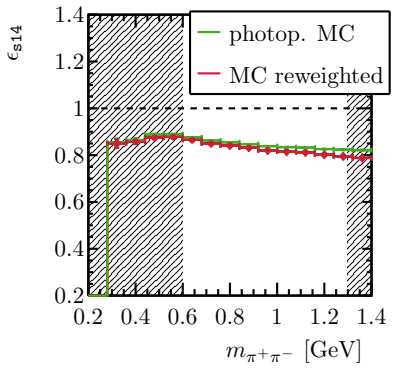

Figure 8.2.2: `s14` trigger efficiency as a function of $m_{\pi^+\pi^-}$ in the photoproduction MC before and after applying the FTT track multiplicity correction.

becoming slightly larger with increasing $m_{\pi^+\pi^-}$. In turn, the `s14` trigger efficiency drops down towards larger p_t as is explicitly discussed below in the text.

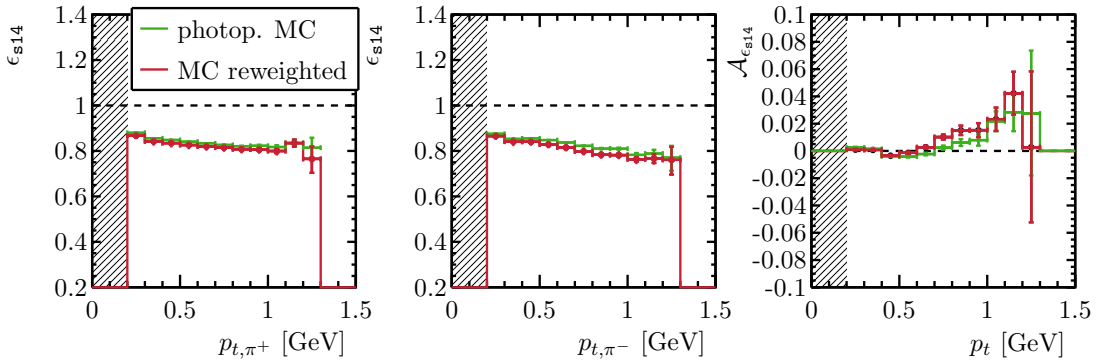

Figure 8.2.3: `s14` trigger efficiency as a function of the pion candidates' transverse momenta and the corresponding asymmetry plot in the photoproduction MC before and after applying the FTT track multiplicity correction.

To study trigger induced charge asymmetries, the dependence of the `s14` efficiency on the pion candidates' transverse momenta is shown in Figure 8.2.3. For both charges the efficiency drops down with increasing p_t. In the corrected MC, this

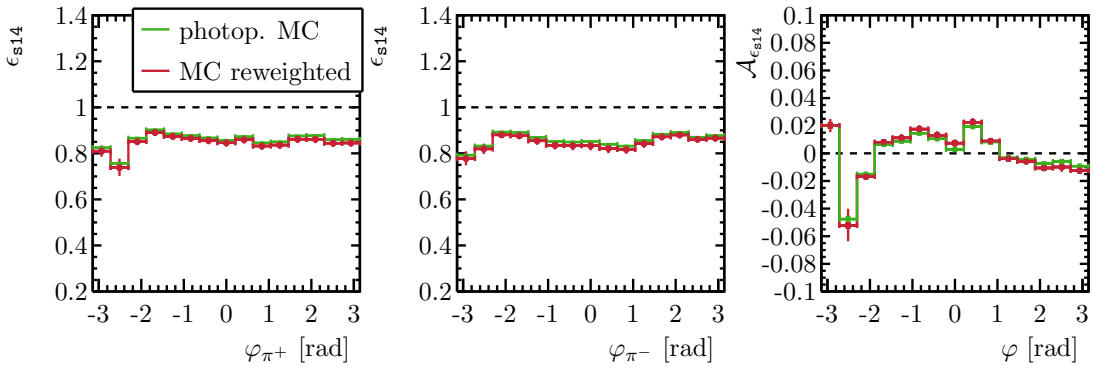

Figure 8.2.4: s14 trigger efficiency as a function of the pion candidates' azimuthal angle and the corresponding asymmetry plot in the photoproduction MC before and after applying the FTT track multiplicity correction.

tendency is again a bit stronger, in particular for negative tracks. A small charge asymmetry can be observed, which becomes larger with increasing p_t. This is all to be expected from the observations made in Section 7.3. Unfortunately, the trigger efficiency asymmetry is not sufficient to fully explain the asymmetry that can be observed in the p_t spectra of the positive and negative pion candidates in Figure 8.1.3. This is further commented on in Chapter 9.

In Figure 8.2.4 the s14 trigger efficiency is shown as a function of the pion tracks' azimuthal angles, together with the corresponding asymmetry. In contrast to DIS, in photoproduction a large asymmetry is present in the inefficient CJC region at low φ. Furthermore, the asymmetry due to the CJC geometry and the vertex offset, which is observed in the single track FTT efficiency in Section 7.3, is also strongly present. Both effects are more pronounced in photoproduction than in DIS because of the different event topologies. In photoproduction the pions' transverse momenta are smaller in favor of both asymmetries. In addition, the asymmetry due to the CJC geometry, which exhibits a 2π periodicity, is enhanced in photoproduction where the pions are back to back in the transverse plane. The asymmetry in φ is affected very little by the reweighting procedure. No asymmetry is present in the pion track θ dependencies of the efficiency and the corresponding plot is not shown.

Summarizing, the s14 trigger efficiency can be measured in photoproduction in the MC with the confidence in the correctness of the simulation that is obtained through the FTT studies in DIS. While a correction of the MC in photoproduction is much less critical than in DIS it can be achieved in a similar manner. Here, no systematic uncertainty on the correction was estimated. The efficiency measurements yield that there are indeed trigger induced charge asymmetries, which depend on the p_t and φ of the pion tracks.

9 Conclusion

In the first part of this thesis, charge asymmetries as a consequence of interference between C-even and C-odd contributions to $\pi^+\pi^-$ photoproduction are studied in the model by Ewerz et al. [14]. These charge asymmetries are expressed in asymmetries of the angular distributions of the pions in the dipion restframe. A focus is put on investigating the odderon contribution to the asymmetries and on the questions where it is strongest and how it can be distinguished from the Primakoff contribution. It is briefly studied how detector effects can modify the model asymmetry, where in particular detector induced charge asymmetries in the p_t and θ spectra of the pions in the lab-frame are critical, while asymmetries in the φ spectra seem to be harmless.

In the second part of this thesis, detector effects in the H1 central tracking system that can cause charge asymmetries are investigated by studying the FTT performance in DIS $\rho^0 \to \pi^+\pi^-$ events. In particular, the geometry of the CJC is found to give rise charge asymmetries in the single track FTT efficiency depending on the kinematics of the pions. Furthermore, charge confusion and track doubling in the FTT are revealed to cause large charge asymmetries in the kinematic dependence of the `s14` trigger efficiency. It is verified that all these effects are well described by the detector simulation after applying a correction. In conclusion, the simulation can be used to measure the `s14` trigger efficiency in photoproduction to correct a photoproduction $\pi^+\pi^-$ data sample.

The `s14` trigger efficiency as measured using simulated photoproduction events gives rise to asymmetries in the pion p_t and φ spectra whose origins are well understood. Unfortunately, the asymmetries observed in the pion p_t spectra of the photoproduction data sample used in this thesis show larger asymmetries than what can be explained by the measured trigger efficiency. Thus other effects must contribute and need to be investigated. A good point to start is to critically analyze the event selection, which was not optimized in the context of this thesis. However, the observation was made that in particular the dE/dx cuts and the requirement to have no more than 2 tracks in the central tracker (including non-vertex fitted tracks) can distort the kinematic distributions of the pion tracks differently depending on the charge. Furthermore, the effects observed to influence the FTT can be expected to also influence the reconstruction of full CJC tracks and thus further increase any asymmetry caused by the FTT. Finally, in parallel to this thesis Sauter [36] investigated how beam-restgas interactions can excite

resonant states in the restgas atoms, which can decay by emitting a pion and a proton. These processes are inherently charge asymmetric and in some kinematic regions cannot be well separated from the photoproduction $\pi^+\pi^-$ signal.

While as a result of this thesis, the FTT is well understood, all of the other effects need also be well understood, if a measurement of the model asymmetries investigated in the first part of this thesis is to be performed.

Part III

APPENDIX

A FTT Track Assignment Algorithm

To assign tracks measured by the FTT to offline reconstructed tracks the following steps are performed. They are motivated by the goal to only assign compatible tracks, maximize the number of assignments and simultaneously minimize the sum of distances between all assigned tracks. The compatibility requirement and distance measure are defined in Section 4.3.

1. The matrix of (binned) distances between all possible pairs of reconstructed and FTT tracks is calculated.
2. This matrix is squared by adding an appropriate number of zero-filled rows or columns.
3. The distances of all track pairs that exceed the maximum accepted distance is set to the largest possible double-value ("∞"). By doing this a higher number of assigned track pairs is favored over a small sum of distances.[1] This is motivated by the assumption that if the FTT sees a track, the offline reconstruction should also see it.
4. The Hungarian Algorithm is performed on this matrix to determine the minimum sum of matrix elements such that each row and each column only contributes once. A recipe for the algorithm is the following, an example can be found in Figure A.1:
   - i The smallest element of each row is subtracted from all entries in that row. Continue with ii.
   - ii In the resulting matrix as many zeroes as possible are marked by a star. There must not be more then one starred zero in each row and column. Continue with iii.
   - iii The columns that contain a starred zero are covered. If all columns are covered, a complete set of unique assignments is given by the starred zeroes. If not, continue with iv.

[1] Assume three track pairs with best sum of distances $1 + 1 + 6 = 8$ for one set of assignments and $3 + 3 + 3 = 9$ for another. The Hungarian Algorithm favors the first. For a maximum accepted distance of 5 the last assignment is then rejected. The chosen modification of the matrix of distances, however, leads to the second, complete set of assignments with a slightly worse sum of distances.

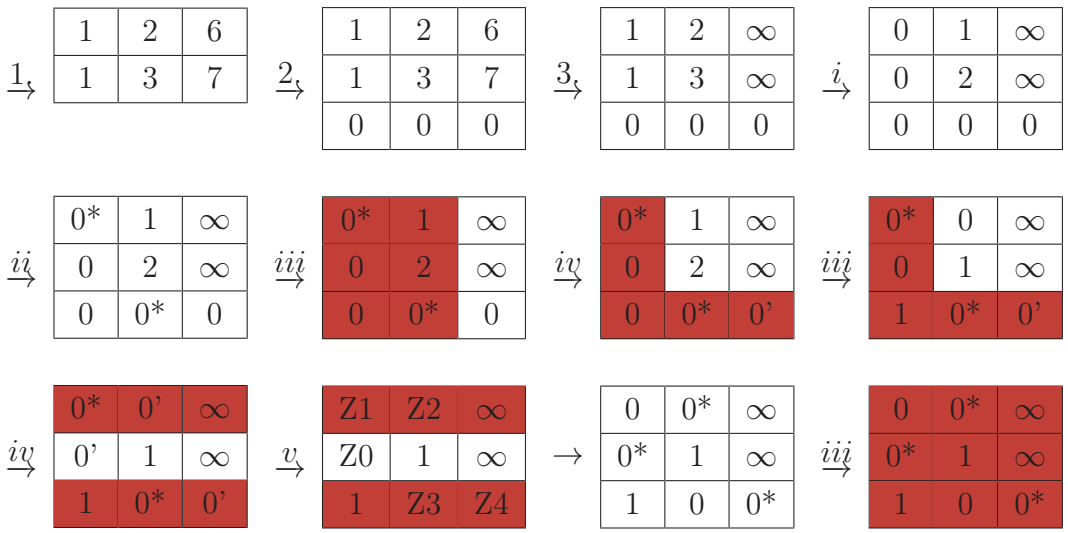

Figure A.1: A simple example for track assignment with the Hungarian Algorithm. It starts with a matrix of distances at the top left and continues along the arrows according to the steps described in the text. A maximum accepted distance of 5 is assumed.

iv A zero that is not covered is chosen and primed. If there is no starred zero in the same row, continue with v. If there is one, the row is covered and the column containing that starred zero is uncovered. Uncovered zeroes are primed in this fashion until there are none left. Then the smallest uncovered value is stored. Continue with vi.

v The primed zero found in iv is labeled “Z0”. If there is a starred zero in the column of Z0, it is labeled “Z1”. In this case there will also be a primed zero in the row of Z1 which gets the label “Z2”. This series of alternating primed and starred zeroes is continued until a primed zero in a column without a starred zero is reached. The stars from all starred zeroes in the series (uneven labels) are then removed and the primed zeroes in the series are marked by a star (even labels). All primes are erased and all rows and columns are uncovered. Continue with iii.

vi The value stored in iv is subtracted from each element in all uncovered columns and added to each element in every covered row. Stars, primes or covered rows and colums are not modified. Continue with iv.

5. The matrix elements selected by the Hungarian Algorithm indicate the optimal track assignment. Assignments of tracks that exceed the maximum accepted distance can be safely discarded. As are assignments to artificial indexes that were introduced to square the distance matrix.

B Selection Cuts

The selection requirements for the DIS and photoproduction data samples used in the thesis are summarized in Table B.1.

Table B.1: Summary of the selection criteria for the DIS and photoproduction $\rho \to \pi^+\pi^-$ data samples.

selection requirement	DIS	photoproduction
run selection	high energy 2006 and 2007 `CJC, CIP, FPS, FTT, LAr, SpaCal, TOF, LUMI, VETO`	
trigger	`s0 || s1 || s2`	`s14`
pion track criteria	$p_t > 200\,\text{MeV}$ && $20^\circ < \theta < 160^\circ$ $d_{ca} < 10\,\text{cm}$ && $z_{vtx} < 25\,\text{cm}$	
electron criteria	$E_{e',clust} > 17\,\text{GeV}$ $R_{e',CT} < 15\,\text{cm}$ fiducial cuts	no scattered electron
LAr veto	no unassociated clusters above 400 MeV in $\theta > 10^\circ$ region	
PID	π selection and K, p, and d vetoes	
background rejection	φ, K^0 and cosmic muon vetoes	
signal region	$-1\,\text{GeV}^2 < t$ $35\,\text{GeV} < W_{\gamma p} < 180\,\text{GeV}$	
	$0.6\,\text{GeV} < m_{\pi^+\pi^-} < 1.1\,\text{GeV}$ $2.5\,\text{GeV}^2 < Q^2$	$0.6\,\text{GeV} < m_{\pi^+\pi^-} < 1.3\,\text{GeV}$

Bibliography

[1] S.L. Glashow. Partial Symmetries of Weak Interactions. *Nucl.Phys.*, 22: 579–588, 1961. doi: 10.1016/0029-5582(61)90469-2.

[2] Steven Weinberg. A model of leptons. *Phys. Rev. Lett.*, 19:1264–1266, Nov 1967. doi: 10.1103/PhysRevLett.19.1264. URL http://link.aps.org/doi/10.1103/PhysRevLett.19.1264.

[3] A. Salam and J.C. Ward. Electromagnetic and weak interactions. *Physics Letters*, 13(2):168 – 171, 1964. ISSN 0031-9163. doi: http://dx.doi.org/10.1016/0031-9163(64)90711-5. URL http://www.sciencedirect.com/science/article/pii/0031916364907115.

[4] H. Fritzsch, M. Gell-Mann, and H. Leutwyler. Advantages of the color octet gluon picture. *Physics Letters B*, 47(4):365 – 368, 1973. ISSN 0370-2693. doi: http://dx.doi.org/10.1016/0370-2693(73)90625-4. URL http://www.sciencedirect.com/science/article/pii/0370269373906254.

[5] H. David Politzer. Reliable perturbative results for strong interactions? *Phys. Rev. Lett.*, 30:1346–1349, Jun 1973. doi: 10.1103/PhysRevLett.30.1346. URL http://link.aps.org/doi/10.1103/PhysRevLett.30.1346.

[6] David J. Gross and Frank Wilczek. Ultraviolet behavior of non-abelian gauge theories. *Phys. Rev. Lett.*, 30:1343–1346, Jun 1973. doi: 10.1103/PhysRevLett.30.1343. URL http://link.aps.org/doi/10.1103/PhysRevLett.30.1343.

[7] Kenneth G. Wilson. Confinement of quarks. *Phys. Rev. D*, 10:2445–2459, Oct 1974. doi: 10.1103/PhysRevD.10.2445. URL http://link.aps.org/doi/10.1103/PhysRevD.10.2445.

[8] T Regge. Introduction to complex orbital momenta. *Nuovo Cimento*, 14: 951–976, 1959.

[9] T Regge. *Nuovo Cimento*, 18:947–956, 1960.

[10] Carlo Ewerz. The Odderon in Quantum Chromodynamics. *arXiv:hep-ph/0306137*, June 2003. URL http://arxiv.org/abs/hep-ph/0306137.

[11] L. Lukaszuk and B. Nicolescu. *Nuovo Cimento Lett*, 8:405, 1973.

[12] I.F. Ginzburg, I.P. Ivanov, and N.N. Nikolaev. Possible odderon discovery via observation of charge asymmetry in the diffractive pi+ pi- production at HERA. *Eur.Phys.J.direct*, C5:02, 2003.

[13] I.P. Ivanov, Nikolai N. Nikolaev, and I.F. Ginzburg. Possible odderon discovery at HERA via charge asymmetry in the diffractive pi+pi- production. pages 728–731, 2001.

[14] Carlo Ewerz, Markos Maniatis, and Otto Nachtmann. A Model for Soft High-Energy Scattering: Tensor Pomeron and Vector Odderon. *Annals Phys.*, 342:31–77, 2014. doi: 10.1016/j.aop.2013.12.001.

[15] Sandy Donnachie, Günter Dosch, Peter Landshoff, and Otto Nachtmann. *Pomeron Physics and QCD*. Cambridge University Press, 2002. ISBN 9780511534935. URL `http://dx.doi.org/10.1017/CBO9780511534935`.

[16] P. D. B. Collins. *An Introduction to Regge Theory and High Energy Physics*. Cambridge University Press, 1977. ISBN 9780511897603. URL `http://dx.doi.org/10.1017/CBO9780511897603`.

[17] K.A. Olive et al. (Particle Data Group). Review of particle physics. *Chin.Phys.*, C38:090001, 2014. doi: 10.1088/1674-1137/38/9/090001.

[18] Ronald Weber. *Diffractive ρ^0 photoproduction at HERA*. PhD thesis, ETH Zürich, 2006. URL `https://www-h1.desy.de/psfiles/theses/h1th-440.pdf`.

[19] Geoffrey F Chew and Steven C Frautschi. Regge trajectories and the principle of maximum strength for strong interactions. *Physical Review Letters*, 8(1):41–44, 1962.

[20] V.N. Gribov. Partial waves with complex orbital angular momenta and the asymptotic behavior of the scattering amplitude. *Sov. Phys. JETP*, 14:1395, 1962.

[21] F. E. Low. Model of the bare pomeron. *Phys. Rev. D*, 12:163–173, Jul 1975. doi: 10.1103/PhysRevD.12.163. URL `http://link.aps.org/doi/10.1103/PhysRevD.12.163`.

[22] S. Nussinov. Colored-quark version of some hadronic puzzles. *Phys. Rev. Lett.*, 34:1286–1289, May 1975. doi: 10.1103/PhysRevLett.34.1286. URL `http://link.aps.org/doi/10.1103/PhysRevLett.34.1286`.

[23] E.A. Kuraev, L.N. Lipatov, and Victor S. Fadin. The Pomeranchuk Singularity in Nonabelian Gauge Theories. *Sov.Phys.JETP*, 45:199–204, 1977.

[24] I.I. Balitsky and L.N. Lipatov. The Pomeranchuk Singularity in Quantum Chromodynamics. *Sov.J.Nucl.Phys.*, 28:822–829, 1978.

[25] Stanley J. Brodsky, Johan Rathsman, and Carlos Merino. Odderon-Pomeron interference. *Phys.Lett.*, B461:114–122, 1999. doi: 10.1016/S0370-2693(99)00807-2.

[26] B. L. Ioffe. Space-time picture of photon and neutrino scattering and electroproduction cross section asymptotics. *Physics Letters B*, 30(2): 123–125, September 1969. ISSN 0370-2693. doi: 10.1016/0370-2693(69)90415-8. URL http://www.sciencedirect.com/science/article/pii/0370269369904158.

[27] J. J. Sakurai. Vector-Meson Dominance and High-Energy Electron-Proton Inelastic Scattering. *Physical Review Letters*, 22(18):981–984, May 1969. doi: 10.1103/PhysRevLett.22.981. URL http://link.aps.org/doi/10.1103/PhysRevLett.22.981.

[28] J. J. Sakurai and D. Schildknecht. Generalized vector dominance and inelastic electron-proton scattering. *Physics Letters B*, 40(1):121–126, June 1972. ISSN 0370-2693. doi: 10.1016/0370-2693(72)90300-0. URL http://www.sciencedirect.com/science/article/pii/0370269372903000.

[29] J. J. Sakurai and D. Schildknecht. Generalized vector dominance and inelastic electron-nucleon scattering - the neutron-to-proton ratio. *Physics Letters B*, 41(4):489–494, October 1972. ISSN 0370-2693. doi: 10.1016/0370-2693(72)90682-X. URL http://www.sciencedirect.com/science/article/pii/037026937290682X.

[30] J. J. Sakurai and D. Schildknecht. Generalized vector dominance and inelastic electron nucleon scattering — the small ω' region. *Physics Letters B*, 42(2):216–220, November 1972. ISSN 0370-2693. doi: 10.1016/0370-2693(72)90065-2. URL http://www.sciencedirect.com/science/article/pii/0370269372900652.

[31] T. H. Bauer, R. D. Spital, D. R. Yennie, and F. M. Pipkin. The hadronic properties of the photon in high-energy interactions. *Reviews of Modern Physics*, 50(2):261–436, April 1978. doi: 10.1103/RevModPhys.50.261. URL http://link.aps.org/doi/10.1103/RevModPhys.50.261.

[32] Arthur Bolz, Carlo Ewerz, Markos Maniatis, Otto Nachtmann, Michel Sauter, et al. Photoproduction of π^+ π^- pairs in a model with tensor-pomeron and vector-odderon exchange. *JHEP*, 1501:151, 2015. doi: 10.1007/JHEP01(2015)151.

[33] H. Primakoff. Photo-production of neutral mesons in nuclear electric fields and the mean life of the neutral meson. *Phys. Rev.*, 81:899–899, Mar 1951. doi: 10.1103/PhysRev.81.899. URL http://link.aps.org/doi/10.1103/PhysRev.81.899.

[34] K. Gottfried and John David Jackson. On the Connection between production mechanism and decay of resonances at high-energies. *Nuovo Cim.*, 33: 309–330, 1964. doi: 10.1007/BF02750195.

[35] J.D. Jackson. Remarks on the phenomenological analysis of resonances. *Il Nuovo Cimento Series 10*, 34(6):1644–1666, 1964. ISSN 0029-6341. doi: 10.1007/BF02750563. URL http://dx.doi.org/10.1007/BF02750563.

[36] Michel Sauter. Personal communication, Michel.Sauter@desy.de, ∼sautem/h1/DiPionAnalysis/, April 2015. URL https://www-h1.desy.de/icgi-h1wiki/moin.cgi/PhysicsAnalysisForum/PhysicsAnalysisForum2015-03-19?action=AttachFile&do=get&target=Sauter.pdf.

[37] R. Mertig, M. Böhm, and A. Denner. Feyn calc - computer-algebraic calculation of feynman amplitudes. *Computer Physics Communications*, 64(3):345 – 359, 1991. ISSN 0010-4655. doi: http://dx.doi.org/10.1016/0010-4655(91)90130-D. URL http://www.sciencedirect.com/science/article/pii/001046559190130D.

[38] E. Byckling and K. Kajantie. *Particle Kinematics*. Wiley, 1973.

[39] **ZEUS Collaboration**. Exclusive electroproduction of two pions at HERA. *The European Physical Journal C*, 72(1):1–12, January 2012. ISSN 1434-6044, 1434-6052. doi: 10.1140/epjc/s10052-012-1869-5.

[40] **H1 Collaboration**. Diffractive electroproduction of ρ and ϕ mesons at HERA. *Journal of High Energy Physics*, 2010(5):1–111, May 2010. ISSN 1029-8479. doi: 10.1007/JHEP05(2010)032.

[41] **ZEUS Collaboration**. Exclusive ρ^0 production in deep inelastic scattering at HERA. *PMC Physics A*, 1:6, 2007. ISSN 17540410. doi: 10.1186/1754-0410-1-6.

[42] **H1 Collaboration**. Diffractive photoproduction of ρ mesons with large momentum transfer at HERA. *Physics Letters B*, 638(5–6):422–431, July 2006. ISSN 0370-2693. doi: 10.1016/j.physletb.2006.05.042.

[43] **ZEUS Collaboration**. Measurement of proton-dissociative diffractive photoproduction of vector mesons at large momentum transfer at HERA. *The European Physical Journal C - Particles and Fields*, 26(3):389–409, January 2003. ISSN 1434-6044, 1434-6052. doi: 10.1140/epjc/s2002-01079-0.

[44] **H1 Collaboration**. Elastic electroproduction of ρ mesons at HERA. *The European Physical Journal C - Particles and Fields*, 13(3):371–396, April 2000. ISSN 1434-6044, 1434-6052. doi: 10.1007/s100520000150.

[45] **ZEUS Collaboration**. Measurement of the spin-density matrix elements in exclusive electroproduction of ρ^0 mesons at HERA. *The European Physical Journal C - Particles and Fields*, 12(3):393–410, February 2000. ISSN 1434-6044, 1434-6052. doi: 10.1007/s100529900246.

[46] **ZEUS Collaboration**. Measurement of diffractive photoproduction of vector mesons at large momentum transfer at HERA. *The European Physical Journal C - Particles and Fields*, 14(2):213–238, May 2000. ISSN 1434-6044, 1434-6052. doi: 10.1007/s100520000374.

[47] **ZEUS Collaboration**. Exclusive electroproduction of ρ^0 and j/ψ mesons at HERA. *The European Physical Journal C - Particles and Fields*, 6(4):603–627, January 1999. ISSN 1434-6044, 1434-6052. doi: 10.1007/s100529901051.

[48] **ZEUS Collaboration**. Elastic and proton dissociative ρ^0 photoproduction at HERA. *Eur.Phys.J.*, C2:247–267, 1998. doi: 10.1007/s100520050136.

[49] **ZEUS Collaboration**. Elastic and proton-dissociative ρ^0 photoproduction at HERA. *The European Physical Journal C - Particles and Fields*, 2(2):247–267, April 1998. ISSN 1434-6044, 1434-6052. doi: 10.1007/s100529800834.

[50] **H1 Collaboration**. Proton dissociative ρ and elastic ϕ electroproduction at HERA. *Zeitschrift für Physik C Particles and Fields*, 75(4):607–618, December 1997. ISSN 0170-9739, 1431-5858. doi: 10.1007/s002880050506.

[51] **H1 Collaboration**. Elastic photoproduction of ρ^0 mesons at HERA. *Nuclear Physics B*, 463(1):3–29, March 1996. ISSN 0550-3213. doi: 10.1016/0550-3213(96)00045-4.

[52] **H1 Collaboration**. Elastic electroproduction of ρ and j/ψ mesons at large q^2 at HERA. *Nuclear Physics B*, 468(1–2):3–33, May 1996. ISSN 0550-3213. doi: 10.1016/0550-3213(96)00192-7.

[53] **ZEUS Collaboration**. Measurement of elastic ρ^0 photoproduction at HERA. *Z.Phys.*, C69:39–54, 1995. doi: 10.1007/s002880050004.

[54] **ZEUS Collaboration**. Exclusive ρ^0 production in deep inelastic electron-proton scattering at HERA. *Physics Letters B*, 356(4):601–616, August 1995. ISSN 0370-2693. doi: 10.1016/0370-2693(95)00879-P.

[55] **ZEUS Collaboration**. Exclusive electroproduction of ϕ mesons at HERA. *Nuclear Physics B*, 718(1–2):3–31, July 2005. ISSN 0550-3213. doi: 10.1016/j.nuclphysb.2005.04.009.

[56] **H1 Collaboration**. Measurement of elastic electroproduction of ϕ mesons at HERA. *Physics Letters B*, 483(4):360–372, June 2000. ISSN 0370-2693. doi: 10.1016/S0370-2693(00)00613-4.

[57] **ZEUS Collaboration**. Measurement of the reaction $\gamma * p \to \phi p$ in deep inelastic e^+p scattering at HERA. *Physics Letters B*, 380(1–2):220–234, July 1996. ISSN 0370-2693. URL `http://www.sciencedirect.com/science/article/pii/037026939600603X`.

[58] **ZEUS Collaboration**. Measurement of elastic ϕ photoproduction at HERA. *Physics Letters B*, 377(4):259–272, June 1996. ISSN 0370-2693. doi: 10.1016/0370-2693(96)00172-4.

[59] **ZEUS Collaboration**. Measurement of elastic ω photoproduction at HERA ZEUS Collaboration. *Zeitschrift für Physik C Particles and Fields*, 73(1):73–84, March 2014. ISSN 0170-9739, 1431-5858. doi: 10.1007/s002880050297.

[60] **ZEUS Collaboration**. Measurement of exclusive ω electroproduction at HERA. *Physics Letters B*, 487(3–4):273–288, August 2000. ISSN 0370-2693. doi: 10.1016/S0370-2693(00)00794-2.

[61] **ZEUS Collaboration**. Measurement of elastic j/ψ photoproduction at HERA. *Zeitschrift für Physik C Particles and Fields*, 75(2):215–228, April 2014. ISSN 0170-9739, 1431-5858. doi: 10.1007/s002880050464.

[62] **ZEUS Collaboration**. Measurement of j/ψ photoproduction at large momentum transfer at HERA. *Journal of High Energy Physics*, 2010(5): 1–36, May 2010. ISSN 1029-8479. doi: 10.1007/JHEP05(2010)085.

[63] **H1 Collaboration**. Elastic j/ψ production at HERA. *The European Physical Journal C - Particles and Fields*, 46(3):585–603, April 2006. ISSN 1434-6044, 1434-6052. doi: 10.1140/epjc/s2006-02519-5.

[64] **ZEUS Collaboration**. Exclusive electroproduction of j/ψ mesons at HERA. *Nuclear Physics B*, 695(1–2):3–37, September 2004. ISSN 0550-3213. doi: 10.1016/j.nuclphysb.2004.06.034.

[65] **H1 Collaboration**. Diffractive photoproduction of j/ψ mesons with large momentum transfer at HERA. *Physics Letters B*, 568(3–4):205–218, August 2003. ISSN 0370-2693. doi: 10.1016/j.physletb.2003.06.056.

[66] **ZEUS Collaboration**. Exclusive photoproduction of j/ψ mesons at HERA. *The European Physical Journal C - Particles and Fields*, 24(3):345–360, July 2002. ISSN 1434-6044, 1434-6052. doi: 10.1007/s10052-002-0953-7.

[67] **H1 Collaboration**. Elastic photoproduction of j/ψ and υ mesons at HERA. *Physics Letters B*, 483(1–3):23–35, June 2000. ISSN 0370-2693. doi: 10.1016/S0370-2693(00)00530-X.

[68] **H1 Collaboration**. Charmonium production in deep inelastic scattering at HERA. *The European Physical Journal C - Particles and Fields*, 10(3):373–393, October 1999. ISSN 1434-6044, 1434-6052. doi: 10.1007/s100529900138.

[69] **H1 Collaboration**. Elastic and inelastic photoproduction of j/ψ mesons at HERA. *Nuclear Physics B*, 472(1–2):3–31, July 1996. ISSN 0550-3213. doi: 10.1016/0550-3213(96)00274-X.

[70] **ZEUS Collaboration**. Measurement of the cross section for the reaction $\gamma p \to j/\psi p$ with the ZEUS detector at HERA. *Physics Letters B*, 350(1): 120–134, May 1995. ISSN 0370-2693. doi: 10.1016/0370-2693(95)00403-8.

[71] **H1 Collaboration**. Photoproduction of j/ψ mesons at HERA. *Physics Letters B*, 338(4):507–518, November 1994. ISSN 0370-2693. doi: 10.1016/0370-2693(94)90806-0.

[72] **H1 Collaboration**. Diffractive photoproduction of $\psi(2s)$ mesons at HERA. *Physics Letters B*, 541(3–4):251–264, August 2002. ISSN 0370-2693. doi: 10.1016/S0370-2693(02)02275-X.

[73] **H1 Collaboration**. Photo-production of $\psi(2s)$ mesons at HERA. *Physics Letters B*, 421(1–4):385–394, March 1998. ISSN 0370-2693. doi: 10.1016/S0370-2693(97)01529-3.

[74] **ZEUS Collaboration**. Measurement of the t dependence in exclusive photoproduction of $\upsilon(1s)$ mesons at HERA. *Physics Letters B*, 708(1–2): 14–20, February 2012. ISSN 0370-2693. doi: 10.1016/j.physletb.2012.01.009.

[75] **ZEUS Collaboration**. Exclusive photoproduction of υ mesons at HERA. *Physics Letters B*, 680(1):4–12, September 2009. ISSN 0370-2693. doi: 10.1016/j.physletb.2009.07.066.

[76] **ZEUS Collaboration**. Measurement of elastic υ photoproduction at HERA. *Physics Letters B*, 437(3–4):432–444, October 1998. ISSN 0370-2693. doi: 10.1016/S0370-2693(98)01081-8.

[77] H. Alvensleben, U. Becker, W. Busza, M. Chen, K.J. Cohen, et al. Precise Determination of ρ-ω Interference Parameters from Photoproduction of Vector Mesons Off Nucleon and Nuclei. *Phys.Rev.Lett.*, 27:888–892, 1971. doi: 10.1103/PhysRevLett.27.888.

[78] G. Breit and E. Wigner. Capture of slow neutrons. *Phys. Rev.*, 49:519–531, Apr 1936. doi: 10.1103/PhysRev.49.519. URL http://link.aps.org/doi/10.1103/PhysRev.49.519.

[79] S. D. Drell. Production of particle beams at very high energies. *Phys. Rev. Lett.*, 5:278–281, Sep 1960. doi: 10.1103/PhysRevLett.5.278. URL http://link.aps.org/doi/10.1103/PhysRevLett.5.278.

[80] S. D. Drell. Peripheral contributions to high-energy interaction processes. *Rev. Mod. Phys.*, 33:458–466, Jul 1961. doi: 10.1103/RevModPhys.33.458. URL http://link.aps.org/doi/10.1103/RevModPhys.33.458.

[81] P. Söding. On the apparent shift of the rho meson mass in photoproduction. *Physics Letters*, 19(8):702 – 704, 1966. ISSN 0031-9163. doi: http://dx.doi.org/10.1016/0031-9163(66)90451-3. URL http://www.sciencedirect.com/science/article/pii/0031916366904513.

[82] Deutsches Elektronen-Synchrotron (DESY). URL http://www.desy.de/.

[83] **H1 Collaboration**. ep Physics beyond 1999. H1 internal report, October 1997. H1-IN-531(10/1997).

[84] Uwe Schneekloth. Recent HERA results and future prospects. 1998.

[85] H1Zeus - HERA combined results, April 2015. URL https://www.desy.de/h1zeus/combined_results/index.php.

[86] **H1 Collaboration**. The H1 detector at HERA. *Nuclear Instruments and Methods in Physics Research Section A: Accelerators, Spectrometers, Detectors and Associated Equipment*, 386(2–3):310 – 347, 1997. ISSN 0168-9002. doi: http://dx.doi.org/10.1016/S0168-9002(96)00893-5. URL http://www.sciencedirect.com/science/article/pii/S0168900296008935.

[87] **H1 Collaboration**. The tracking, calorimeter and muon detectors of the H1 experiment at HERA. *Nuclear Instruments and Methods in Physics Research Section A: Accelerators, Spectrometers, Detectors and Associated Equipment*, 386(2–3):348 – 396, 1997. ISSN 0168-9002. doi: http://dx.doi.org/10.1016/S0168-9002(96)00894-7. URL http://www.sciencedirect.com/science/article/pii/S0168900296008947.

[88] J. Bürger, L. Criegee, G. Franke, H. Klär, J. Meyer, J. Schug, M. Schulz, P. Steffen, P. Waloschek, G.G. Winter, W. Zimmermann, U. Gaethke, E. Schenuit, and H. Spitzer. The central jet chamber of the H1 experiment. *Nuclear Instruments and Methods in Physics Research Section A: Accelerators, Spectrometers, Detectors and Associated Equipment*, 279(1–2):217 – 222, 1989. ISSN 0168-9002. doi: http://dx.doi.org/10.1016/0168-9002(89)

91084-X. URL http://www.sciencedirect.com/science/article/pii/016890028991084X.

[89] Max Christoph Urban. *The new CIP2k z-Vertex Trigger for the H1 Experiment at HERA*. PhD thesis, Universität Zürich, 2004. URL https://www-h1.desy.de/psfiles/theses/h1th-366.pdf.

[90] J. Becker, K. Bosiger, L. Lindfeld, K. Muller, P. Robmann, et al. A Vertex trigger based on cylindrical multiwire proportional chambers. *Nucl.Instrum.Meth.*, A586:190–203, 2008. doi: 10.1016/j.nima.2007.11.024.

[91] B. Andrieu and others, **H1 Calorimeter Group**. The H1 liquid argon calorimeter system. *Nucl.Instrum.Meth.*, A336:460–498, 1993. doi: 10.1016/0168-9002(93)91257-N.

[92] F. Sefkow, E. Elsen, H. Krehbiel, U. Straumann, and J. Coughlan. Experience with the first level trigger of H1. *IEEE Transactions on Nuclear Science*, 42(4):900–904, aug 1995. ISSN 0018-9499. doi: 10.1109/23.467771.

[93] H.-C. Schultz-Coulon, J. Coughlan, E. Elsen, T. Nicholls, and H. Rick. A general scheme for optimization of trigger rates in an experiment with limited bandwidth. In *1998 IEEE Nuclear Science Symposium, 1998. Conference Record*, volume 2, pages 956–961 vol.2, 1998. doi: 10.1109/NSSMIC.1998.774326.

[94] T. Nicholls, M. Charlet, J. Coughlan, E. Elsen, D. Hoffmann, H. Krehbiell, H.-C. Schultz-Coulon, J. Schutt, and F. Sefkow. Concept, design and performance of the second level triggers of the H1 detector. *IEEE Transactions on Nuclear Science*, 45(3):810–816, June 1998. ISSN 0018-9499. doi: 10.1109/23.682642.

[95] Jürgen Naumann. *Entwicklung und Test der dritten H1-Triggerstufe*. PhD thesis, Universität Dortmund, 2012. URL http://www-h1.desy.de/psfiles/theses/h1th-305.pdf.

[96] I. Antcheva, M. Ballintijn, B. Bellenot, M. Biskup, R. Brun, N. Buncic, Ph. Canal, D. Casadei, O. Couet, V. Fine, L. Franco, G. Ganis, A. Gheata, D. Gonzalez Maline, M. Goto, J. Iwaszkiewicz, A. Kreshuk, D. Marcos Segura, R. Maunder, L. Moneta, A. Naumann, E. Offermann, V. Onuchin, S. Panacek, F. Rademakers, P. Russo, and M. Tadel. ROOT — A C++ framework for petabyte data storage, statistical analysis and visualization. *Computer Physics Communications*, 180(12):2499–2512, dec 2009. ISSN 0010-4655. doi: 10.1016/j.cpc.2009.08.005. URL http://www.sciencedirect.com/science/article/pii/S0010465509002550.

[97] Bjarne Stroustrup. *The C++ Programming Language*. Addison-Wesley, July 2013. ISBN 9780133522853.

[98] Niklaus Berger. *Measurement of Diffractive ϕ Meson Photoproduction at HERA with the H1 Fast Track Trigger*. PhD thesis, ETH Zürich, 2007. URL `https://www-h1.desy.de/psfiles/theses/h1th-459.pdf`.

[99] A. Baird, E. Elsen, Y. H. Fleming, M. Kolander, S. Kolya, D. Meer, D. Mercer, J. Naumann, P. R. Newman, D. Sankey, A. Schoening, H.-C. Schultz-Coulon, and Ch Wissing. A Fast High Resolution Track Trigger for the H1 Experiment. *IEEE Transactions on Nuclear Science*, 48(4): 1276–1281, aug 2001. ISSN 00189499. doi: 10.1109/23.958765. URL `http://arxiv.org/abs/hep-ex/0104010`.

[100] H. W. Kuhn. The Hungarian method for the assignment problem. *Naval Research Logistics (NRL)*, 52(1):7–21, 2005. ISSN 1520-6750. doi: 10.1002/nav.20053. URL `http://onlinelibrary.wiley.com/doi/10.1002/nav.20053/abstract`.

[101] Benno List and A. Mastroberardino. DIFFVM - A Monte Carlo generator for diffractive processes in ep scattering. In *A.T. Doyle, G. Grindhammer, G. Ingelman, H. Jung (eds): "Monte Carlo generators for HERA physics, proceedings of the workshop 1998-1999"*, volume DESY-PROC-1999-02, pages 396–404, Hamburg (DESY), 1999. URL `www.desy.de/~heramc/proceedings/wg50/list.ps.gz`.

[102] Rene Brun, Federico Carminati, Simone Giani, et al. GEANT detector description and simulation tool. *CERN program library long writeup W*, 5013, 1993.

[103] E. Fermi. Über die Theorie des Stoßes zwischen Atomen und elektrisch geladenen Teilchen. *Zeitschrift für Physik*, 29(1):315–327, December 1924. ISSN 0044-3328. doi: 10.1007/BF03184853. URL `http://link.springer.com/article/10.1007/BF03184853`.

[104] E. J. Williams. Nature of the High Energy Particles of Penetrating Radiation and Status of Ionization and Radiation Formulae. *Physical Review*, 45(10): 729–730, May 1934. doi: 10.1103/PhysRev.45.729. URL `http://link.aps.org/doi/10.1103/PhysRev.45.729`.

[105] C. F. v Weizsäcker. Ausstrahlung bei Stößen sehr schneller Elektronen. *Zeitschrift für Physik*, 88(9-10):612–625, September 1934. ISSN 0044-3328. doi: 10.1007/BF01333110. URL `http://link.springer.com/article/10.1007/BF01333110`.

[106] V. M. Budnev, I. F. Ginzburg, G. V. Meledin, and V. G. Serbo. The two-photon particle production mechanism. Physical problems. Applications. Equivalent photon approximation. *Physics Reports*, 15(4):181–282, January 1975. ISSN 0370-1573. doi: 10.1016/0370-1573(75)90009-5. URL http://www.sciencedirect.com/science/article/pii/0370157375900095.

[107] Y. Akimov, L. Golovanov, S. Mukhin, V. Tsarev, E. Malamud, R. Yamada, P. Zimmerman, R. Cool, K. Goulianos, H. Sticker, D. Gross, A. Melissinos, D. Nitz, and S. Olsen. Analysis of diffractive $pd \to Xd$ and $pp \to Xp$ interactions and test of the finite-mass sum rule. *Phys. Rev. D*, 14:3148–3152, Dec 1976. doi: 10.1103/PhysRevD.14.3148. URL http://link.aps.org/doi/10.1103/PhysRevD.14.3148.

[108] K. Goulianos. Diffractive interactions of hadrons at high energies. *Physics Reports*, 101(3):169 – 219, 1983. ISSN 0370-1573. doi: http://dx.doi.org/10.1016/0370-1573(83)90010-8. URL http://www.sciencedirect.com/science/article/pii/0370157383900108.

[109] Torbjorn Sjostrand. PYTHIA 5.7 and JETSET 7.4: Physics and manual. 1995.

[110] Marc Ross and Leo Stodolsky. Photon dissociation model for vector-meson photoproduction. *Phys. Rev.*, 149:1172–1181, Sep 1966. doi: 10.1103/PhysRev.149.1172. URL http://link.aps.org/doi/10.1103/PhysRev.149.1172.

[111] Barbara Clerbaux. *Electroproduction élastique de mésons ρ à HERA*. PhD thesis, Université Libre de Bruxelles, 1999. URL http://www-h1.desy.de/psfiles/theses/h1th-142.pdf.

[112] E. Egli, E. Elsen, V. Lemaitre, K. Müller, H. Rick, and H.-C. Schultz-Coulon. Calculating Event Weights in Case of Downscaling on Trigger Levels 1-4. H1 internal report, April 1997. H1-IN-517(04/1997).

[113] Michel David Sauter. *Measurement of Beauty Photoproduction at Threshold Using Di-Electron Events With the H1 Detector at HERA*. PhD thesis, Swiss Federal Institute of Technology Zurich, 2009. URL https://bib-pubdb1.desy.de/record/91126/files/h1th-518.pdf.

[114] Andreas W. Jung. *Measurement of the $D^{*\pm}$ Meson Cross Section and Extraction of the Charm Contribution, $F_2^c(x;Q^2)$, to the Proton Structure in Deep Inelastic ep Scattering with the H1 Detector at HERA*. PhD thesis, Ruprecht-Karls-Universität Heidelberg, 2009. URL https://www-h1.desy.de/psfiles/theses/h1th-504.pdf.

[115] H1OO analysis framework. Internal documentation, 2015. URL https://www-h1.desy.de/icas/oop/.

[116] Florian Huber. *Elastic and Proton Dissociative J/ψ Photoproduction at low $W_{\gamma p}$ with the H1 Detector at HERA*. PhD thesis, Ruperto-Carola Universität Heidelberg, 2012. URL http://www-h1.desy.de/psfiles/theses/h1th-796.pdf.

[117] Karin Daum. H1 Tracking Group. Personal communication, karin.daum@desy.de, January 2015.

[118] ROOT Reference Guide. TGraphAsymmErrors, 2015. URL https://root.cern.ch/root/html/TGraphAsymmErrors.html#TGraphAsymmErrors:Divide.

Danksagung

Diese Arbeit ist meinem Bruder Carl Friedrich gewidmet, dessen Hilfsbereitschaft stets nur eine Textnachricht entfernt wartet. Danke, für all die Unterstützung, die du mir über die letzten sechs Jahre gegeben hast.

Ich bedanke mich herzlich bei Prof. Dr. André Schöning dafür, dass er mir diese Arbeit ermöglicht hat und für seine Betreuung während des letzten Jahres. Ich bedanke mich bei Prof. Dr. Ulrich Uwer dafür, dass er die Zweitkorrektur der Arbeit übernommen hat.

Vor allem danke ich auch Michel Sauter für seine sehr gute Betreuung im letzten Jahr und für alles, was er mir in dieser Zeit beigebracht hat.

Schließlich bedanke ich mich bei Eltern und Großeltern, die durch ihre großzügige Unterstützung mein Studium möglich gemacht haben.

Erklärung:

Ich versichere, dass ich diese Arbeit selbstständig verfasst habe und keine anderen als die angegebenen Quellen und Hilfsmittel benutzt habe.

Heidelberg, den (Datum) .....